To the Graduate Council:

I am submitting herewith a dissertation written by Reza Safabakhsh entitled "Automated Visual Inspection for Detection, Characterization, and Measurement of Flaws on Machined Metal Surfaces." I have examined the final copy of this dissertation for form and content and recommend that it be accepted in partial fulfillment of the requirements for the degree of Doctor of Philosophy, with a major in Electrical Engineering.

R. C. Gonzalez, Major Professor

We have read this dissertation
and recommend its acceptance:

Accepted for the Council:

Vice Provost
and Dean of The Graduate School

AUTOMATED VISUAL INSPECTION FOR DETECTION, CHARACTERIZATION, AND MEASUREMENT OF FLAWS ON MACHINED METAL SURFACES

A Dissertation

Presented for the

Doctor of Philosophy

Degree

The University of Tennessee, Knoxville

Reza Safabakhsh

March 1986

Oh kings,

we destroyed all the outside enemies,

but yet,

there remains the worst enemy

inside!

Mowlawi

ACKNOWLEDGEMENTS

The author wishes to express his appreciations to Professor R. C. Gonzalez for his guidance of this research and his support and friendship. The author's appreciations are also extended to Professors R. W. Rochelle, R. E. Bodenheimer, D. W. Bouldin, and C. F. Moore for serving on the dissertation committee. Much gratitude is offered to Professor M. A. Breazeale of the Physics Department for the many useful discussions he held with the author during the course of this research.

The author would like to thank Martin Marietta Energy Systems, Inc., for financing and supporting this investigation. His gratitude is also extended to the Electrical Engineering Department for providing the author with financial support throughout his graduate program.

Special thanks are due to Ms. Denise Smiddy for her excellent work in typing this manuscript, Mrs. Jenny Craven for doing the drawings, and Mr. David Donahue for correcting the language of the manuscript.

ABSTRACT

This work investigates the automatic inspection of machined metal surfaces through their light scattering properties. Light patterns resulting from the incidence of laser light on a surface flaw are studied to develop efficient methods for detection, characterization, and measurement of flaws on machined surfaces. The work places special emphasis on flaw depth inspection and the simplicity of the inspection system.

Experimental investigations of this study involve optical and pattern recognition techniques. Low-power laser light impinges on a machined surface normally. The scattered light is focused on a Wedge/Ring detector whose signals are processed by pattern recognition algorithms to qualify the surface.

Three theoretical light-scattering models are developed for surface flaws. These models indicate that the light scattered from a flaw surface is dependent on flaw parameters, experimental factors, and surface properties, and that the observed light intensity and flaw depth do not have a one-to-one relationship.

The major experimental results are that flaw detection based on a given depth threshold can be performed very satisfactorily if flaw width and shape do not disturb the depth inspection drastically. However, separating flaws into different classes based on depth cannot be performed so successfully. Improvement of the results generally requires finding a data feature which depends only on flaw depth or developing models which properly accommodate the effects of flaw depth, width, and shape.

Experimental models are developed for construction of flaw shape and measurement of flaw dimensions. While shape construction is hindered by laser characteristics, measurement of flaw depth or width can be performed fairly satisfactorily, although it needs further improvement.

This study examines some theoretical and some experimental aspects of metal surface inspection. Although the results do not present a complete solution to the problem, they constitute a significant contribution to the state of the art in this field.

TABLE OF CONTENTS

CHAPTER		PAGE
1.	INTRODUCTION	1
2.	AUTOMATED VISUAL INSPECTION BACKGROUND	7
	2.1 Inspection, The Necessary Evil	8
	2.2 Automatic Inspection	10
	2.3 Automatic Visual Inspection Systems	14
	2.3.1 Light Sources	16
	2.3.2 Optical Components	18
	2.3.3 Detectors	20
	2.3.4 Processors	26
	2.4 Automatic Metal Surface Inspection	31
	2.4.1 Surface Finish Monitoring	32
	2.4.2 Defect Detection	33
	2.4.3 Defect Measurement	37
	2.5 Concluding Remarks	38
3.	LIGHT SCATTERING MODELS FOR FLAWS ON METAL SURFACES	40
	3.1 Surface Profile Approximations	41
	3.2 Light Scattering Theories and Models	46
	3.2.1 The Point-Source Approximation	47
	3.2.2 The Tangent-Plane Approximation	51
	3.2.3 The Perturbation Theory Approximation	58
	3.3 Comparison of the Models	65
4.	THE EXPERIMENTAL INSPECTION SYSTEM	67

4.1 Experimentation Approach and System Components . 68
4.1.1 The Laser Light Source 70
4.1.2 The Translation Stage 70
4.1.3 The Optical Configuration 70
4.1.4 The WRD-6400 Detector 71
4.1.5 The High Speed Sampler 74
4.1.6 The Microcomputer System 74
4.2 The HSDPS Output 75
4.3 The Sensor Characteristics and Calibration 76
4.3.1 The Dark-Current Test 76
4.3.2 The Uniform Lighting Test 78
4.3.3 Calibrating The Detector 79
5. INSPECTION OF MACHINED METAL SURFACES BY THE EXPERIMENTAL SYSTEM 88
5.1 Sample Parts for Experiments 89
5.2 Feature Extraction and Correlations. 94
5.2.1 Environmental Lighting Effects 94
5.2.2 Feature Selection 95
5.3 Flaw Detection 104
5.4 Flaw Characterization 113
5.4.1 Classification of Flaws 113
5.4.2 Flaw Shape Construction 120
5.5 Flaw Measurement 132
5.5.1 Experimental Models 132

5.5.2 Flaw Measurement by the Linear Model 134

5.5.3 Width Measurement and the Varying-V Models. 141

6. CONCLUSIONS AND RECOMMENDATIONS 146

BIBLIOGRAPHY 157

APPENDICES 165

APPENDIX A. SCATTERED FIELD FOR A POINT LIGHT SOURCE 166

APPENDIX B. SCATTERING COEFFICIENT FOR PLANE WAVES. 172

APPENDIX C. SURFACE PROFILE TRANSFORAMTION 178

APPENDIX D. TRUNCATED DATA STATISTICS . . . 183

VITA 197

LIST OF TABLES

TABLE		PAGE
4.1	Calibration coefficients for the 64 elements of the WRD-6400 detector	83
5.1	Flaws used in correlation experiment	97
5.2	Cluster separation coefficients for the selected features	104
5.3	Depth and width correlations for the selected features	104
5.4	Correct detection of flaws used in training by the minimum distance classifier	108
5.5	Correct detection of flaws used in training by the Bayes classifier	109
5.6	Correct detection of test flaws by the minimum distance classifier	110
5.7	Correct detection of test flaws by the Bayes classifier	111
5.8	Correct classification of training and testing patterns into four ranges of flaw depth	115
5.9	Correct classification of a set of flaws chosen to show the degrading effect of flaw width	117
5.10	Evaluation of models used for flaw depth measurement	138
5.11	Error percentages of flaw depth measurements	139
5.12	Measurement of flaw depth and width by two models	143
D.1	Mean values of features 1-10 for truncated data	184
D.2	Mean values of features 11-20 for truncated data	185
D.3	Mean values of features 21-30 for truncated data	186
D.4	Standard deviations of features 1-10 for truncated data	187
D.5	Standard deviations of features 11-20 for truncated data	188

D.6 Standard deviations of features 21-30 for truncated data . 189

D.7 Lower limits of features 1-10 for truncated data 190

D.8 Lower limits of features 11-20 for truncated data 191

D.9 Lower limits of features 21-30 for truncated data 192

D.10 Upper limits of features 1-10 for truncated data 193

D.11 Upper limits of features 11-20 for truncated data 194

D.12 Upper limits of features 21-30 for truncated data 195

D.13 Correlation between truncated data features and flaw depth or width 196

LIST OF FIGURES

FIGURE		PAGE
2.1	General structure of an AVI system	15
2.2	A laser scanning system	21
2.3	Possible functions of the AVI system processor	27
3.1	Sinusoidal approximations for defective surface profiles	43
3.2	Piecewise linear approximation of a defective surface profile	45
3.3	Light scattering from the piecewise linear model	49
3.4	General light scattering geometry	53
4.1	Components of the experimental inspection system	69
4.2	Three optical configurations for data acquisition	72
4.3	Surface of the WRD-6400 detector	73
4.4	Sample raw and calibrated data for a high light intensity	84
4.5	Sample raw and calibrated data for a medium-high light intensity	85
4.6	Sample raw and calibrated data for a medium-low light intensity	86
4.7	Sample raw and calibrated data for a low light intensity	87
5.1	Photographs of several parts used in experiments	91
5.2	Typical profile of machined surfaces used in experiments	92
5.3	Three sample flaw profiles	93
5.4	Mean values of flaw groups for various features	100
5.5	The Coincident Spectral Plot for the three features RS, RP1, and T*P.	118
5.6	The decision tree for the four-class tree classifier	119

5.7 Representing scratch shape by contours 124

5.8 Representing scratch shape by a varying V 124

5.9 Determination of Belt and Grid Models 125

5.10 Construction of flaw shape by contours for scratch C2 . . . 126

5.11 Construction of flaw shape by contours for scratch C9 . . . 127

5.12 Mean profiles for scratches C1, C2, C4, and C9 129

5.13 Contracted mean profiles for scratches C1, C2, C4, and C9 . 130

5.14 Inverting a Belt Model profile in several ways for obtaining flaw shape 131

5.15 Different feature regions for Model 3 136

5.16 Comparison of the Light-section Microscope calibration and a Varying-V model for scratch C2 144

CHAPTER 1

INTRODUCTION

Vision is one of the most important senses of man, providing him an effective and efficient faculty to determine what goes on in the *world* around him. This *optical non-contact* sensory facility enables man to do a wide variety of things which would have been difficult or impossible to do without visual capability. A similar condition is true in many industrial machines. Introduction of visual sensors in such machines will increase their intelligence and efficiency, boost their capabilities, and enable them to do things which they could not do otherwise.

Computer vision techniques have been applied successfully to aerial photographs and medical images for some time; but they were not directed towards use in industrial machines until recent years. The available sensing devices, vision algorithms, and computing power were not suitable for industrial applications where the demand for speed is high, the available computing power and storage capacity are low, and the investment capital is rather limited. However, in recent years there have been considerable improvements in vision system components. These improvements have provided means of developing efficient, economical seeing machines for industry, although major difficulties still must be overcome before these machines reach maturity in visual sensing. Even when the application is limited only to visual inspection, a thorough understanding of the problems is lacking, and development of economical,

efficient, and automatic inspection systems in most cases is yet to be achieved. The difficulties are felt more seriously when complexities associated with many applications make the technical feasibility of automation questionable. Here, technical complexities combine with economic and efficiency considerations to render the development of automated inspection systems less successful.

One of the technically-questionable cases arises in the inspection of metal surfaces, where complexities result due to the nature of the surfaces and their inspection needs. Characteristics of metal surfaces and their flaws vary from one point on the surface to another. This changes the light scattering properties of the surface and the flaw and complicates the inspection task. In addition, the inspection requirements of most applications frequently go beyond simple flaw detection. Often, it is desirable to know the degree of deviation of a faulty part from the acceptable standards, to provide some type of overall description for the flaw, or to give precise measurements for certain flaw dimensions. Characterization and measurement of flaws put the technical feasibility of automated metal surface inspection under question. Nevertheless, the significance of surface qualification in industry and the high expense and inefficiencies of manual methods have made the automation of metal surface inspection highly desirable and have constituted the drive for development of automated methods, despite discouraging difficulties.

Theoretical analysis of the problem necessitates the study of wave scattering from random surfaces. In general, the wave equation should be

solved for the scattered field subject to the boundary conditions given by the scattering surface. However, this cannot be done in a perfect manner. The metal surface and the flaw profile should be approximated by a simplified profile, and approximations must be adopted to allow calculation of the scattered field. Then a light scattering model can be developed for the flaw to show the relationship between the observed light intensity and flaw parameters such as width and depth. Such models are indispensable in understanding the nature of light scattering from metal surfaces and may be useful in obtaining flaw parameters for a given light intensity.

A linearly-polarized monochromatic light source, such as a laser, seems to be more appropriate for depth inspection than other light sources. Incidence of laser light on a flaw produces diffracted light patterns which can be studied to determine the characteristics of the flaw. The most crucial step in such a study is to find one or more features of the light pattern which correlate with flaw characteristics. It is highly desired that each such feature relate to one flaw parameter only, and be insensitive to other parameters. Finding such features will guarantee the success of the inspection system. However, in reality, it is more likely that the features will be influenced by more than one parameter. For example, a feature which represents flaw depth may very well be affected also by flaw width or shape. The experimental analysis accordingly should accommodate such influences to arrive at the desired accuracies. If this is achievable, however, it may also have the adverse effect of introducing additional errors in the depth measurement.

Inspection of flaws may be based on single data acquisitions or a number of data acquisitions from the flaw. Using single data acquisitions is desirable because it results in a faster inspection process. However, such an approach has a serious drawback. How is the system supposed to locate the deepest point or the widest point of the flaw for depth or width inspection? Finding these points fairly accurately requires many more data acquisitions which will slow down the inspection, but which will also produce an advantage. The data sets can be used to represent the profile in some form. For example, a mean profile for a portion of the flaw or the whole flaw can be attractive for applications which do not require very high accuracy. Another form of flaw representation, if attainable, is a three-dimensional construction of flaw shape. This will portray much information about the flaw and will provide a complete description of the flaw.

Based on the above considerations, this work examines the inspection of machined metal surfaces. The investigation is presented with the following organization. Chapter 2 contains a comprehensive review of the background material. Problems associated with manual inspection are presented, and the need for automation of inspection is justified. Then, a general structure for automated inspection systems is given and each of its components is described briefly. The chapter concludes with a summary of the literature on automated metal surface inspection, including surface finish monitoring, defect detection, and defect measurement.

The theoretical study of the problem is included in Chapter 3. Mathematical representations for surface flaws are given, and three approximate light scattering theories are applied to them. The results are three models describing the light scattering behavior of the flaws. The models suggest the dependence of the light scattered from flaw surface on the flaw dimensions, surface characteristics, and system configuration. A uniqueness problem is also indicated to exist between flaw depth and the observed light intensity.

Chapter 4 describes the specific approach chosen for experimental investigation and introduces the various components of the selected inspection system. Characteristics of a special detector, called the WRD-6400 detector, are studied. Several preprocessing operations are suggested to correct the highly unbalanced responses of the detector elements. A set of calibration coefficients are found to compensate for the undesirable detector characteristics and are used subsequently to correct all the data.

The experimental results of inspection are summarized in Chapter 5. A statistical study of the relationship of flaw depth and 30 features extracted from data gives four features as the most appropriate features for flaw depth inspection. These features are sum of ring data, total energy multiplied by peak of ring data, peak of ring data, and the ratio of sum of ring data 5 to 32 to sum of ring data 16 to 32. The chapter examines inspection of flaws in three forms -- detection, characterization, and measurement. Detection of flaws separates flaws into the two GO and NO-GO classes based on a depth threshold. Flaw characterization is fulfilled in

two ways -- determining the range of flaw depth and constructing the shape of the flaw. Based on the models obtained in Chapter 3, several experimental models are developed and utilized in the measurement of flaw width and depth. Experimental results for the different forms of inspection are presented, and the error-causing factors in each case are discussed.

Finally, Chapter 6 presents the conclusions obtained from the study and makes recommendations for the continuation of the work.

CHAPTER 2

AUTOMATED VISUAL INSPECTION BACKGROUND

Automation of inspection is intended to reduce problems associated with manual inspection and to overcome weaknesses related to human inspectors. Most industries strive to meet expectations of their customers concerning quality and performance of their products. Inspection of industrial parts and products, therefore, is a necessity which cannot be avoided, even though it constitutes a significant overhead.

Customer expectations in many cases are dictated by technical requirements which are rather strigent. An example of such cases is surface qualification of production parts, which is very crucial in applications dealing with quick motion and great strain. This stringency means that industrial inspection is not always an easy job. Indeed, it can be quite involved and take a long time, requiring a high level of skill and, accordingly, increasing production expenses. Naturally, this situation will be intensified if 100% inspection is required for difficult or slow inspection tasks.

Automatic inspection aims at reduction or complete elimination of difficulties connected with manual inspection. It attempts to shorten the inspection time, to increase the inspection efficiency, to implement difficult tasks through innovative approaches and intelligent machines, and to reduce inspection overhead, resulting in substantial long-term savings.

Background material concerning automated inspection is presented in this chapter. Some issues surrounding inspection and its automation are discussed and the need for automated inspection is justified. Furthermore, the general structure of Automatic Visual Inspection (AVI) systems and a brief description of their components are introduced. The chapter continues with a survey of automated visual metal-surface inspection and ends with a summary of conclusions.

2.1 Inspection, The Necessary Evil

Inspection is the process of verifying whether or not a part or product is what it is supposed to be and can do what it is expected to do. The part or product may be checked from the standpoint of compatibility, interchangeability, reliability, or acceptability. This means that the part or product may be inspected for its capability to combine with other parts without undesirable after effects, its capability of being interchanged, the extent to which it produces consistent results, or its conformity with approved standards. However, not all these aspects are crucial in every inspection task. Inspection criteria incorporate the essential checks which guarantee the quality to in-house and customer satisfaction. In this regard, inspection consists of a series of comparisons between the product and some criteria.

Some of the inspection tasks are relatively simple and can be performed without the need for sophisticated equipment or skilled inspectors. In other cases, however, complicated equipment as well as

skilled personnel are required for inspecting parts or products by comparing them to masters, photographs, or drawings of acceptable samples. The personnel, equipment, and facilities required for such inspection operations constitute a significant overhead which many industrial managers consider undesirable on one hand and necessary for survival on the other hand. Thus, inspection is a necessary evil and its efficient handling and containment is a long-standing objective of management.

In addition to economic problems, certain weaknesses associated with manual inspection make its adoption in many applications undesirable or impractical. The first weakness is that inspection decisions made by human inspectors are dependent on their physical and psychological conditions. Fatigue, boredom, discomfort, anxiety, hatred, love, and similar factors strongly affect the decision-making of the inspectors. Fadl and Parsons [1978] give result of an experiment in which parts inspected by an inspector in the morning were returned to him in the afternoon for reinspection. The results differed 20% to 25% from morning to afternoon. The second weakness is that performing on-line inspection by human inspectors is not possible in some applications. Continuous work under constant concentration produces strain and creates problems with human perception and information processing. Inspection of moving parts, in particular, exerts an enormous pressure on the inspector's reception that no human being can tolerate for a sustained period of time. An example of this situation arises in on-line inspection of moving metal surfaces. It is not

possible for human inspectors to inspect the surface even at moderate mill speeds. The third weakness of manual inspection in some applications is its slowness. This shortcoming not only slows down the production output, but also adds to the handling costs.

Manual inspection can offer viable solutions to simpler inspection tasks; nevertheless, it comes short of efficiently solving the more complicated ones, and in some cases it simply is not practical. Improved performance, higher speeds and more economical inspection approaches are demanded in many fields. What alternative is likely to offer the desired solution?

2.2 Automatic Inspection

Using machines to perform inspection or to aid the inspector will solve the inspection problems in many fields. Although automation of most inspection processes will demand considerable initial investment, in the long run automatic inspection will reduce expenditures and justify itself economically. As human influence in decision-making is reduced, automatic inspection will bring about more consistency and thus improved results. Errors made in manual inspection due to fatigue and exhaustion will be eliminated with the untiring machines. In addition, the more difficult or even some impossible manual inspection tasks will be feasible by automatic methods. Speed of inspection will increase significantly and technical and economic improvements will result.

The benefits of automatic inspection include:

1. Reducing inspection manpower, especially skilled personnel, and inspection time, thus achieving higher throughput and lower labor costs;
2. Improving accuracy, consistency, and objectivity of inspection;
3. Increasing reliability and thus decreasing warranty costs;
4. Improving control of incoming goods and supplies;
5. Matching speed of inspection with the speed of production, resulting in savings in material handling;
6. Allowing greater flexibility in coping with demand changes;
7. Providing the possibility of 100% inspection;
8. Allowing better feedback to engineering/design areas through collection of accurate and complete statistical data;
9. Providing greater operator comfort and safety and higher equipment protection;
10. Lowering the possibility of damage to products during inspection;
11. Allowing integration of inspection with production and hence improving machine, manpower, and material utilization through quick reaction to detected faults;
12. Improving corporate image by installing new technology--a marketing weapon;
13. Providing more efficient service to the customers and thus encouraging higher sales; and
14. Defeating competitors who cannot afford the investment necessary for automation and making new entries to the market less likely.

Not all applications lend themselves to automation with equal ease. In general, applications chosen for automation should be within growing industries with a higher level of competition. They should possess one or more of the following attributes:

1. There is a high throughput and thus demand for mass-inspection.
2. The inspection time is long, and large numbers of inspectors are needed.
3. 100% inspection is demanded but cannot be carried out manually.
4. High penalties result if the product does not meet standards.
5. The product does not have a complicated external appearance (it does not include many knobs and switches) and has recognizable edges.

These conditions indicate which applications are more likely to be potential candidates for automation at present.

Automatic inspection systems have developed slowly for several reasons. On the technical side, although powerful computers with mass-storage devices have been available at reasonable costs for some time, good sensing capability as well as fast and efficient processing algorithms necessary for the more sophisticated applications have not been available. As a result, consideration of many applications for automation has been out of the question due to costs, inefficiencies, or difficulties.

From the economic point of view, one major obstacle in the way of development of automatic inspection systems has been the need for a different solution for each separate application. Each application, therefore, will have its own development expenses. This is an investment which should be assessed on whether or not it is likely to provide a return

on capital. In fact, deciding whether or not to automate is not a simple task. A large number of interacting economic factors and constraints must be analyzed and evaluated, and the present and future trends of the market must be studied before economic feasibility can be established. These difficulties, along with the natural conservatism existing in industry, are the factors responsible for today's lack of many automated inspection systems in industry.

Automated inspection systems, nevertheless, will increasingly appear in industry in the near future. Recent advances in the fields of optics and visual sensing technology are improving and will continue to improve the acquisition of inspection information. Moreover, the digital algorithms of pattern recognition and image processing, which have been applied to other fields such as medicine and defense, are being adapted to suit industrial inspection applicaitons. The real difference here is that in industrial applications, computer vision systems must have reasonable cost and fast response in addition to high performance; the major criterion in military or medical image processing is merely high performance. As economic pressures become sufficiently strong, technical difficulties for the most parts are resolved, and competitors automate, many industries will utilize a generation of automatic inspection machines which are economical, efficient, easy to use, easily programmable, easily applicable to a wide variety of applications, suitable for operation in plant environment, and reliable with quick and low-cost breakdown repair.

2.3 Automatic Visual Inspection Systems

AVI should not be perceived as a narrow field. Applications presently represented under this discipline make the interpretartion of the field and the terms *automatic*, *visual*, and *inspection* rather broad. *Automatic* should be interpretted as *semi-automated* or *fully automated*. *Semi-automated* would mean that the machine works in conjunction with an operator to perform parts of the task. In contrast, *fullly-automated* refers to the situation in which the machine performs all the tasks without the need for operator intervention. All the methods of data acquisition in which data can be represented in the form of an image are considered *visual*. In this context, systems using ultrasound, x-ray, infrared, microwave, and similar approaches to data acquisition are considered visual systems. Term *inspection* should not be regarded as referring to only defect detection. The present trends in automation also consider measurement, counting, sorting, grading, and verifying as parts of the inpsection task. These definitions indicate that AVI should be considered as a broad discipline.

The general structure and components of an AVI system are shown in Figure 2.1. The system may include a light source for illuminating the object under inspection, neessary optical components for directing or structuring the incident light, neessary optics for directing or collecting the light scattered from the object surface, a detector to register the scattered light, and a processor to process the detector signal. For optimal performance of the system, each part of the AVI machine must be optimized individually. A brief discussion on AVI system components is in order.

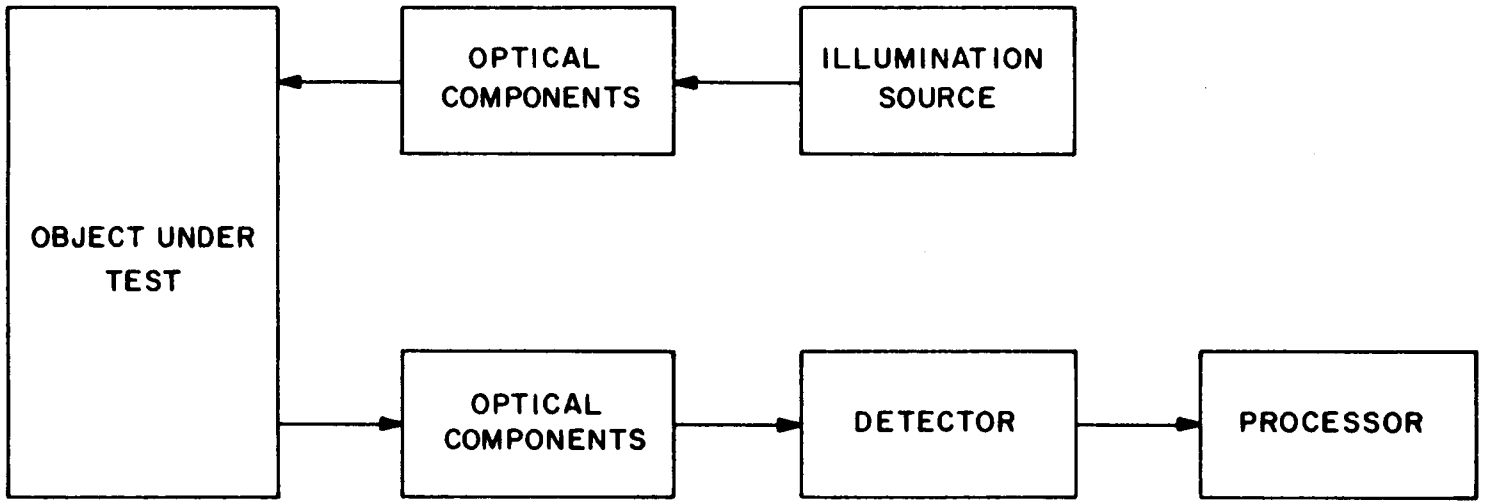

Figure 2.1. General structure of an AVI system.

2.3.1 Light Sources

Two groups of light sources are in use today in inspection systems. The first group consists of different types of lamps such as tungsten filament, quartz halogen, fluorescent, and arc discharge high-pressure mercury lamps. The second group consists of low-power lasers. Each of these light sources has its own pecularities and characteristics which make it suitable for certain applications. Nevertheless, the first group of lamps is more commonly used in conjunction with imaging and image procesing techniques while the second group is generally used in conujunction with diffracted light patterns and analog or digial processing.

Characteristics of lamps are different. The spectral distributions of the tungsten filament, quartz halogen, and fluorescent lamps are continuous with smooth changes, while the high-pressure mercury lamp has a discontinuous spectral density consisting of a series of spikes. Examination of the typical spectral densities show that the first three lamps radiate not only visible light, but also considerable infrared and little ultraviolet wavelengths. This radiation shifts more toward infrared in tungstan filament and quartz halogen lamps if the lamps are under-run or if their intensities are reduced by light-dimmers. The tungsten filament lamp is a non-uniform point source in which the flux shape is dependent on the filament shape. The quartz halogen lamp is also non-uniform, but it can be either a point or a linear source. The fluorescent lamp, on the other hand, is a linear source with even distribution, lower intensity, and higher efficiency. Finally, distribution of light within the radiation pattern in

tungsten filament and quartz halogen lamps is amorphous, resulting in superimposing of shadows on the actual images. In contrast, the fluorescent lamp does not add shadows for most of its length as it has uniform distribution along its length except for the neighborhood of its two ends.

Lasers used in inspection tasks are generally low-power He-Ne gas lasers, radiating 1 to 5 mw of power at the wavelength of 0.6328 μm. The main reason for using this type of lasers as opposed to many other types available is their longer tube life and much lower price. The most outstanding properties of the laser beam are its high degree of directionality, monochromaticity, coherence, and brightness. The laser provides very bright and directional light with well-defined phase and wavelength which can interfere. These properties make lasers unique for use in certain applications where conventional lamps cannot be focused sharply enough and do not guarantee constant light intensity. Also, the insufficient power of conventional lamp light sources necessitates proximity to the object under inspection while the laser head can be kept far away from the object.

If smaller beam divergence and minimal spot size is desired in an application, one must use lasers which to a great extent eliminate all modes other than the lowest mode, TEM_{00}. The TEM_{00} mode corresponds to the lowest order solution of the laser cavity resonator and is depicted in a circular luminous spot with Gaussian radial intensity distribution.

2.3.2 Optical Components

Even though illumination of the object under test may not seem so important, it plays a major role in the success of inspection systems. Good illumination will bring out those features of the image or the scattered light pattern which are helpful in solving the problem and will eliminate those features which will make the task merely more complicated. The result is that the necessary processing will be simplified and the costs will decrease significantly. Optical components perform this task by directing and structuring light and implementing innovative lighting methods. Natural light varies so much that not only can it not be used for illumination, but it must also be controlled to not to disturb the artificial lighting.

A large number of components are used for manipulating light. This section will briefly cover some of the elements which are more useful in inspection systems.

Diffusers may be *transmitting* or *reflecting*. They are used to spread light from a source onto an area evenly. Diffusers are made from plastic or ground glass.

Condensers are certain types of lenses or mirrors which are used to reroute light from a source or an object while eliminating shadows.

Reflectors and mirrors redirect light from a source at a predetermined angle. Dichroic reflectors with an infrared filtering property as well as hot and cold mirrors act to not only redirect light, but also remove unwanted wavelengths.

Filters are used to allow passage of certain wavelengths to the object while preventing passage of other wavelengths. Filters reduce spurious reflections and generally improve image defintion.

Beam splitters are part mirrors and part window. They are employed in many laser-based systems for dividing light into two paths. Beam splitters furnish the means of simultaneous normal incidene and normal observation.

Rotating disks and shutters can be used for chopping off the beam and breaking it into bursts or for strobing.

Light guides can perform branching and realigning of light. Light may be divided from a single source into several branches or it may be routed from a source to an object with the facility to negotiate obstacles and to align at the user's discretion.

Lenses of various types provide a variety of operations for manipulation of light. Common examples of such operations are expanding light beam diameter, collimating the light beam, adjusting the beam size to smaller size (e.g., size of sensor surface), and focusing light at a certain point. The performance of lenses has a strong influence in the success or failure of an inspection.

Physical lenses depart from ideal conditions. These departures are referred to as lens aberrations and exist for both monochromatic and chromatic light. Lens aberrations change the intensity profile in the image by blurring sharp edges and points, and they introduce shifts from the true positions, thus distorting images. Increasing lens aperture or field angle

worsens almost all types of aberrations. Lens aberrations are usually corrected for the circumstances for which the lenses are designed. Enlarging lenses, for example, are designed to work best at their moderate magnifications. As a result, a lens should be chosen so that the required magnification is the moderate magnification of the lens, the field angle is just large enough to produce the desired image size, the aperture is stopped down, and the lens resolution permits formation of the image with the necesary resolution.

Laser scanners are opto-mechanical devices which put the laser spot into motion on the surface under test. A sketch of a laser scanner is shown in Figure 2.2. The rotating mirror makes the laser beam scan the surface in a line. A second motion obtained from the surface itself (in on-line inspection) in a direction perpendicular to the scan line will make the coverge of the whole surface possible. Converging lens elements are used to produce a collimate beam while keeping aberrations minimal. More complicated laser scanners which are used for inspecting specular surfaces include other components such as diffusion strips or cylindrical lenses as well.

2.3.3 Detectors

In addition to appropriate illumination of the object under test, registration of a good image or scattered light pattern requires a sensor which can function under hostile conditions with minimum error-causing and quality-lowering effects while remaining economical. Production environments, are generally hot, humid, dusty, or oily. Photosensitive

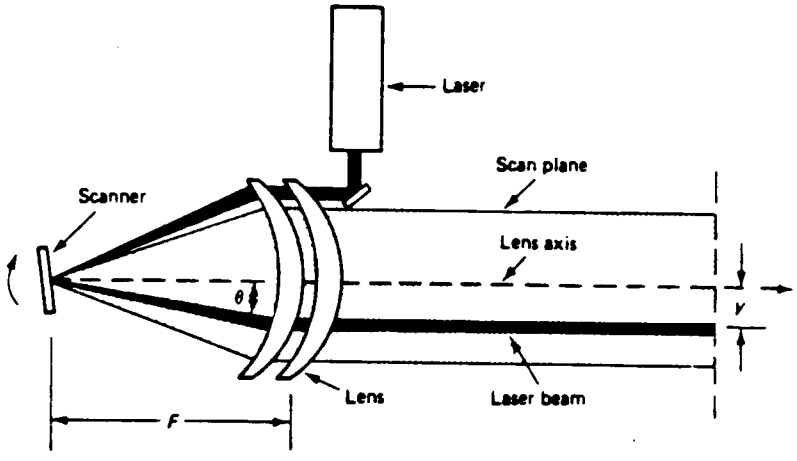

Figure 2.2. A laser scanning system (from Luxon and Parker [1985]).

devices usually do not function very well in such conditions. These factors along with the lack of variety in sensors have made effective sensing a major problematic part of the AVI system. Nevertheless, significant improvements in the sensor technology have been made in recent years, and this trend will continue at a fast pace. This section will introduce the most common visual sensors and some of their characteristics.

Television cameras have been improved significantly since the invention of these imaging devices over sixty years ago. The advent of vidicon tubes particularly has lead to production of a family of cameras which perform more efficiently and which are considered standard television cameras. Today, these cameras offer certain characteristics which make them preferred options for specific types of applications. They can offer extended spectral response, very high sensitivity, wide dynamic range, high-speed strobing, very high resolution, electronic zooming, high tonal quality, and a wide range of ancillary equipment avaialbe at modest cost.

These advantages, where they apply, must be balanced against some well-known disadvantages of these cameras. Television cameras are not made for continuous work at hostile environments. Their lives, as a result, are short in industrial applications. They are succeptible to damage, have large size, require high voltages, have imprecise scanning, and are heavy. In addition, their dark current may make the image background lighter, their image-retention tendency will register a semi-permanent record of image highlights, and their inherent lag reduces the response speed. On

the top of all these, the analog signal of a television camera needs to be converted to digital form by a usually-expensive digitizer before it can be processed.

The advantages and disadvantages of the television camera must be carefully considered and compared to those of the other detectors before deciding what sensor should be used for an application.

Solid-state arrays are the present rivals of television cameras in industrial applications, and it is very likely that they will surpass the performance of television cameras in the near future. These devices started out several decades ago actually as bundles of discrete photodiodes and have evolved with the advancement of the integrated-circuit technology to the stage of incorporating up to 2048 sensitive elements in one-dimensional arrays and 488 x 380 elements in two-dimensional arrays on a single silicon chip. Furthermore, the necessary scanning circuits are also included on the same chip, providing the means of in-turn interrogation of the elements.

Solid-state arrays are *integrating* detectors as are television cameras. As a result, the sensitivity of solid-state arrays is proportional to the exposure time; and the higher the light level, the faster the arrays can be scanned. However, if the light level and exposure time go up, they could result in element saturation of the array. Another characteristic of solid-state arrays is their dark leakage current which, as in any other silicon chip, increases with temperature. This dark signal is unfortunately different for each one of the array elements, making it harder to

compensate for the leakage current and imposing limitations on the uncompensated array.

There are two types of non-uniformities among the elements of a solid-state array -- *dark-signal* non-uniformities and *response* non-uniformities. The dark-signal non-uniformity, as mentioned above, is temperature dependent and varies from chip to chip significantly. A cooling unit can reduce this type of non-uniformity. Response non-uniformity arises because of different gains of different array elements and is highly dependent on the light color. It is higher for red and infrared wavelengths. A calibration procedure with the same color is necessary to correct this effect.

Other characteristics of the solid-state arrays are the random noise associated with the readout of the element signals, cross talk between different elements (which increases as the light wavelength increases), and spectral response (which is biased towards red and infrared and is more limited than that of the television camera).

Despite some drawbacks associated with the solid-state arrays, they offer certain advantages which makes them more appropriate for many applications. These arrays are more rugged, perform better in hostile environments, are lighter and smaller, have longer lives, and have rapid and variable scan rates.

A special type of diode-array sensor has also been made with a different philospopy. This sensor, called the Wedge/Ring Detector has been constructed so that it can measure the amplitude and distribution of a light

pattern focused on it. Further description of this sensor will be given in Chapter 4.

Photomultipliers are designed to work as detectors for laser scanners. They have a light-sensitive cathode and an internal electron-amplifying mechanism. The analog signal produced by these devices is a description of the surface reflectivity. The presence of a defect on the surface changes this reflectivity and thus the photomultiplier signal. This signal may be processed by a threshold detector to generate a trigger.

Photomultipliers have high gain-bandwidth products and provide simple means of detection and processing for laser scanners. However, they are fragile, have short lives, need high voltages for operation, may be damaged by high light levels, and have very blue-biased spectial responses (resulting in poor response at the red and infrared wavelengths).

Fiber-optic sensors consist of a light source, optical fibers, and a photoreceiver. For inspection purposes, these devices can be low-power or high-power. The light source in a low-power fiber optic sensor is a small lens-ended lamp or a light-emitting diode. Larger lamps are used when higher energy is required. Optical fiber probes are made of transparent dielectric fibers which conduct light efficiently. Total internal reflections of light on the walls of these fibers gives them good light gathering capacity. However, since attenuation in the fiber is high, the length of the fiber should ideally not exceed 0.75 meter for low-power optical fiber sensors and 2 meters for high-power sensors. The receivers of these sensors are usually

photodarlingtons, phototransistors, or photodiodes whose sensitive areas are interfaced to the end seciton of the optical fiber probe.

Fiber-optic sensors are non-imaging, non-contact devices which can be used effectively in inspection tasks. Their speed of response and reasonable cost make them suitable for economical, high-speed inspection. They can be interfaced easily to computers to boost the processing power. Similar to other optical devices, these devices must be kept clean.

2.3.4 Processors

Processing is another key element in AVI systems. Despite the influence of other components, the performance of the overall system eventually depends on the processor. An inefficient processor will degrade system performance even though other parts of the system function optimally. The proessor must be able to extract information necessary for inspection and to make a decision at a sufficiently high speed and for a reasonable cost. Requiring both great processing power at high speed and low costs is contradictory. As a result procesing units frequently perform certain manipulations on data before the main processing. These operations, whereever possible, are performed by hardware implementation.

Processor functions, as illustrated in Figure 2.3, consist of preprocessing, main processing, storage, and display. The first preprocessing operation, where it applies, is probably correction for camera imperfections. Certain characteristics of cameras such as non-uniformity in solid-state cameras necessitate calibration of the detector data. Other

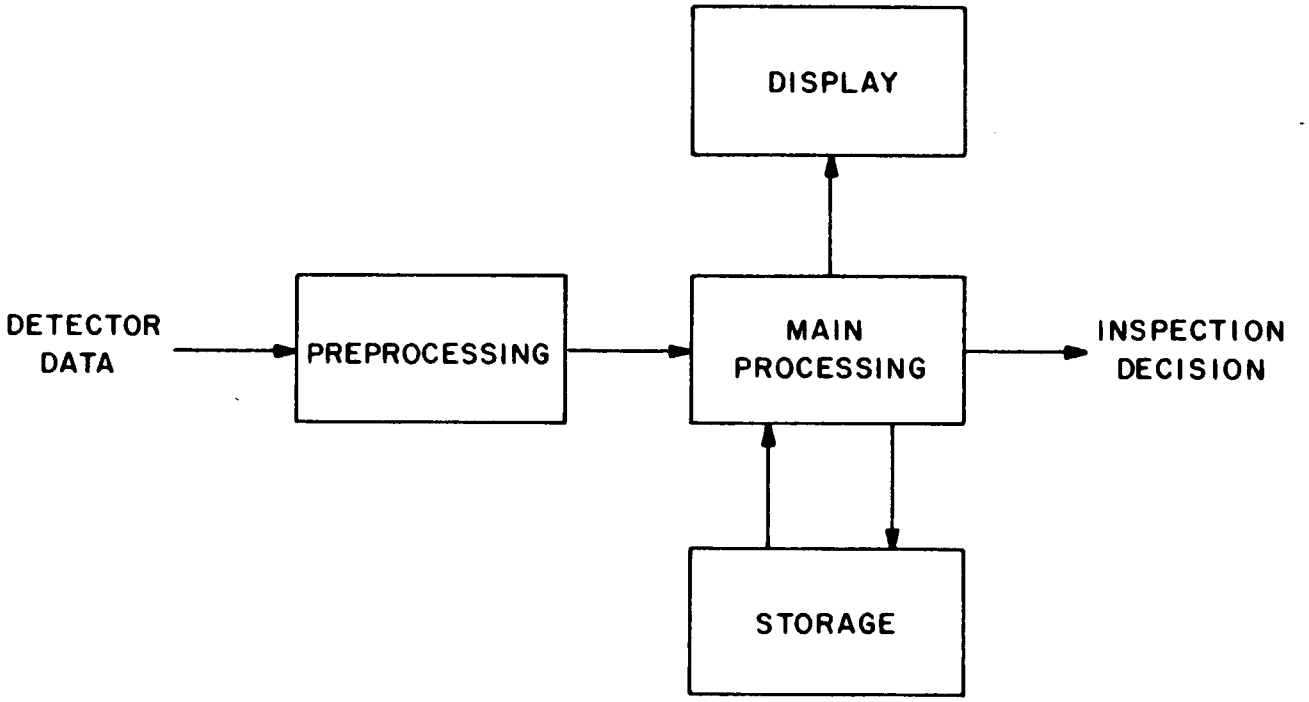

Figure 2.3. Possible functions of the AVI system processor.

preprocessing functions are generally included to reduce the volume of data. The need for data reduction is well appreciated in image-based AVI systems where every second one to ten million numbers are produced by the camera and need to be processed. This situation, indeed, makes systems based on gray-level images too slow and too costly for on-line inspection.

Data reduction is preferrably fulfilled by special-purpose hardware in the analog, digital, or hybrid form. For example, unnecessary signals are eliminated from analog signals by different filtering operations. This enhances the featurs needed for inspection and allows more efficient processing of the data. On the other hand, data reduciton in pictures commonly includes changing the image representation from one form to another. A large pixel array of intensity values is commonly converted to a much smaller data file representing the image boundary or other relevant description.

The *Main Processing* step accepts preprocessed data and produces a decision concerning the object under test. Algorithms used for processing and decision-making are generally borrowed from image processing and pattern recognition fields. These disciplines have provided techniques for other types of image analysis and decision-making (eg., medical, military) for some time, but they are only beginning to supply useful algorithms for industrial vision. Techniques developed for other applications must be adopted to meet the needs of industrial vision.

Choosing processing algorithms for a certain application, as the design of the whole AVI system, is still based on experimentation and

gusswork; there is no systematic procedure for it. In this respect, it is still very much an art. Acquisition of a good image and its appropriate reprsentation are indispensable in eliminating the need for complicated, time-consuming algorithms. Poor image qualities cannot necessarily be compensated by even sophisticated processing algorithms, while minor changes in illumination may redue the complexity of the required algorithm significantly. The influence of image encoding, on the other hand, emanates from the fact that it will to a high degree determine what processing algorithms are applicable.

This report does not present processing techniques. These techniques are covered in image processing literature comprehensively (Gonzalez and Wintz [1977], Pratt [1978], Rosenfeld and Kak [1982], Andrews [1978], Batchelor [1978], Castleman [1979], Batchelor et al. [1985]).

Processor architectures and languages presently constitute two areas of intensive research in AVI systems and image processing, in general. The problem is viewed by different people from different angles.

For some researchers an image processing language (or more correctly system) should consist of a library of routines with standard calls and written in a high-level language such as Fortran. Such systems utilize existing operating systems of computers and consist of the following categories of functions: 1) utilities; 2) arithmetic operations; 3) geometrical manipulation; 4) image display; 5) image enhancement; 6) image analysis; and 7) decision-making methods. There are already a large number of

these systems (e.g., PAX, SLIP, GLOL, VICAR, IMPROC); however, only few of them include all the seven categories of functions.

Another group of researchers believe that a command language consiting of assembly language macros for most parts and high-level routines for some parts must be developed. The advantage of such a system is its higher (about twice) efficiency in time and memory usage. Portability seems to be a problem for such a language. However, it does not constitute a big problem because there are only a few machines which are very commonly used for image processing tasks.

Searching for alternative computer architectures and languages more suitable for image processing is another active reseearch area. The philosophy is that if a problem implies a specific structure for a solution, it will be solved more efficiently on a machine and by a language which reflect that structure. Here parallel architectures and multiprocessors are more likely to provide desired systems.

AVI system processors should be capable of accomplishing pictorial, numerical, structural, and intelligent processings. They must also incorporate a *learning* capability. That is, the machine must have the ability to extract certain informatin from the object and to form a model of the object from one or more typical samples. This information will be used later by the system to recognize objects of the same type. This capability increases the usefulness and flexibility of AVI systems.

2.4 Automatic Metal Surface Inspection

Automation of visual metal-surface inspection is not a new problem, but it is a difficult one. The difficulties are due to metal production processes, component geometries, metal surface characteristics, and lighting arrangements. Deposition of lubricants, oil, or dirt on the metal surface is a common problem in the production of metal parts or strips. This changes the surface brightness and thus reflectivity, complicating the on-line inspection. Even without foreign material, surfaces of metals such as steel inherently have highly varying brightnesses which create the same kind of problem. Parts and products made from metals often have complex shapes and geometries. In addition, shadows produced in images as a result of product shape and lighting introduce their own complications. These complexities make the tasks of scaning product surface and extracting inspection information from images quite difficult.

The inherent problems mentioned above have limited the advancement of visual metal-surface inspection for many years. Most metal inspection tasks are still performed off-line by human inspectors. Dimensional measurements of defects are performed manually with the aid of such instruments as *Stylus Profilers* and *Light-section Microscopes*. Both these devices measure the profile along a line on the surface; they are both slow, and their use requires some degree of skill. Stylus instruments are more appropriate for measuring surface finishes because their sensitivity is higher and the stylus cone imposes a limitation on the depth-to-wide ratio

of flaws which can be wholly sensed by the stylus. Moreover, slight carelessness in using stylus instruments will damage the object under test and the instrument itself. The Light-section Microscope, on the other hand, is a non-contact instrument and is more suited to measuring deep roughnesses and flaws.

Little work pertinent to automatic visual metal-surface inspection is reported in the literature. We shall categorize different metal surface inspection problems into *surface finish monitoring*, *defect detection* and *defect measurement*. A brief survey of each cathegory is given below.

2.4.1 Surface Finish Monitoring

Characteristics of metal surfaces depend on the surface material and the processing method. Surface roughness, waviness, graininess, spottiness, and streakiness are characteristics which are of concern in many applications. Weszka and Rosenfeld [1976] have evaluated a large number of features for surface texture qualification. Gray level images of certified samples are utilized in the study and three features with good performance have been found.

Another work in this category is reported by Don et al. [1984]. A tree classifier is used to classify metal surface samples based on their texture into six different classes. The experiment uses 288 64 x 64 gray level images. Results show better than 90% correct classification. Inari [1972] discusses a different approach for monitoring surface roughness. He uses scattering of laser on a metal surface to determine surface texture quality. The system does not include any lens or other optical components. The

nature of the diffraciton pattern and its distribution can be utilized to determine surface characteristics. Although the method is somewhat limited, it can provide efficient solution for certain problems.

2.4.2 Defect Detection

Detection of defects on metal surfaces has received more attention than defect measurement or surface finish monitoring. This is probably because defect detection is easier and is more widely needed than the other two tasks.

Over the last fifteen years a good deal of work has gone into the development of laser scanners for on-line inspection of moving metal strips. The first scanners actually used fluorescent tubes as the light source and a row of photocells as the detector. These devices were not very successful due to lack of sensitivity to small defects on metal surfaces. The operation of these scanners, known as *image scanners*, was based on collection of reflected light from an illuminated band of metal surface by a lens drum. A complete description of image scanners is given by Brook [1971].

The advent of lasers brought a new generation of scanners, called the *flying-spot* scanners. These devices scan a light spot across the surface and register the scattered light by a number of photomultipliers or a solid-state diode array. The performance of these scanners is much better than that of the image scanners and they are under operation or experimentation in many places. West [1982] describes three different scanners, one of which can be used for detection of defects on metal surfaces. Pinholes of diameters

25 μm and up can be detected on metal strips with the width of 1.2 m moving at a speed of 5 m/s.

Aalderink and de Jone [1976] discuss the development of a scanner for on-line inspection of cold-rolled steel sheet. The scanner uses tungsten filament lamps for illumination and arrays of photodiodes for detection. It is expected that the system performs satisfactorily up to speeds of 30 m/s.

Investigations have sought to complement the detection capability of scanners by adding defect classification ability to them. Norton-Wayne and his colleagues have been working steadily on this subject since 1971. The results are still not conclusive. Norton-Wayne and Hill [1974] considered ten classes of defects on metal sheets rolling with a speed up to 25 m/s. Information useful for classification is obtained from the shape of the output signal of the scanner and binary images obtained from thresholding of consecutive scanner signals. A threshold detector gates information into a pattern recongition machine only when a certain threshold is exceeded. This reduces the huge volume of information before performing classification. The best results obtained are 77% correct clasificaiton for a linear classifier using nine features. Norton-Wayne, Hill, and Brook [1977] and Norton-Waye, Watts, and Hill [1980] report on the progress of the project. The number of classes of defects (for steel strips) has been increased to the more realistic value of 35, and the best result is 55% correct classification of the defects.

Logan and Macleod [1974] also report a study for identification of defects on rolling metal surfaces. The system uses binary images

constructed from scanner data and distinguishes five defect classes. A number of classifiers are evaluated, with the most successful ones being non-parametric trained classifiers givning 87% to 97% correct classification of defects.

A feasibility study of defect classification is presented by Saridis and Brandin [1976]. They use a television camera with its vertical axis eliminated and acquire a visual signal which represents surface characteristics. This signal goes through some analog processing and alerts a computer when a possible defect is detected. The computer performs classification of the defects.

A laser scanner for detection of flaws on machined parts is described by Hirata et al. [1982]. A laser beam scans the surface of an object. Deviations from the diffraction pattern of a flawless area are detected by a photodetector through an optical fiber bundle. Fadl and Parsons [1978] describe a laser scanner built on the above principle to detect defects on rotating parts.

Development of a system for on-line inspection of hot steel slabs is discussed by Suresh et al. [1983]. The moving surface is scanned by a 2048-element linear array, while the slab position is determined by a second array collecting data longitudinally. An array processor and a minicomputer process the image data and produce a report about the slab under test. Laboratory experiments sugest that the system can properly detect and identify surface flaws on-line. Reich and Coleman [1976] describe a flaw detection system for 100% inspection of small caliber

ammunition. A line of laser light scans the surface of the spinning cartridge case. Fiber optics probes collect the light scattered from the case surface and deliver it to several photomultipliers. Signals from these devices are fed to a computer which declares the part as accepted or rejected. The system inspects 20 cartridge cases each second.

Development of an interesting system is reported by Graham and Choong [1982]. The system utilizes a robot for inspection and polishing of complex geometry components. Six degrees of freedom between the camera and component provide sufficient flexibility for an intelligent model-based vision system to acquire suitable images through a 64 x 64 solid-state camera. The system controls component orientation, viewing geometry, and lighting intensity to obtain satisfactory images. Three PDP-11/23's control the operation of the system.

Batchelor and Williams [1979] study detection of defects on the internal surfaces of cylinders used in the automotive industry. Necessary image analysis is determined by an interactive image analyzer called SUSI. Signal processing methods which improve the results previously obtained by the authors are introduced.

Using the theory of light scattering from rough surfaces, Mundy [1982] proposed a method of image analysis which improves contrast of the surface image when a defect is present and thus makes defect detection on metal surfaces easier. The method, however, requires two images obtained from normal and grazing illumination.

Perkins [1983, 1984] studies inspection of objects with complex appearances such as those with many components. He uses a model-based approach which teaches the system about the object and allows different inspection tasks to be performed.

Finally, inspection of the surfaces of ball and roller bearing components is discussed by Sevcik [1982] and Barton and Kusenberger [1977, 1982]. They introduce devices which inspect these components through deviations form normal conditions (flawless surface) of the scattered laser light.

2.4.3 Defect Measurement

Automatic measurement of the dimensions of flaws is indispensable in some critical applications. Nevertheless, fulfillment of such a task from visual data is quite difficult. This is evident by the few reports published on the subject.

Klingsporn [1980] describes a system for automatic measurement of defect dimensions on superfinished spherical surfaces. he uses an optical arrangement to sense the amplitude and distribution of the diffraction pattern produced by the defect. Then from theory he shows that certain parameters of the pattern are related to the defect width/diameter and depth and thus measures defect dimensions from these parameters. The inspection requires less than 30 minutes with the system as opposed to five hours for a manual approach. To evaluate the accuracy of measurements, Klingsporn measures a number of calibrated defects and reports standard

deviations of 120 and 12 μin for scratch width and depth and 230 and 36 μin for pit width and depth.

In an effort to measure surface waviness from surface profile, Don et al. [1984] use a surface scattering model to obtain the surface profile from an image of the surface. Images used in this study were obtained by a microscope. The accuracy of the measurement has not been assessed.

Finally, Porter and Mundy [1982] discuss the development of a profile sensing system for inspection of metal surfaces. The system operates based on optical triangulation. A laser beam scans the metal surface normally while its trace is registered by a camera from an angle. The analysis of the images and control of the system necessitates the use of four general-purpose computers. Performance evaluations show that the specifications of 0.001 inch depth resolution, 0.002 inch lateral resolution, and one milion pixels per second can be met by the system. However, signal sensitivity to reflectance-changes degrades the system performance.

2.5 Concluding Remarks

Inspection of parts and products is an inevitable and costly task in industry. AVI offers effective and efficient solutions to the problems and weaknesses of manual inspection. Technological advancements have made AVI systems more powerful, more economical and feasible for many inspection tasks. However, much advancement is needed to render AVI a mature field.

Design of AVI systems is still very much an art. Each application requires the development of a specific solution and demands much design experience. The choice of system components plays an essential role in the success or failure of the system. Factors seemingly unimportant in the design of AVI systems may drastically affect the performance of the system.

Automatic inspection of metal surfaces faces serious difficulties at present. Understanding the nature of light scattering from metal surfaces of different characteristics is indispensable in the development of meaningful methods for automated metal surface inspection. Models which properly describe light scatteirng of metal surfaces and allow accurate measurement of the surface topography must be developed. The present conditions of the field suggest that it will be some time before this can be achieved.

CHAPTER 3

LIGHT SCATTERING MODELS FOR FLAWS ON METAL SURFACES

When light impinges on metal surfaces, it is modulated by the surface to carry information about its structure. Characteristics of the returned light and the amount of information that it carries are dependent on the light wavelength, the angle of incidence, and the surface characteristics. If the rms variations in the height and distribution of the hills and valleys of the surface is much less than the light wavelength, the surface is called *specular* and acts as a mirror or reflector. The reflected light in this case carries almost no information about the surface topology. As the surface roughness is increased, the returned light is more scattered and it carries more information about the surface characteristics. The returned light may be diffracted into certain angles or it may be scattered in many directions. A vast amount of information concerning the surface is contained in the diffracted and scattered light patterns.

Visual inspection of metal surfaces by machines relies on the feasibility and accuracy of information extraction from the light patterns modulated by the surface. These patterns must be correlated with the surface topology through understanding the light scattering mechanisms of metal surfaces and establishing scattering models for the surfaces.

This chapter is devoted to the study of several light scattering theories and the development of scattering models for flaws on metal surfaces. Certain approximations for flaw cross-sections are introduced, and an

approximate theory based on consideration of spherical waves from a point source in the Helmholtz intergral is developed. Next, a second formulation founded on scalar diffraction theory and tangent plane approximations is considered, and the relationship between the scattered light intensity and flaw dimensions is investigated. Finally, a method obtained through quantum perturbation theory is applied to the problem and modeling aspects are studied. Boldfaced constants or variables denote *complex* quantities or *vectors* throughout this work.

3.1 Surface Profile Approximations

Metal surfaces have a high degree of variability in their characteristics. The surface topology shows no specific pattern or consistency in variations in the surface roughness, and the reflectivity varies at different points on the surface. These attributes render the mathematical description of the surfaces impractical if not impossible. On the other hand, theories used to study light scattering from metal surfaces will require some type of mathematical description of the surface. The result is that simplifying assumptions about the surface characteristics must be adopted before analytical studies can be made.

Surfaces which are considered in this study are those of machined parts with a periodic-like roughness. The light incident on these surfaces diffracts into a band with a specific orientation on the observation plane. If a flaw such as a scratch comes under light incidence, the light diffracted from the flaw forms a second band at a different angle from the first one. (It

is assumed here that the scratch does not lie exactly on the periodic grooves of the surface). As a result, the light diffracted from the flaw and that from the background surface can be sensed separately with minimum impact on one another. Therefore, we define a flaw-free surface as one for which the flaw sensor detects a minimal and almost fixed value. Such a surface has an almost zero reflection coefficient as seen by the flaw sensor. A flaw on an otherwise flaw-free surface signifies a region with a non-zero reflection coefficient which acts as a concave cylindrical or concave spherical reflector on a completely light-absorbing background.

Considering the above discussion, we will regard the profile of the machined surface as zero everywhere except for the region of the flaw. In this region, the shape of the flaw will determine the functional form of the profile. An appropriate approximation must be made. This approximation must be flexible in accommodating various shapes and yet remain simple enough to yield managable mathematical relations.

Generally, when flaws occur on metal surfaces, some residues are left or the metal is deformed to create hills on the sides of the flaw. These hills, which we call *ridges*, also act as scatterers and must be included in the analysis. Figure 3.1 shows three examples of surface profiles which use sinusoidal functions. The first profile illustrates a clean flaw while the other two have ridges on one or both sides. These approximations are somewhat limited in that the shape is functionally not flexible and a certain degree of symmetry about the z-axis is assumed.

$$z(x) = \begin{cases} d_o \dfrac{\cos\omega_\ell - \cos x}{1 - \cos\omega_\ell} & -\omega_\ell \le x \le \omega_\ell \\ 0 & \text{elsewhere} \end{cases}$$

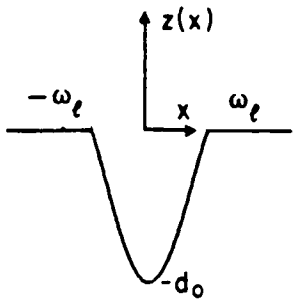

(a)

$$z(x) = \begin{cases} d_o \dfrac{\cos\omega_\ell - \cos x}{1 - \cos\omega_\ell} & -\omega_\ell \le x \le \pi \\ 0 & \text{elsewhere} \end{cases}$$

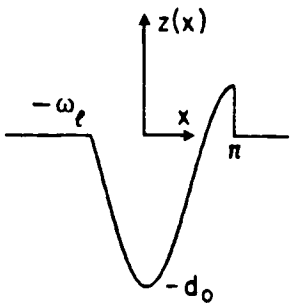

(b)

$$z(x) = \begin{cases} d_o \dfrac{\cos\omega_\ell - \cos x}{1 - \cos\omega_\ell} & -\pi \le x \le \pi \\ 0 & \text{elsewhere} \end{cases}$$

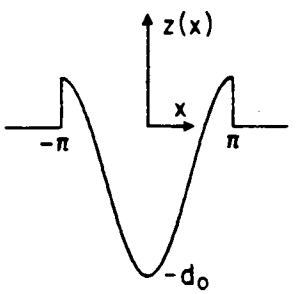

(c)

Figure 3.1. Sinusoidal approximations for defective surface profiles.

An alternative surface profile is indicated in Figure 3.2. This piecewise linear model is more universal and flexible than the sinusoidal model because there is no limitation on the number, lengths, or angles of the segments which constitute the profile. Furthermore, since the segments are represented by first-order polynomials, the mathematical analysis will probably be simpler. The mathematical description of the profile is:

$$z(x) = \begin{cases} -a_j x + b_j & -\omega_m \le x \le 0 \\ a_j x + b_j & 0 \le x \le \omega_m \\ 0 & \text{elsewhere} \end{cases} \tag{3.1}$$

where

$$a_j = \frac{d_{j-1} - d_j}{\omega_j - \omega_{j-1}} \tag{3.2}$$

$$b_j = \frac{d_j \omega_{j-1} - d_{j-1} \omega_j}{\omega_j - \omega_{j-1}} \tag{3.3}$$

This model also assumes symmetry about the z-axis, but not about the ridge axes. In the theoretical developments in this chapter we will tolerate this symmetry limitation since analysis in the absence of the symmetry was found to be complex and very involved.

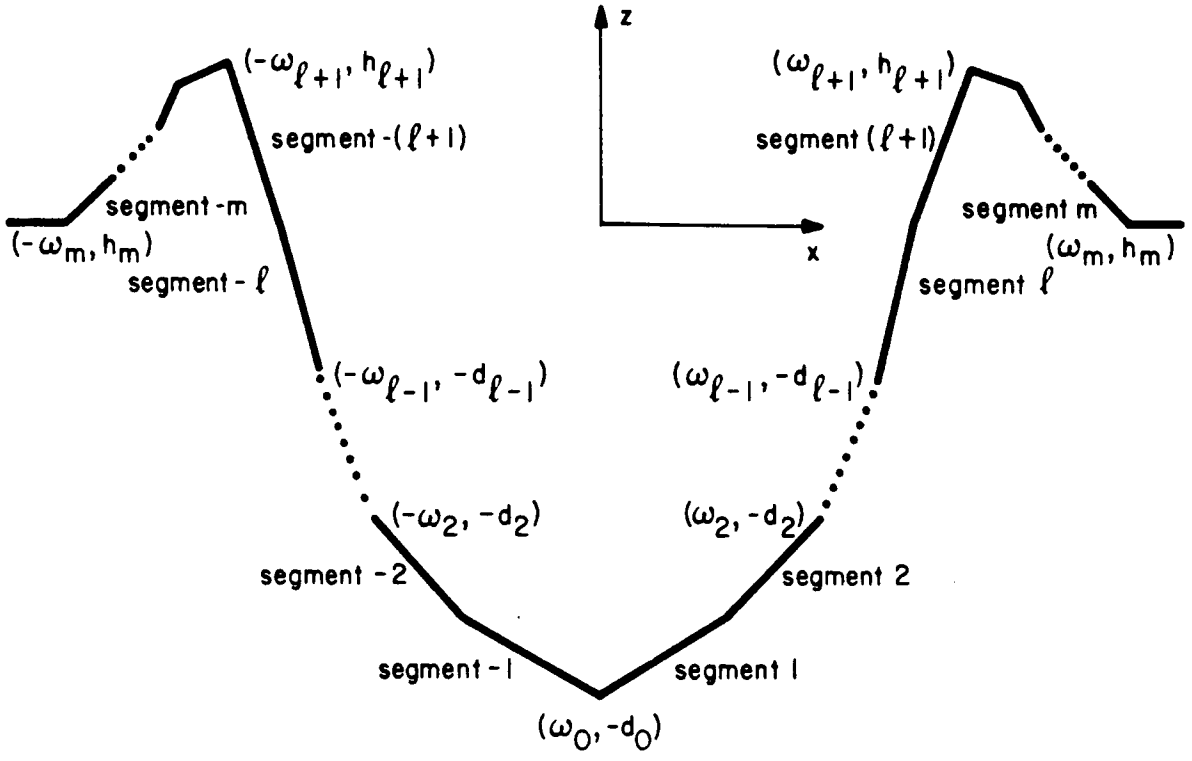

Figure 3.2. Piecewise linear approximation of a defective surface profile.

3.2 Light Scattering Theories and Models

As the nature of light is electromagnetic radiation, its various field quantities can be determined through the solution of the *wave equation.* In case of light scattering from metal surfaces, the boundary conditions for the solution are determined by the characteristics of the metal surface. Among different components of the electromagnetic field, the electric field intensity E is responsible for optical processes and will be considered in this discussion.

Consider the problem of linearly-polarized monochromatic light (such as laser light) striking a metal surface. Substitution of the harmonic electric field intensity $E(P_0,t)$ in the scalar wave equation would necessitate that the complex field amplitude

$$E(P_0) = E(P_0)\exp[-i\Phi(P_0)] \tag{3.4}$$

satisfy the *Helmholtz equation* (Goodman [1968]). That is:

$$\nabla^2 E(P_0) + k^2 E(P_0) = 0 \tag{3.5}$$

where ∇^2 is the *Laplacian operator* and k is the *wave number* given by:

$$k = \frac{2\pi}{\lambda} \quad . \tag{3.6}$$

This means that the field wave will propagate so that its amplitude and phase always satisfy Equation 3.5. Assuming that the metal is perfectly conducting results in the boundary condition that the tangential component of the electric field intensity vanishes on the metal surface.

The Helmholtz equation and the Green's Theorem, with a spherical wave as the Green's function, can be used to determine the field at a point P_0 (Goodman [1968], Beckmann and Spizzichino [1963]). Assume that P_s is a variable point on surface S around an observation point P_0 and R_0 is the distance between P_s and P_0. The field at P_0 can be found in terms of the field and its normal derivative on the surface S as:

$$\mathbf{E}(P_0) = \frac{1}{4\pi} \int\int_S \left\{ \frac{\partial \mathbf{E}(P_s)}{\partial \mathbf{n}} \left[\frac{\exp(ikR_0)}{R_0} \right] - \mathbf{E}(P_s) \frac{\partial}{\partial \mathbf{n}} \left[\frac{\exp(ikR_0)}{R_0} \right] \right\} ds \tag{3.7}$$

This equation is known as the *integral theorem of Helmholtz and Kirchhoff* and is the basis of several field scattering theories.

3.2.1 The Point-Source Approximation

Determination of the scattered field from the integral theorem of Helmholtz and Kirchhoff requires that the electric field and its normal derivative on the scattering surface be known. Unfortunately, the exact values of these quantities are generally not known and must be approximated. Various approximations for $\mathbf{E}$ and $\partial\mathbf{E}/\partial\mathbf{n}$ will produce different theories which may prove useful under cetain conditions. It is

common in wave scattering theories to consider a global normal for the whole surface. However, since this is not always a good or valid approximation, we attempt in this section to look at the problem considering a point light source and local normals.

Assume that a linearly polarized light source at point P_ℓ radiates spherical waves onto a surface S at an angle α from the surface global normal $\mathbf{n}_g$. With the geometry shown in Figure 3.3, the radiated field at a point P_s on the surface is:

$$\mathbf{E}(P_s) = \frac{\exp(ikR_\ell)}{R_\ell} \tag{3.8}$$

We show in Appendix A that if flaw dimensions are much larger than the light wavelength λ and much smaller than the distance of the excitation and observation points from the surface, then the field observed at point P_o is:

$$\begin{aligned}\mathbf{E}(P_o) = \frac{L}{2\pi}\mathbf{F}_1\Bigg\{&\sum_{j=0}^{\ell}\left(\frac{\omega_j-\omega_{j-1}}{d_{j-1}-d_j}-\frac{\omega_{j+1}-\omega_j}{d_j-d_{j+1}}\right)\mathbf{E}\,i(iF_2+iF_3d_j)\\&+\sum_{j=\ell+1}^{m}\left(\frac{\omega_j-\omega_{j-1}}{h_j-h_{j-1}}-\frac{\omega_{j+1}-\omega_j}{h_{j+1}-h_j}\right)\mathbf{E}\,i(iF_2-iF_3h_j)\Bigg\}\end{aligned} \tag{3.9}$$

where

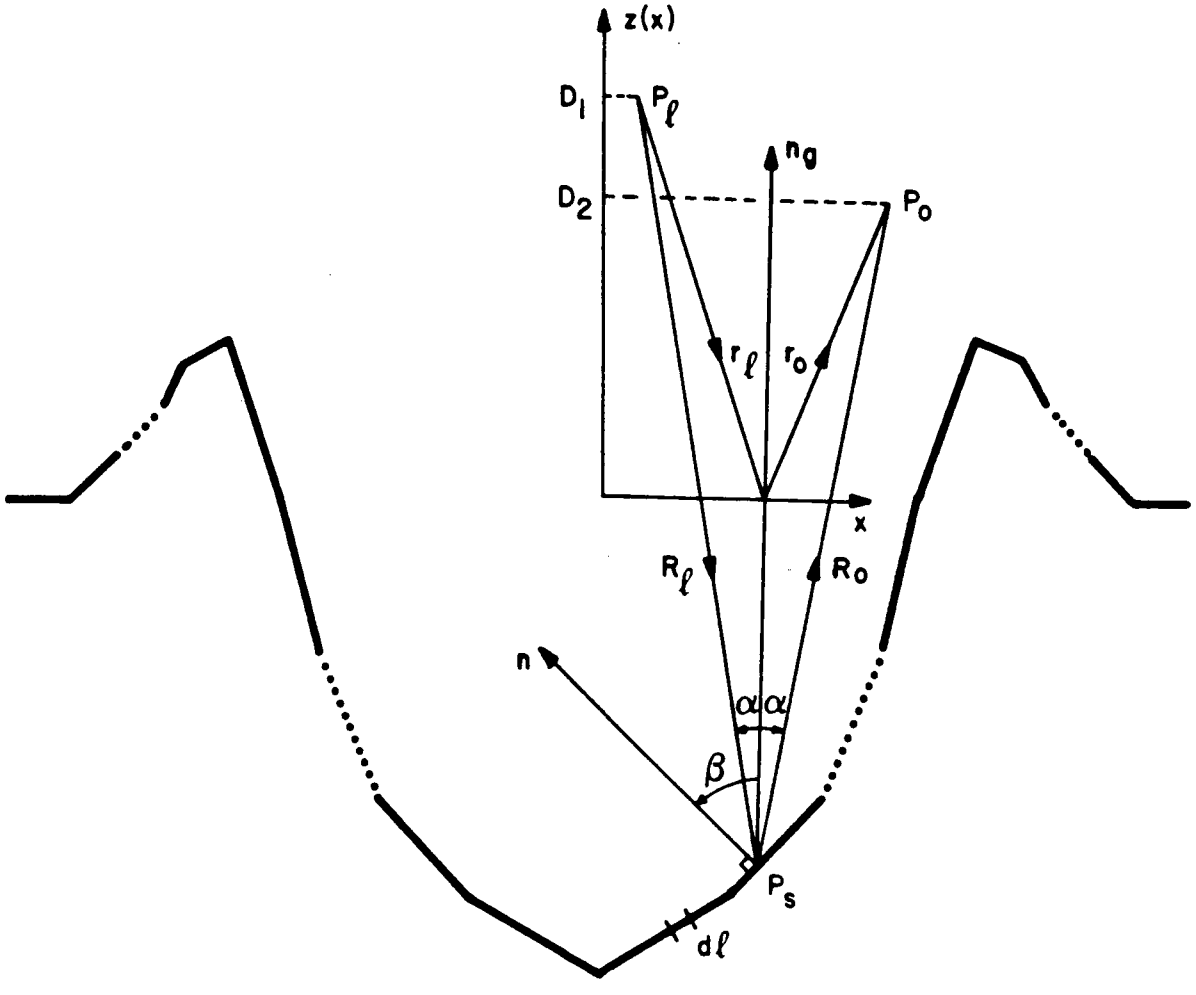

Figure 3.3. Light scattering from the piecewise linear model.

$$F_1 = \frac{-i4kD_1}{(r_o D_1 + r_\ell D_2) r_\ell} \exp\left(ik \frac{r_o^2 D_1 + r_\ell^2 D_2}{r_o D_1 + r_\ell D_2} \right) \tag{3.10}$$

$$F_2 = k \frac{(D_1 + D_2) r_\ell r_o}{D_1 r_o + D_2 r_\ell} \tag{3.11}$$

$$F_3 = k(D_1 + D_2) \tag{3.12}$$

and

$$Ei(z) = \int_{-\infty}^{z} \frac{e^t}{t} dt \tag{3.13}$$

The ensemble mean light intensity at point P_0 is given by $<|E(P_0)E^*(P_0)|>$. Using Equation 3.9 to obtain the light intensity will produce a quite involved expression which is not given here. However, the dependence of E on the d_j and ω_j indicates that the observed light is a function of shape, depth, and width of the scratch. In addition, the scratch length, the light wavelength, the light source location, and the observation point affect the observed light intensity.

In order to see the nature of the relationship between the scattered light intensity and the scratch characteristics, we assume that the scratch has a V-shaped profile (this corresponds to $m=1$ in the profile of Figure 3.2), the Exponential Integral Function Ei can be approximated by its first

order approximation exp(-z)/z (since $F_2 + F_3 d_o >> 1$), and $F_2 >> F_3 d_o$, then

$$E(P_o) \approx \frac{F_1}{F_2} L \frac{\omega_1}{d_o} \exp(-i F_2)[1 - \exp(-i F_3 d_o)] \tag{3.14}$$

and the functional form of the observed light intensity is:

$$\langle |E(P_o) E^*(P_o)| \rangle \approx |F_1|^2 \frac{F_3^2}{F_2^2} (2L)^2 (2\omega_1)^2 \left(\frac{\sin \frac{F_3 d_o}{2}}{\frac{F_3 d_o}{2}} \right)^2 . \tag{3.15}$$

Equation 3.15 suggests that the observed light intensity increases with scratch width or scratch length parabolically, but its dependence on the scratch depth is more complex. More importantly, the equations indicate that the observed light intensity and the scratch depth do not have a one-to-one relationship. This means that scratches of certain different depths produce the same effect on the incident light and that the measurement of defect depth from the scattered light faces a uniqueness problem.

Using sinusoidal scratch profiles shown in Figure 3.1 on page 43 produces similar expressions for the observed light intensity but with more complex functions of ω_j and d_j. These expressions are not presented here.

3.2.2 The Tangent-Plane Approximation

Beckmann (Beckmann and Spizzichino [1963]) in his study of radio-wave scattering used the integral theorem of Helmholtz and Kirchhoff to

develop a relatively simple relationship for the calculation of the field scattered on a surface. He assumed that the surface did not include sharp irregularities (the radius of curvature of irregularities larger than the light wavelength λ) and approximated the field and its normal derivative at each point on the surface by similar quantities existing on a plane tangent to the surface at that point. Furthermore, he assumed linearly polarized plane waves and perfect conductivity of the surface. Then using the notation illustrated in Figure 3.4, he showed that if the rough surface S is under light incidence from $x=-X$ to $x=X$ and $y=-Y$ to $y=Y$, then the scattering coefficient (normalized field intensity) is:

$$\rho = \frac{C(\theta_i, \theta_r, \phi)}{4XY} \int\int_S \exp(i\,\mathbf{u}\cdot\mathbf{r})\,dx\,dy \tag{3.16}$$

where

$$C(\theta_i, \theta_r, \phi) = \frac{1 + \cos\theta_i \cos\theta_r - \sin\theta_i \sin\theta_r \cos\phi}{(\cos\theta_i + \cos\theta_r)\cos\theta_i} \tag{3.17}$$

$$\mathbf{u} = \mathbf{K}_i - \mathbf{K}_r = u_x \mathbf{a}_x + u_y \mathbf{a}_y + u_z \mathbf{a}_z \tag{3.18}$$

$$u_x = \frac{2\pi}{\lambda}(\sin\theta_i - \sin\theta_r) \tag{3.19}$$

$$u_y = \frac{-2\pi}{\lambda}(\sin\theta_r \sin\phi) \tag{3.20}$$

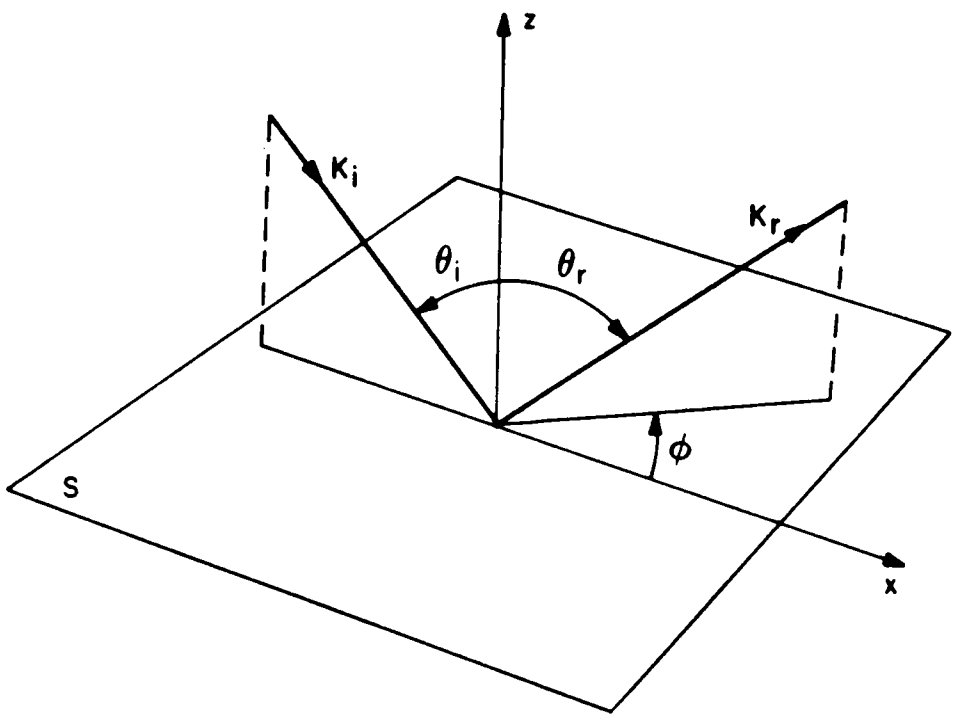

Figure 3.4. General light scattering geometry.

$$u_z = \frac{-2\pi}{\lambda}(\cos\theta_i + \cos\theta_r) \tag{3.21}$$

and

$$\mathbf{r} = x\,\mathbf{a}_x + y\,\mathbf{a}_y + z(x)\,\mathbf{a}_z\,. \tag{3.22}$$

In this section we study light scattering from a scratch with a piecewise linear profile as shown in Figure 3.2 on page 45 and extending from y = - L to y = + L. We show in Appendix B that the scattering coefficient is:

$$\rho = \frac{(2L)C}{2X\,Y\,u_x}(\sin u_x X - \sin u_x \omega_m) + \frac{(2L)C}{2X\,Y}\left[\sum_{j=1}^{\ell}\frac{G_j + iH_j}{u_x^2 + a_j^2 u_z^2} + \sum_{j=\ell+1}^{m}\frac{G_{rj} + iH_{rj}}{u_x^2 + a_{rj}^2 u_z^2}\right] \tag{3.23}$$

where

$$C = \frac{1 + \cos(\theta_i + \theta_r)}{\cos\theta_i(\cos\theta_i + \cos\theta_r)} \tag{3.24}$$

$$G_j = S_j \cos d_j u_z + T_j \sin d_j u_z \tag{3.25}$$

$$H_j = T_j \cos d_j u_z - S_j \sin d_j u_z \tag{3.26}$$

$$S_j = u_x \sin u_x\omega_j - u_x \sin u_x\omega_{j-1}\cos q_j - a_j u_z \cos u_x\omega_{j-1}\sin q_j \tag{3.27}$$

$$T_j = u_x \sin u_x\omega_{j-1}\sin q_j + a_j u_z \cos u_x\omega_j - a_j u_z \cos u_x\omega_{j-1}\cos q_j \tag{3.28}$$

$$q_j = (\omega_j - \omega_{j-1}) a_j u_z \tag{3.29}$$

$$a_j = \frac{d_{j-1} - d_j}{\omega_j - \omega_{j-1}} \tag{3.30}$$

$$G_{rj} = S_{rj} \cos h_j u_z - T_{rj} \sin h_j u_z \tag{3.31}$$

$$H_{rj} = T_{rj} \cos h_j u_z + S_{rj} \sin h_j u_z \tag{3.32}$$

$$S_{rj} = u_x \sin u_x \omega_j - u_x \sin u_x \omega_{j-1} \cos q_{rj} - a_{rj} u_z \cos u_x \omega_{j-1} \sin q_{rj} \tag{3.33}$$

$$T_{rj} = u_x \sin u_x \omega_{j-1} \sin q_{rj} + a_{rj} u_z \cos u_x \omega_j - a_{rj} u_z \cos u_x \omega_{j-1} \cos q_{rj} \tag{3.34}$$

$$q_{rj} = (\omega_j - \omega_{j-1}) a_{rj} u_z \tag{3.35}$$

and

$$a_{rj} = \frac{h_j - h_{j-1}}{\omega_j - \omega_{j-1}} \quad . \tag{3.36}$$

u_x and u_z are defined in Equations 3.19 and 3.21.

The light intensity observed at an angle θ_r can be obtained from $<|\rho\rho^*|>$. Considering the complexity of ρ, we do not derive the relationshiop here. Instead, we make two simplifying assumptions as follows. We let angles of incidence and observation be equal; then u_x becomes zero and significant reductions in equations result. Also, the

shape of the scratch profile is considered as a V to eliminate summation of many terms. Then the result is:

$$\rho = \frac{(2L)}{(2Y)}\left\{\left(1 - \frac{\omega_1}{X}\right) - \frac{\omega_1}{X}\left(\frac{\sin d_o u_z}{d_o u_z}\right) + i\,\frac{\omega_1}{X}\left(\frac{1 - \cos d_o u_z}{d_o u_z}\right)\right\} \tag{3.37}$$

and

$$<|\rho\,\rho^*|> = \frac{(2L)^2}{(2Y)^2}\left\{\left(1 - \frac{\omega_1}{X}\right)^2 - 2\,\frac{\omega_1}{X}\left(1 - \frac{\omega_1}{X}\right)\frac{\sin d_o u_z}{d_o u_z} + \left(\frac{\omega_1}{X}\right)^2\left(\frac{\sin \frac{d_o u_z}{2}}{\frac{d_o u_z}{2}}\right)^2\right\} \tag{3.38}$$

where

$$d_o u_z = -\,4\pi\,\frac{d_o}{\lambda}\cos\theta_i \ . \tag{3.39}$$

Dependence of the light intensity scattered from a defective metal surface on the flaw length, width, and depth as well as on the light wavelength, the angles of incidence and observation, and the area under light incidence is witnessed by Equation 3.38. Furthermore, this scattering model states that for a certain laser head oriented at a fixed angle and impinging light on a flaw of constant width, the observed scattered light intensity changes with depth as:

$$I \sim a + b\left(\frac{\sin 2\alpha d_o}{2\alpha d_o}\right) + c\left(\frac{\sin \alpha d_o}{\alpha d_o}\right)^2 \tag{3.40}$$

where a, b, c, and α are constants. here again the lack of uniqueness in the relationship of defect depth and the scattered light intensity is observed.

If the flaw has a varying width but a constant depth, the model suggests that the scattered light changes with the width in the following manner:

$$I \sim a + b\,\omega_l + c\,\omega_l^2 \,. \tag{3.41}$$

Finally, the scattering model of Equation 3.40 gives the relationship between the scattered light and the angle of incidence and observation as:

$$I \sim a + b\left[\frac{\sin(2\alpha\cos\theta_i)}{2\alpha\cos\theta_i}\right] + c\left[\frac{\sin(\alpha\cos\theta_i)}{\alpha\cos\theta_i}\right]^2 . \tag{3.42}$$

The scattering coefficient introduced in this section is also evaluated for the sinusoidal flaw profile introduced in Part (c) of Figure 3.1 on page 43. We show in Appendix B that when the observation angle θ_r is equal to the incidence angle θ_i, the scattering coefficient ρ is:

$$\rho = \frac{2L}{2Y}\left\{\left(1 - \frac{\pi}{X}\right) + \frac{\pi}{X}\exp\left(i\,u_z d_o \frac{\cos\omega_\ell}{1-\cos\omega_\ell}\right) J_o\left(\frac{-u_z d_o}{1-\cos\omega_\ell}\right)\right\} \tag{3.43}$$

where

$$u_z = \frac{-4\pi}{\lambda} \cos\theta_i \tag{3.44}$$

and J_0 represents the Bessel function of the first kind and zero order. The scattered light observed at angle $\theta_r = \theta_i$ is:

$$\begin{aligned} <|\rho\rho^*|> = \left(\frac{2L}{2Y}\right)^2 \Bigg\{ & \left(1 - \frac{\pi}{X}\right)^2 + \left(\frac{\pi}{X}\right)^2 J_o^2\left(\frac{-u_z d_o}{1 - \cos\omega_\ell}\right) \\ & + 2\left(1 - \frac{\pi}{X}\right)\frac{\pi}{X} J_o\left(\frac{-u_z d_o}{1 - \cos\omega_\ell}\right)\cos\left(u_z d_o \frac{\cos\omega_\ell}{1 - \cos\omega_\ell}\right)\Bigg\} \end{aligned} \tag{3.45}$$

This light scattering model introduces the dependence of the scattered light on the flaw depth, width, and angle of incidence through the Bessel functions of the first kind. Even though the functional form of the dependence here is more complex than in Equation 3.38, similar conclusions result.

3.2.3 The Perturbation Theory Approximation

Assume that in the light scattering geometry of Figure 3.4, the light incidence is normal and the diffracted light is observed at an angle (θ_r,ϕ). Furthermore, assume that **r** is a vector parallel to the mean plane of the surface (x-y plane in Figure 3.4) given by:

$$\mathbf{r} = x\,\mathbf{a}_x + y\,\mathbf{a}_y \tag{3.46}$$

and **u** is the projection of $\mathbf{K}_r$ in the x-y plane given by:

$$\mathbf{u} = u_x \mathbf{a}_x + u_y \mathbf{a}_y \tag{3.47}$$

where

$$u_x = \frac{2\pi}{\lambda} \sin\theta_r \cos\phi \tag{3.48}$$

and

$$u_y = \frac{2\pi}{\lambda} \sin\theta_r \sin\phi \tag{3.50}$$

Elson and Ritchie [1971] utilized the quantum perturbation theory to obtain the probability of occurrence of various processes at the metal surface. They showed that the probability that diffuse scattered light is observed in the direction (θ_r,ϕ) in an infinitesimal solid angle $d\Omega$ for the s-polarized photons is:

$$\frac{dP^s}{d\Omega} = \frac{1}{\pi^2 A}\left(\frac{2\pi}{\lambda}\right)^4 \cos^2\theta_r \sin^2\phi \left| \int_r z(\mathbf{r}) \exp(-i\,\mathbf{u}\cdot\mathbf{r})\, d\mathbf{r} \right|^2 \tag{3.51}$$

and for the p-polarized photons is:

$$\frac{dP^p}{d\Omega} = \frac{1}{\pi^2 A}\left(\frac{2\pi}{\lambda}\right)^4\left(\cos^2\theta_r\cos^2\phi\right)\left(\frac{\sin^2\theta_r - \varepsilon}{\sin^2\theta_r - \varepsilon\cos^2\theta_r}\right)\left[1 + \left(\frac{4\varepsilon}{\varepsilon - \sin^2\theta_r}\right)^{\frac{1}{2}}\right]^2$$

$$\left|\int_r z(\mathbf{r})\exp(-i\mathbf{u}\cdot\mathbf{r})\,d\mathbf{r}\right|^2 \tag{3.52}$$

where λ is the light wavelength, A is the area under light incidence, ε is the dielectric permittivity of the metal, and $z(\mathbf{r})$ gives the height of surface roughness at $\mathbf{r}$. The total probability is:

$$\frac{dP}{d\Omega} = \frac{dP^s}{d\Omega} + \frac{dP^p}{d\Omega} = F_o(\theta_r,\phi,\lambda,\varepsilon,A)\left|\int_r z(r)\exp(-i\mathbf{u}\cdot\mathbf{r})\,d\mathbf{r}\right|^2 \tag{3.53}$$

where

$$F_o(\theta_r,\phi,\lambda,\varepsilon,A) = \frac{1}{\pi^2 A}\left(\frac{2\pi}{\lambda}\right)^4\left\{\sin^2\phi + \cos^2\phi\,\frac{\sin^2\theta_r - \varepsilon}{\sin^2\theta_r - \varepsilon\cos^2\theta_r}\left[1 + \left(\frac{4\varepsilon}{\varepsilon - \sin^2\theta_r}\right)^{\frac{1}{2}}\right]^2\right\}\cos^2\theta_r \tag{3.54}$$

is a constant for a given laser head, a certain metal, and a fixed observation point. Equation 3.53 indicates that the total probability of the observation of scattered light from a surface is proportional to the power spectrum of the surface roughness.

We show in Appendix C that for the surface profile of Figure 3.2 on page 45, the integral in Equation 3.53 is:

$$\int_r z(\mathbf{r}) \exp(-i\,\mathbf{u}\cdot\mathbf{r})\,d\mathbf{r} = \left(\frac{4 \sin u_y L}{u_x^2 u_y}\right)\left[\sum_{j=0}^{\ell}\left(\frac{d_{j+1}-d_j}{\omega_{j+1}-\omega_j} - \frac{d_j - d_{j-1}}{\omega_j - \omega_{j-1}}\right)\cos u_x \omega_j \right.$$

$$\left. + \sum_{j=\ell+1}^{m}\left(\frac{h_j - h_{j-1}}{\omega_j - \omega_{j-1}} - \frac{h_{j+1} - h_j}{\omega_{j+1} - \omega_j}\right)\cos u_x \omega_j\right] \tag{3.55}$$

where $d_j = h_j = 0$ and $\omega_j = \infty$ for $j > m$ or $j < 0$.

Equation 3.55 can be expressed in another useful form. Assume that d_j and h_j are fractions of d_o, and ω_j is a fraction of ω_m as defined in the following equations:

$$\begin{aligned} d_j &= \alpha_j d_o \qquad && j = 1, 2, \ldots, \ell \\ h_j &= -\alpha_j d_o \qquad && j = \ell+1, \ell+2, \ldots, m \\ \omega_j &= \beta_j \omega_m \qquad && j = 1, 2, \ldots, m-1 \end{aligned} \tag{3.56}$$

Then Equation 3.55 can be expressed as:

$$\int_r z(\mathbf{r}) \exp(-i\,\mathbf{u}\cdot\mathbf{r})\,d\mathbf{r} = \left(\frac{8 \sin u_y L}{u_x^2 u_y}\right)\left[\sum_{j=0}^{m}\left(\frac{\alpha_{j+1} - \alpha_j}{\beta_{j+1} - \beta_j} - \frac{\alpha_j - \alpha_{j-1}}{\beta_j - \beta_{j-1}}\right)\cos u_x \omega_j\right]\left(\frac{d_o}{2\omega_m}\right) \tag{3.57}$$

where $\alpha_j = 0$ and $\beta_j = \infty$ for $j > m$ or $j < 0$.

The expression inside parentheses in the above summation is constant for a fixed shape regardless of the size of the profile. We call this term the *shape constant* and denote it by Ψ_j. Then:

$$\Psi_j = \frac{\alpha_{j+1} - \alpha_j}{\beta_{j+1} - \beta_j} - \frac{\alpha_j - \alpha_{j-1}}{\beta_j - \beta_{j-1}} \tag{3.58}$$

in which $\alpha_j = 0$ and $\beta_j = \infty$ for $j > m$ or $j < 0$. We define also a *Test Factor* Γ given by:

$$\Gamma(\theta_r, \phi, A, \lambda, \varepsilon) = \left(\frac{8}{u_x^2}\right)^2 F_o(\theta_r, \phi, A, \lambda, \varepsilon) \ . \tag{3.59}$$

Now if we substitute Equations 3.57 to 3.59 in Equation 3.53, we get:

$$\frac{dP}{d\Omega} = \Gamma(\theta_r, \phi, A, \lambda, \varepsilon)\left(\frac{\sin u_y L}{u_y L}\right)^2\left(\frac{d_o L}{2\,\omega_m}\right)^2\left[\sum_{j=0}^{m} \Psi_j \cos u_x \omega_j\right]^2 \tag{3.60}$$

or if we separate the effect of scratch valley and ridges, we get

$$\frac{dP}{d\Omega} = \Gamma(\theta_r, \phi, A, \lambda, \varepsilon)\left(\frac{\sin u_y L}{u_y L}\right)^2\left(\frac{d_o L}{2\,\omega_m}\right)^2 \cdot \left[\sum_{j=0}^{\ell} \Psi_j \cos u_x \omega_j + \sum_{j=\ell+1}^{m} \Psi_j \cos u_x \omega_j\right]^2 \ . \tag{3.61}$$

If all the parameters in the above equation are kept constant except for Ψ_j and ω_j, $j = 1, 2, ..., \ell\text{-}1$, then referring to Figure 3.2 on page 45, one sees that the changes in the diffracted light at the observation point are due to the changes in the shape of the scratch valley. This effect appears in the

first summation in Equation 3.61. We therefore define this summation as the scratch *valley shape factor* ξ_v given by:

$$\xi_v = \sum_{j=0}^{\ell} \Psi_j \cos u_x \omega_j \ . \tag{3.62}$$

Similarly, if all the parameters of Equation 3.61 are kept constant except for Ψ_j and ω_j, $j = \ell+1, \ldots, m-1$, then the changes observed in the diffracted light are due to the changes in the shape of ridges. These effects appear in the second summation in Equation 3.61. We define a scratch *ridge shape factor* ξ_r as:

$$\xi_r = \sum_{j=\ell+1}^{m} \Psi_j \cos u_x \omega_j \tag{3.63}$$

to represent the ridge shape.

Now suppose that the total width ($2\omega_m$) and depth (d_o) of the scratch are kept constant but the shape of the scratch valley and ridges can change. These changes will be reflected in the summation in Equation 3.60, which we define as the scratch *total shape factor* ξ_t:

$$\xi_t = \sum_{j=0}^{m} \Psi_j \cos u_x \omega_j \ . \tag{3.64}$$

Finally, substitution of the three shape factors in Equations 3.60 and 3.61 gives the following forms for the models:

$$\frac{dP}{d\Omega} = \Gamma(\theta_r, \phi, A, \lambda, \varepsilon)\left(\frac{\sin u_y L}{u_y L}\right)^2\left(\frac{d_o L}{2\omega_m}\right)^2 \xi_t^2 \tag{3.65}$$

and

$$\frac{dP}{d\Omega} = \Gamma(\theta_r, \phi, A, \lambda, \varepsilon)\left(\frac{\sin u_y L}{u_y L}\right)^2\left(\frac{d_o L}{2\omega_m}\right)^2 (\xi_v^2 + \xi_r^2 + 2\xi_v \xi_r) \ . \tag{3.66}$$

A simplified form of this model also can be obtained by assuming a V-shaped profile for the flaw. Let m=1 in Equation 3.60, then using Equations 3.58 and 3.59, we get:

$$\frac{dP}{d\Omega} = F_o(\theta_r, \phi, A, \lambda, \varepsilon)\left(\frac{\sin u_y L}{u_y L}\right)^2 L^2 d_o^2 (2\omega_1)^2 \left(\frac{\sin \frac{u_x \omega_1}{2}}{\frac{u_x \omega_1}{2}}\right)^4 . \tag{3.67}$$

The light scattering models in Equations 3.65 to 3.67 suggest that when light strikes a defective metal surface normally, the light diffracted into a small solid angle $d\Omega$ is dependent on the observation point, the area under light incidence, the light wavelength, and the dielectric permittivity of the metal. In addition, the diffracted light is a function of the length, width, depth, and shape of the flaw on the metal surface. The ridges as well as the valley of the flaw influence the scattered light. If the experiment setup and the metal under test remain fixed, changes observed in the

diffracted light are due to the changes in the characteristics of the flaw.

This theory, as did the theories in previous sections, gives the important result that the light intensity produced by a flaw is affected by various dimensions of the flaw simultaneously and that determination of the individual flaw dimensions from the scattered light intensity faces a uniqueness problem.

3.3 Comparison of the Models

The light-scattering models developed in this chapter were derived from three approximate theories under different conditions and have different implications. While the first model was obtained directly from the integral theorem of Helmholtz and Kirchhoff assuming a point light-source, the second theory used the Beckmann's scattering coefficient and the third approach evaluated the probability of the observation of diffracted light in a differential solid angle. All the three theories assumed that the observation point is far from the surface (compared to flaw dimensions or the light wavelength). In addition, the first model required flaw dimensions to be much larger than the light wavelength while the other two theories demanded that the radius of curvature of surface irregularities to be greater than the light wavelength, or the surface be weakly rough. The first model also assumed that the distance of the excitation point from the surface was much larger than flaw dimensions and approximated the Exponential Integral Function by its first order approximation. In the first two models, it was necessary to assume equal angles of light incidence and

observation to simplify the models while in the third model the angle of incidence was zero and not necessarily equal to the angle of observation. Furthermore, to make the first two models mathematically manageable, the flaw profile was assumed to be V-shaped; however, the third model was developed with the general piecewise linear profile and with the V-shaped profile.

Predictions of the three models about light scattering of the surface flaws are that the experimental factors as well as flaw depth, width, and shape influence the observed scattered light, and that the relationship between the observed light intensity and flaw parameters suffers from a uniqueness problem. Moreover, since these models resulted from different approximate theories, they reflect the influence of different factors with different degrees of emphasis. For example, the influence of flaw depth is seen in the first two models more strongly, while flaw width is better represented by the second and third models and the effect of flaw shape is better reflected in the third model.

Despite the usefulness of the present forms of the models in predicting the light scattering behaviour of the surface flaws, these models must be further simplified to allow their use in determination of flaw parameters from the observed light intensity uniquely. Such simplifications and examination of the simpler models are discussed in Chapter 5.

CHAPTER 4

THE EXPERIMENTAL INSPECTION SYSTEM

A certain experimental approach must be adopted to allow investigation about detection, characterization, or measurement of metal surface flaws and evaluation of the predictions of the approximate light scattering theories. The approach is determined mainly by the selection of the lighting method and the sensing scheme, as these aspects indirectly determine the system elements and the applicable techniques. For example, if a laser source and a diode array are chosen as opposed to other alternatives such as a tungsten filament lamp and a television camera or a fiber optic lighting and sensing device, then other system components and techniques are, to a certain degree, defined accordingly, and certain limitations and flexibilities result. When the experimental approach is specified, the system components must be chosen so that each one is individually optimized.

Sensing devices and their associated units generally require an initial correction and calibration. Nonuniformities associated with solid-state devices must be compensated for, and the device must be calibrated for appropriate interpretation of the data. Furthermore, these corrections and calibrations must be rechecked occasionally when the system has been operating for some time. The system should provide an easy means of checking the sensing devices.

This chapter gives the requirements for and the final choice of the experimental inspection system which is used in the remainder of this investigation. In addition, the conversion of the sensor data to decimal numbers is discussed, the sensor characteristics are studied, and the sensor calibration is explained. The listings and structure charts of the computer programs referred to in this chapter are given in Safabakhsh [1986].

4.1 Experimentation Approach and System Components

The investigation approach and the resulting inspection system must meet a number of requirements to be practically acceptable. The system must be efficiently implementable and operational on the production floor. As a result, it should not include a large number of optical components, nor should it need frequent adjustments. In addition, the speed of the system should be considerably higher than the speed of manual inspection, and its costs must be within reasonable limits. Finally, the system must be capable of extracting dimensional information about the flaw from the scattered light.

Considering the above requirements and the state-of-the-art of the field, it was concluded that the investigation should use a low-power laser source and a solid-state sensing device. A *Wedge/Ring Detector* (WRD-6400) manufactured by Recognition Systems, Inc., was selected because of its very low data rate, very high speed, low computer memory requirement, relatively low system costs, and immediate availability. Other elements of the system, as shown in Figure 4.1, consist of optical components for

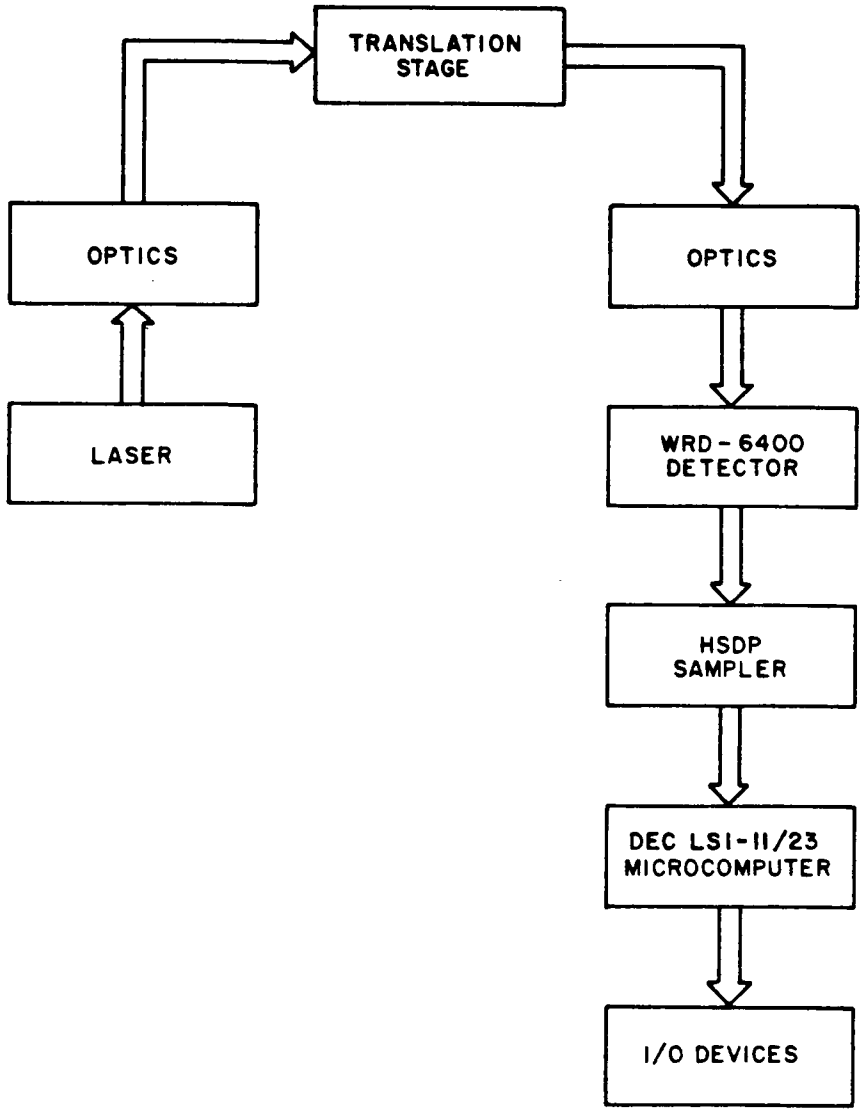

Figure 4.1. Components of the experimental inspection system.

directing the light, a translation stage for precision positioning of the part, a high speed sampler for data conversion, and a computer for decision making. More detailed descriptions of the system components are given in the remainder of this section.

4.1.1 The Laser Light Source

The light source is a Hughes 3021H-P Laser System radiating a light beam with the TEM_{00} output power of 1.0 mW. The light is linearly polarized and has a wavelength of 0.6328 μm. The $1/e^2$-diameter of the beam is 0.64 mm.

4.1.2 The Translation Stage

The translation stage is a linear 3-axis precision positioning device equipped with three micrometers. The three axes of the device presently are operated manually; they also can be operated under computer control if the necessary motors and interface circuits are provided.

4.1.3 The Optical Configuration

The choice of the optical configuration in the inspection system greatly influences the quality and usefulness of the acquired data. Care must be taken in selection of both the configuration and the components. A bad choice of a lens, for example, can degrade the system performance beyond compensation. Generally, the number of components in an optical system tends to grow very quickly. On the other hand, the more complex an optical system gets, the more degrading effects such as multiple reflections, refractions, and distortions could accumulate and degrade the overall

system performance. This is why optics experts try in their designs to get the job done using a minimum number of components. Another disadvantage of a complex optical system is that, even if it may be managable and easily operated in laboratories, a complex optical system does not suit the production environment.

Regarding the above aspects, a number of different optical configurations consisting of lenses, apertures, spatial filters, beam expanders, and beam splitters were considered and their performances were experimentally evaluated. Three of the more promising configurations are shown in Figure 4.2. Configurations (a) and (b) in Figure 4.2 were used in experiments reported in Safabakhsh [1983, 1984]. While the configuration (a) is simple, the large angle of light incidence is not desirable, especially for measurement purposes, as it will reduce the accuracy of the measurement. Optical configuration (b) in Figure 4.2 is not preferred for use on the plant floor nor is its performance drastically different from those of other two configurations. As a result, configuration (c) in Figure 4.2 is used in the experimental system. This configuration has the advantages that it is very simple and the light incidence and observation in it are close to normal.

4.1.4 The WRD-6400 Detector

The WRD-6400 Detector is composed of 64 light sensitive elements fabricated in a circle as shown in Figure 4.3. The first 32 elements have the form of concentric half rings and form half of the sensor surface. These elements are called *Rings*. The other 32 diodes are pie-shaped and

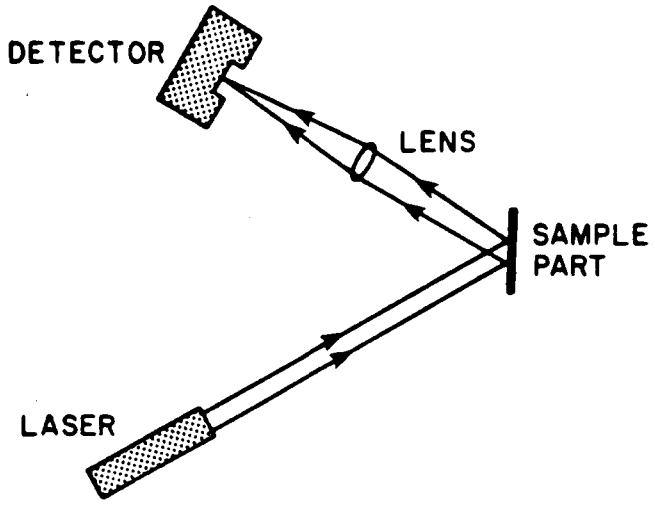

(a)

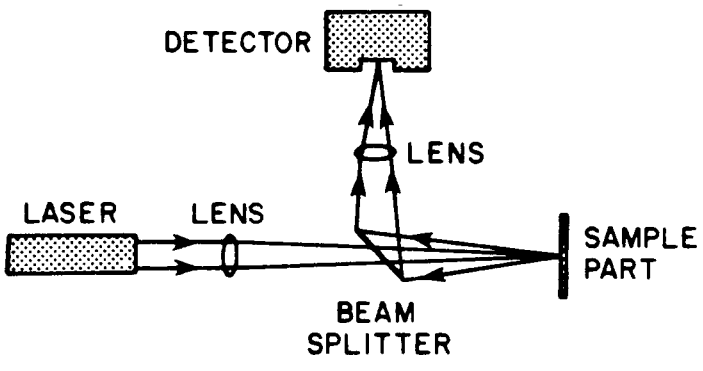

(b)

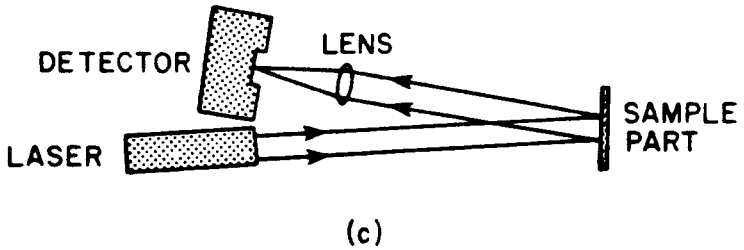

(c)

Figure 4.2. Three optical configurations for data acquisition.

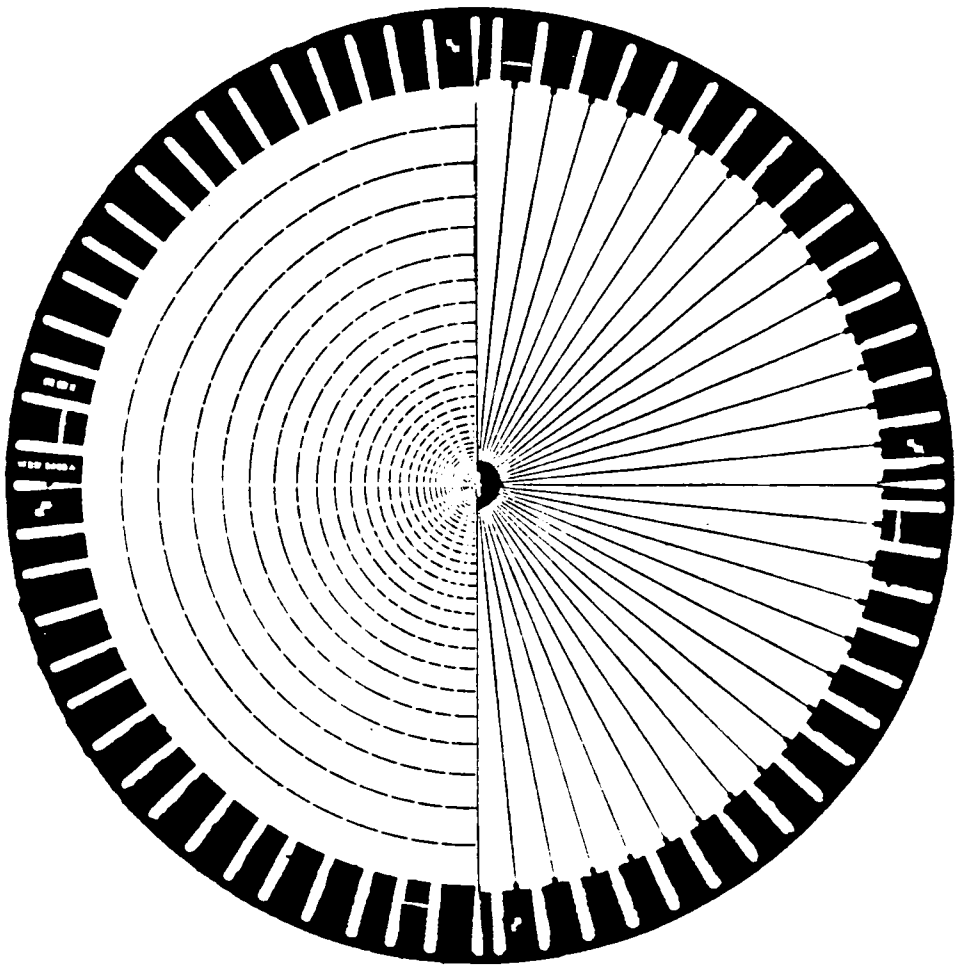

Figure 4.3. Surface of the WRD-6400 detector.

constitute the second half of the detector surface. These 32 diodes are known as *Wedges*. While the rings provide information about radial distribution of the detected light pattern, the wedges give information on the angular distribution of the light patterns.

When light strikes the surface of this detector, 64 signals are produced by the 64 diodes. This very low number of signals for processing constitutes a great advantage for this sensor as compared to a camera which produces tens of thousands of numbers per picture.

4.1.5 The High Speed Sampler

The outputs of the detector are weak analog signal. To make these signals usable for processing, a High Speed Diffraction Pattern Sampler (HSDPS) is supplied with the sensor to provide buffering, amplification, smapling, holding, and analog-to-digital conversion of the WRD signals. The 64 signals are digitized sequentially by a multiplexing scheme with a conversion cycle of 36 μs. In addition to these functions, the unit furnishes an operator control panel for manual checking and a computer interface for automatic operation of the unit.

4.1.6 The Microcomputer System

A DEC LSI-11/23 microcomputer with floating point arithmetic and memory management capabilities forms the brain of the system. The computer is equipped with 64K bytes of RAM, a dual disk drive unit with total capacity of 1M bytes, a 32-bit parallel I/O module for communication with the HSDPS, a video terminal, and a printer. An Extended RT-11

operating system runs the computer. A Fortran IV compiler and a Macro-Assembler are available for software development.

4.2 The HSDPS Output

The tasks of data acquisition and data conversion in the experimental system are performed under the control of the microcomputer. The sequence of the operations is:

1. Set the HSDPS to *tracking mode.*
2. Delay for tracking.
3. Check the Operator Panel switches. Declare error and exit if *sequential mode* is not selected.
4. Otherwise, disable tracking mode, enable *hold mode.*
5. Start the converter to convert a signal.
6. Delay for conversion.
7. Read the converted data into computer.
8. Repeat steps 5, 6, and 7 for all the signals.

An Assembly Language subroutine was developed to implement these bit-level operations. The subroutine is named WRD.

The outputs of the HSDPS are 11-bit binary numbers with a special format. Bits 0 to 7 represent the mantissa of the sampled data while bits 8 to 10 give its exponent. The mantissa is an 8-bit fractional binary number. The exponent is a 3-bit binary number which specifies the number of times the decimal point in mantissa should be moved to the right. This format

should be changed to a more appropriate form (e.g., decimal) before further processing. The following formula gives the HSDPS output in dcecimal:

$$\text{DATA} = (2^{\text{exponent}})(\text{mantissa})_{10} \tag{4.1}$$

An Assembly Language program called MANEXP was written to separate the mantissa and exponent of the converter output and to store them in the computer memory for the preprocessing operation of Equation (4.1) by a higher-level language.

4.3 The Sensor Characteristics and Calibration

Before investigating the inspection of metal surfaces by the experimental inspection system, it is necessary to study characteristics of the WRD-6400 detector and to become familiar with it. In addition, if any further preprocessing operation on the detector data is needed, it should be done at this stage.

4.3.1 The Dark-Current Test

The dark-current signals of the detector must be checked occasionally to assure its proper operation. Generally, it is desirable that these signals be very small and remain constant. The manufacturer of the WRD-6400 specifies a dark-current rating of $(0037)_8$ at the output of the HSDPS for each of the detector elements. This rating is equivalent to 0.121 decimal.

A dark-current test was performed with the aid of the Fortran program CHKWRD. The detector was completely darkened and a number

of data acquisitions were made under identical conditions. The resultant data showed dark signals in the range of 0.039 to 0.246 for different detector elements. This corresponds to a deviation of -67.7% to +103.3% from the nominal value. Moreover, signals produced by the inner rings were smaller and more consistent that those generated by the outer rings.

Considering the structure of the WRD-6400 detector, the production of unequal signals by the different detector elements is not far from expectation. The surfaces of the elements are not equal and it is only natural that the larger surfaces produce higher currents. In fact, the difference between some element areas is quite large. Ring 1, for example, has a surface of 0.02483 mm^2 while the surface area of ring 32 is 70 mm^2, 2817 times larger! Wedges (except for two of them) have equal areas which are larger than the area of ring 1 by a factor of 46.6. These differences in the areas of the detector elements must be considered in preprocessing of the data to eliminate their effects in the experiments.

While signals of various detector elements can be corrected for surface area differences, the signals of any single element cannot be controlled from fluctuations, even under identical test conditions. These fluctuations occur due to the noise present in the system and the environmental effects on the sensor. The result is that the sensor can not produce very consistent outputs--an undesirable characteristic for any detector. This effect is seen more clearly in the larger rings. Care must be taken to control the enviromental conditions very tightly to reduce their effect on the detector signals.

4.3.2 The Uniform Lighting Test

To observe the performance of the detector when the areas of the detector elements are taken into consideration, a second test with the inspection system was devised. The lighting and temperature of the test environment were controlled to minimize errors in the detector signals and the CHKWRD software was used to run the experiment. A low-power uniform variable-intensity light source was chosen to illuminate the detector elements uniformly. The intensity level was changed from zero to a high value (high enough to saturate the detector) and a large number of data sets were acquired. For each acquired data set, which we shall call *raw data*, a *corrected data* set was calculated. The corrected data for each element of the detector was obtained from:

$$\text{Corrected Data} = (\text{Raw Data}) \frac{1000}{\text{Element Surface Area}} \tag{4.2}$$

The corrected data for various lighting levels were studied and the following conclusions were drawn:

1. For a specific light intensity, the corrected wedge data are not dramatically different, while the corrected ring data still show very significant differences. The major problem appears at the two ends of the ring data where drastic nonlinearities show up. The behavior of the corrected data for middle rings, otherwise, is rather acceptable. The above observation suggests that correction of the data only for the effect of the surface areas does not produce the desired result and

further preprocessing of the data is necessary. Moreover, since the behaviour of the ring data is different from that of the wedge data, separate correction of the ring data and the wedge data is preferred.

2. At low light intensities, smaller rings do not respond to the changes in the light intensity. For example, rings 1 and 2 start to respond to the changes in light intensity at an intensity level which drives rings 27 to 32 to saturation.
3. As the light intensity is increased, more detector elements saturate. Rings 25 to 32 saturate before any wedge saturates. Saturation of the wedges occurs at about the same intensity level at which ring 24 saturates. Also, wedges come out of saturation at about the same intensity level at which ring 24 comes out of saturation.
4. At high intensity levels, larger rings must be watched for producing saturated data.

4.3.3 Calibrating the Detector

The Uniform Lighting Test indicated that normalizing raw data by the element surface areas does not correct the data adequately. Further preprocessing of the data is needed so that the detector response nonlinearities are made minimal. If the range of light intensity in a data acquisition is given, it is possible to specify which rings repsond to the intensities and to perform the preprocessing only for those rings. This eliminates the need for consideration of all the ring data in the correction procedure, it would correct the data only for the useful portion of the rings, and it would make correction of the data easier. However, requiring that

the intensity range be known for each data set necessitates the intervention of an operator and makes data correction cumbersome and inefficient. A better approach which does not require operator input in every data acquisition is desired.

In the Uniform Lighting Test the ring data for middle rings were fairly close. Based on this, a procedure was developed to attempt to level the ring intensity curve to its mid-range average and the wedge intensity curve to its overall average by finding a *calibration coefficient* for each ring or wedge. The procedure is interactive and consists of the following steps:

1. Using uniform lighting at a certain intensity, acquire raw data and store in $R_c(I, J)$ where I specifies the element number and J the data acquisition number.
2. Correct the raw data for area differences from:

$$C_c(I,J) = 1000\,\frac{R_c(I,J)}{A(I)} \qquad I = 1,\ldots,64 \tag{4.3}$$

   where A(I) gives the area of element I. Display the corrected data on the screen.
3. Get the lower bound (LB) and the upper bound (UB) of the range in which ring data are fairly constant from the operator.
4. Calculate the average of the ring data in the given range from:

$$M_R(J) = \frac{1}{UB-LB+1}\sum_{I=LB}^{UB} C_c(I,J) \tag{4.4}$$

Determine the *correcting coefficients* for rings so that each ring datum is converted to the above average value. That is:

$$COR(I,J) = \frac{M_R(J)}{C_c(I,J)} \qquad I = 1, \ldots, 32 \tag{4.5}$$

5. Compute the average of the wedge data from:

$$M_W(J) = \frac{1}{32} \sum_{I=33}^{64} C_c(I,J) \tag{4.6}$$

and determine the correcting coefficient for wedges so that each wedge datum is converted to the wedge data average. The coefficients are:

$$COR(I,J) = \frac{M_W(J)}{C_c(I,J)} \qquad I = 33, \ldots, 64 \tag{4.7}$$

6. Repeat steps 1 through 5 a number of times for various intensity levels (J = 1, ..., NT). Each cycle produces one set of correcting coefficients for the detector. Use the mean of these correcting coefficients to calibrate the corrected data. Calibration of the raw data can be performed by:

$$CALCO(I) = \frac{1000}{NT * A(I)} \sum_{J=1}^{NT} COR(I,J) \qquad I = 1,\ldots,64 \tag{4.8}$$

We call these coefficients the *calibration coefficients*. The calibration of new acquired data then is performed by:

$$\text{CALIBRATED DATA (I)} = \text{CALCO (I)} * \text{RAW DATA (I)} \tag{4.9}$$

Combining Equations 4.3 to 4.8, we get the coefficients as:

$$\text{CALCO(I)} = \begin{cases} \dfrac{1000}{NT * (UB - UL + 1)} \displaystyle\sum_{J=1}^{NT} \left[\frac{1}{R_c(I,J)} \sum_{I=LB}^{UB} \frac{R_c(I,J)}{A(I)} \right] & I = 1, \ldots, 32 \\ \dfrac{1000}{NT * 32} \displaystyle\sum_{J=1}^{NT} \left[\frac{1}{R_c(I,J)} \sum_{I=33}^{64} \frac{R_c(I,J)}{A(I)} \right] & I = 33, \ldots, 64 \end{cases} \tag{4.10}$$

This calibration procedure also was implemented in the CHKWRD program and several experiments were performed with it. High light intensities were avoided to eliminate the possible adverse effects of saturation. It was observed that using many sets of correcting coefficients (>20) reduces the effectiveness of the procedure. Among the experiments performed, one set of calibration coefficients derived from 10 cycles in the procedure showed the best performance and was chosen for future use. These coefficients are given in Table 4.1. Figures 4.4 to 4.7 show the raw and calibrated data for four different intensity levels. To make comparison easier, the calibrated data in these figures were multiplied by 10. Performance of these calibration coefficients is satisfactory and they are used to correct the detector data from this point on.

Table 4.1. Calibration coefficients for the 64 elements of the WRD-6400 detector.

I	CALCO(I)	I	CALCO(I)	I	CALCO(I)	I	CALCO(I)
1	1.877	17	0.324	33	0.511	49	0.591
2	1.780	18	0.257	34	0.505	50	0.578
3	1.532	19	0.198	35	0.498	51	0.571
4	1.304	20	0.153	36	0.505	52	0.574
5	1.483	21	0.121	37	0.504	53	0.583
6	1.433	22	0.092	38	0.511	54	0.583
7	1.218	23	0.070	39	0.520	55	0.585
8	1.173	24	0.051	40	0.526	56	0.585
9	1.156	25	0.039	41	0.532	57	0.596
10	1.020	26	0.028	42	0.532	58	0.594
11	0.902	27	0.022	43	0.536	59	0.595
12	0.764	28	0.016	44	0.558	60	0.588
13	0.677	29	0.014	45	0.569	61	0.583
14	0.565	30	0.011	46	0.614	62	0.584
15	0.485	31	0.008	47	0.564	63	0.577
16	0.390	32	0.007	48	0.589	64	0.595

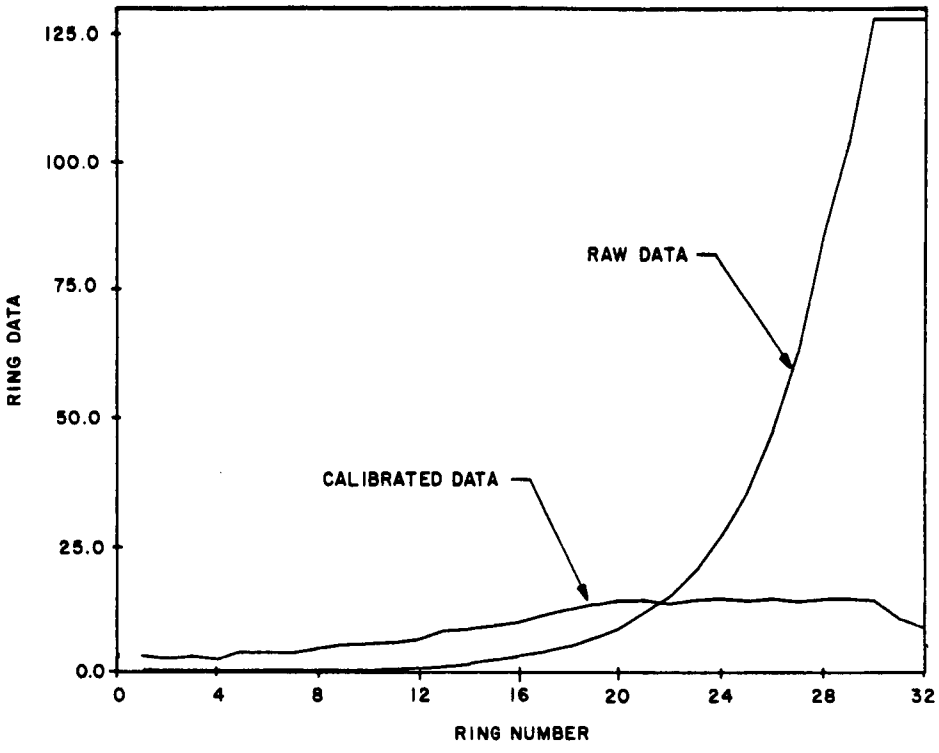

(a)

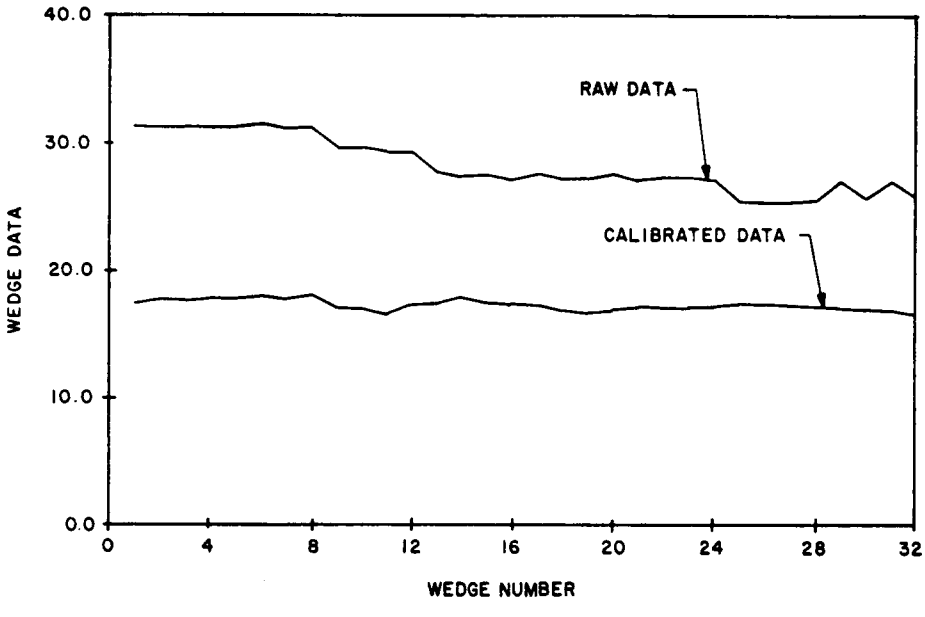

(b)

Figure 4.4. Sample raw and calibrated data for a high light intensity.

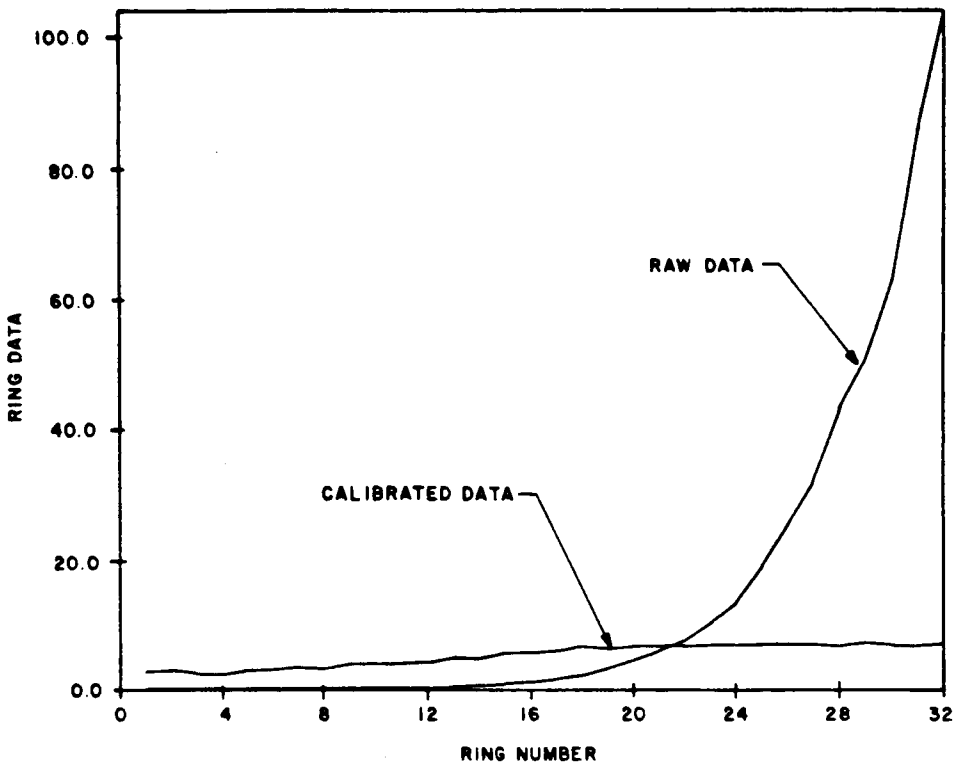

(a)

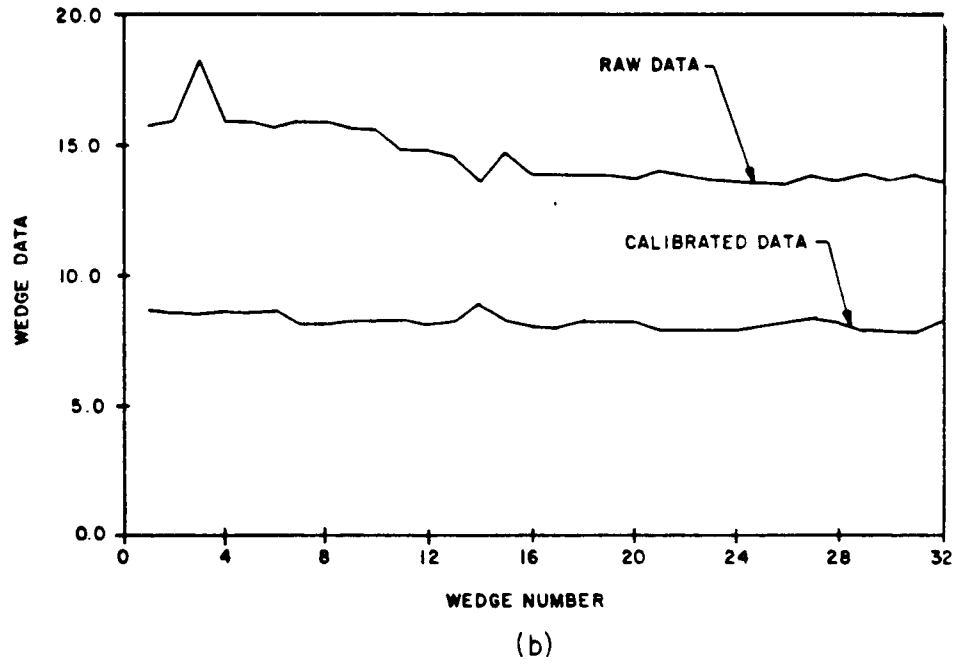

(b)

Figure 4.5. Sample raw and calibrated data for a medium-high light intensity.

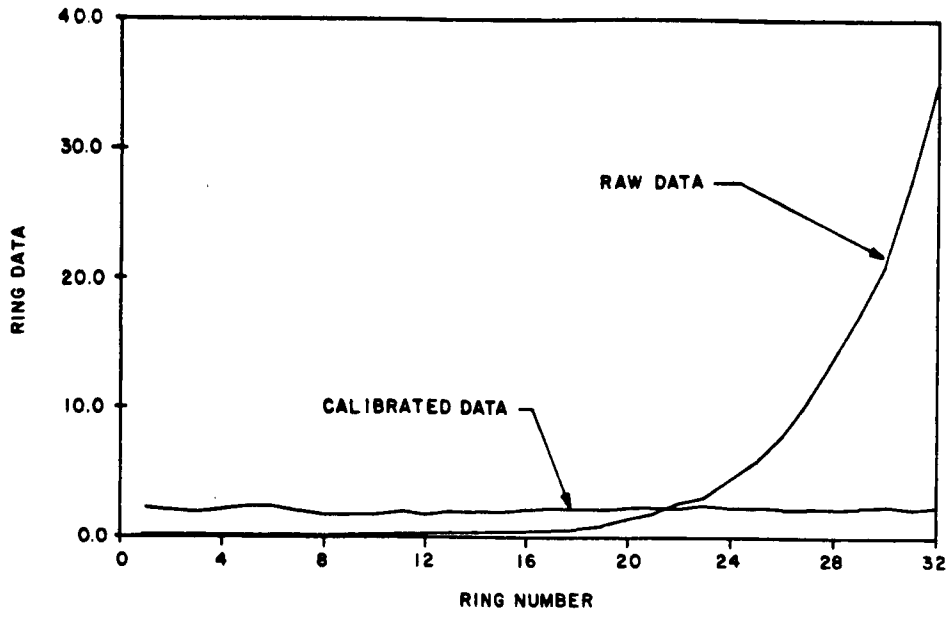

(a)

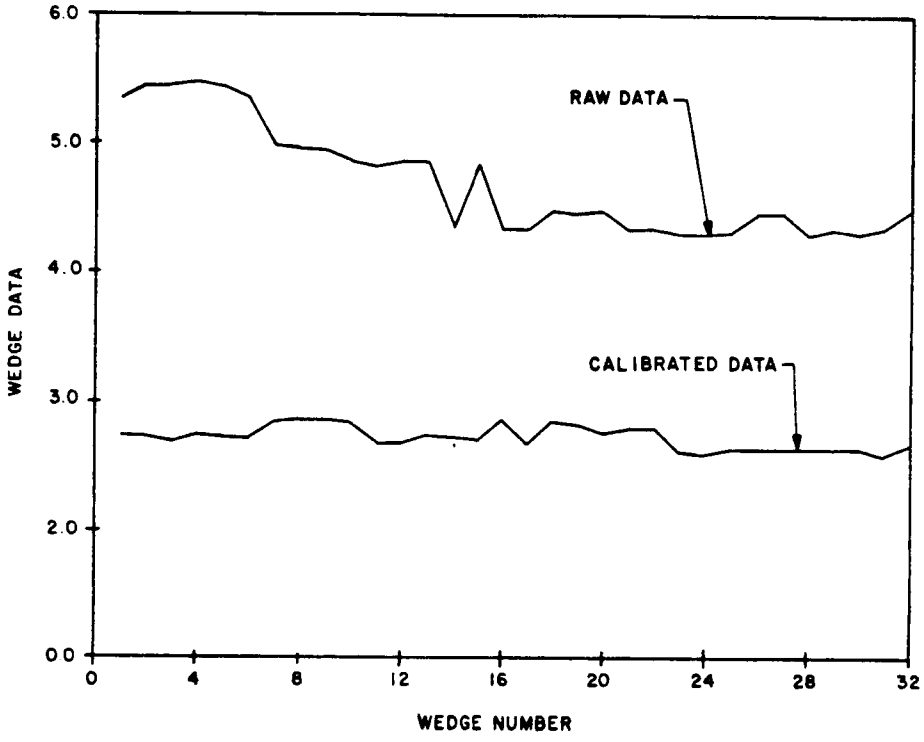

(b)

Figure 4.6. Sample raw and calibrated data for a medium-low light intensity.

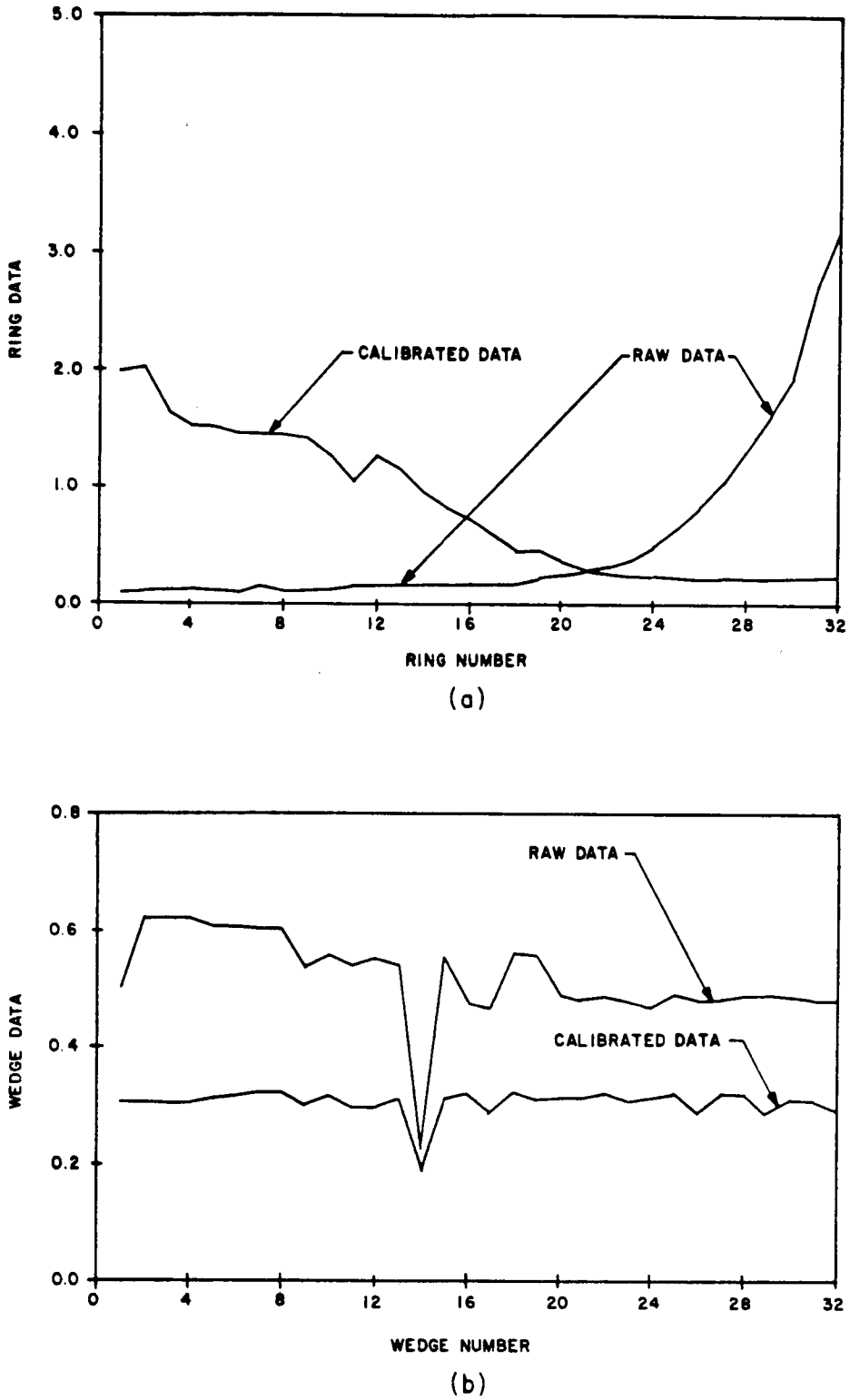

Figure 4.7. Sample raw and calibrated data for a low light intensity.

CHAPTER 5

INSPECTION OF MACHINED METAL SURFACES BY THE EXPERIMENTAL SYSTEM

Inspection requirements of various applications are different from one another. One application may require only the *detection* of flaws on metal surfaces while other applications may demand *detection and characterization* or *detection and measurement* of the flaws. The level of complexity of the task and the difficulty of its resolution increase drastically if characterization or measurement is demanded.

Detection of flaws is a macro-analysis of the surface quality, or a *macro-inspection*. A surface which could be quite large is examined for possible flaws and an *Accept/Reject* or *Go/No-Go* verdict is issued. The issuance of such a verdict requires the definition of what exactly constitutes acceptance and what exactly constitutes rejection of a surface.

Flaw characterization aims at providing *some* information about a detected flaw. The information describes the flaw relevant to features essential to the application. For example, the descriptions shallow; deep, wide; and shallow, narrow, long characterize the flaw when depth; depth and width; and depth, width, and length of the flaw, respectively, are critical to the application. An example of quantified flaw characterization would be categorizing flaws into various depth ranges such as:

$$\left\{\text{depth} < 5,\ \ 5 < \text{depth} < 10,\ \ \ 10 < \text{depth} < 15,\ \ \ \text{depth} > 15\right\} .$$

The most complete characterization of a flaw is a three-dimensional representation of the flaw. This is also the most difficult one to achieve.

Flaw measurement refers to precise quantified characterization of flaws. Here, the inspection system is expected to give numerical values for flaw dimensions. The dimensions of interest would generally be the length, the width at the widest point, and the depth at the deepest point. However, a more complete measurement of flaws requires a calibrated three-dimensional representation of the flaw. Quantitative description of flaw length or width is easier to achieve. A great difficulty enters the measurement task when measurement of depth is desired.

This chapter presents the results of flaw detection, characterization, and measurement by the Experimental Inspection System. Emphasis is put on depth inspection. The parts and flaws used in experiments are introduced first. Then, further preprocessing of the calibrated data to compensate for the environmental lighting and to extract relevant information or *features* for decision making from the data is discussed. Experiments for flaw detection, characterization, and measurement are described and conclusions are presented. All the computer programs referred to in this chapter are written in standard Fortran. Their structure charts and listings are given in Safabakhsh [1986].

5.1 Sample Parts for Experiments

Experiments for the inspection of machined surfaces require a set of sample parts with calibrated surface flaws. Such a sample set in this work

consists of a number of machined aluminum parts with flaws of various constant dimensions on their surfaces, several of which are shown in Figure 5.1. The surface roughnesses have peak-to-peak values of 0.00008" to 0.00016" (2.0 to 4.0 microns). A typical roughness profile obtained by an Alpha Step Profiler from one of the surfaces is shown in Figure 5.2. The flaws are all calibrated through the use of a Zeiss Light-section Microscope. The flaw depths range between 0.0001" and 0.0020" (2.5 to 51.0 microns) while the flaw widths range between 0.0015" and 0.0100" (38 to 254 microns). The shapes of the flaws are different, especially their ridges. Stylus-produced profiles of three of the flaws are illustrated in Figure 5.3.

The following important point concerning the above calibrated values and profiles must be remembered. The Light-section Microscope and the Stylus Profiler are both line-profiling devices, producing measurements of the flaw cross-section at one point along the flaw. The result is that the given calibrated values are valid at only one point along the flaw, and they do not necessarily represent accurate enough measurements at other points of the flaw. This can be particularly appreciated when the flaws are inspected under a microscope and the microscopic changes in flaw dimensions and shape are observed. Nevertheless, such calibrations are the best which can be obtained and were used in this work. Light-section Microscopes or similar devices which produce three-dimensional surface profiles to the author's knowledge do not exist.

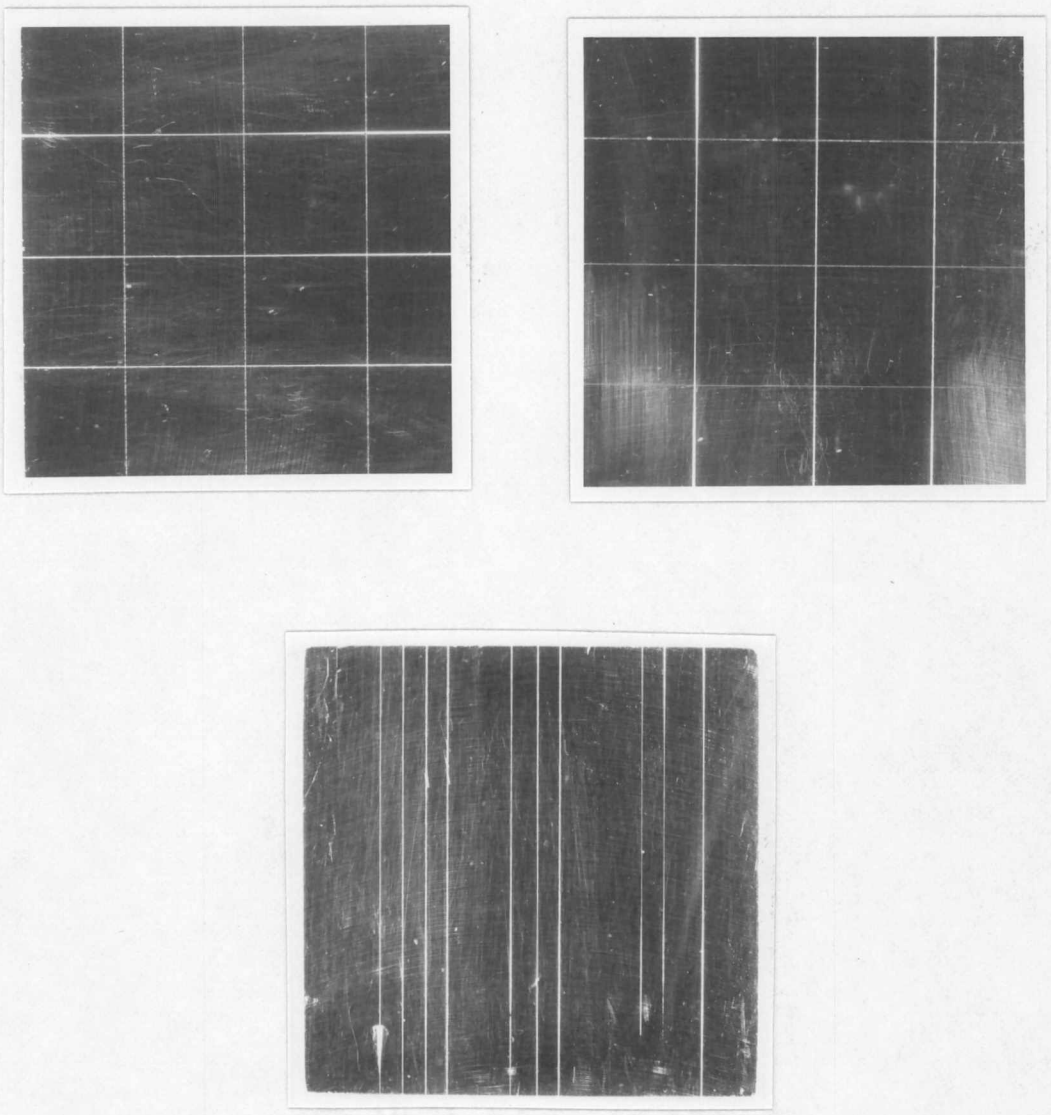

Figure 5.1. Photographs of several parts used in experiments.

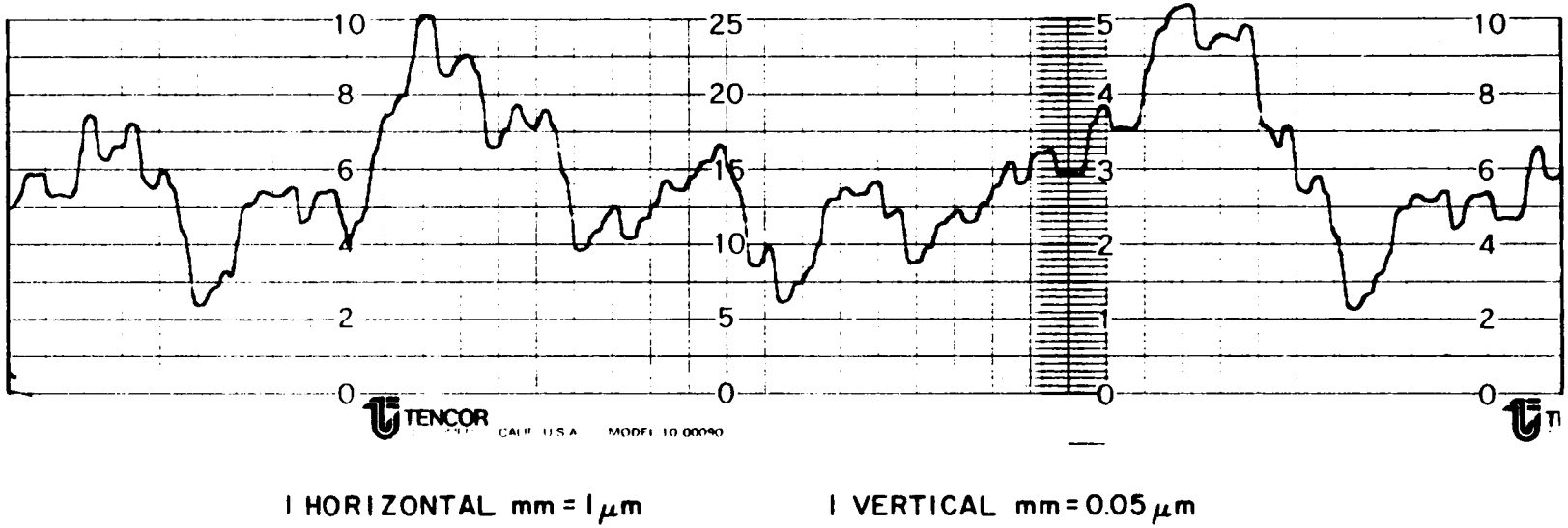

Figure 5.2. Typical profile of machined surfaces used in experiments.

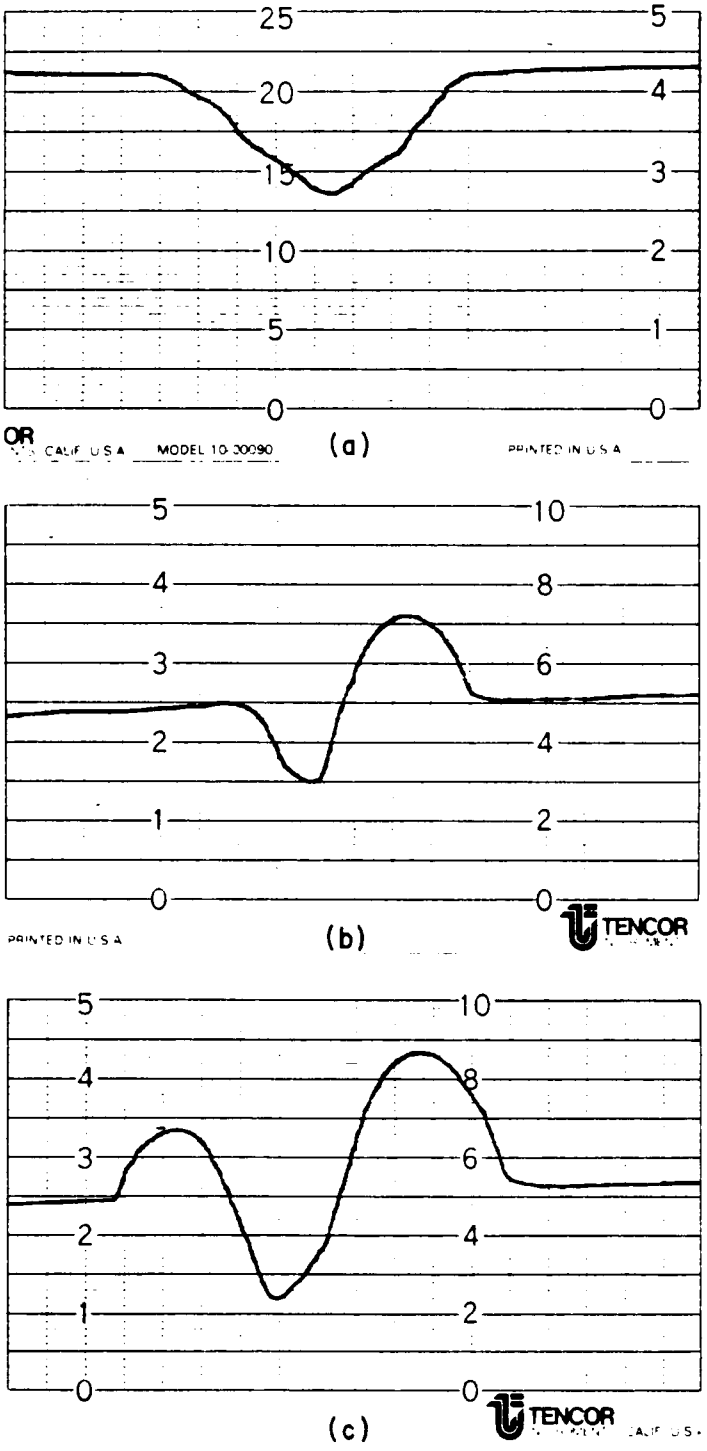

1 HORIZONTAL mm = 1 μm
1 VERTICAL mm = 2 μm

Figure 5.3. Three sample flaw profiles.

5.2 Feature Extraction and Correlations

The calibrated detector data consist of 64 numbers. Further preprocessing of this data is desired to serve two purposes: (1) to find some attribute of the data which carries a strong correlation with the flaw depth; and (2) to reduce the data volume to avoid mathematical operations on large vectors and matrices. This section introduces data reduction methods to achieve these goals.

5.2.1 Environmental Lighting Effects

Study of the Wedge/Ring detector revealed that the detector is very sensitive to environmental lighting and is saturated very easily, even by ordinary room illumination. This sensitivity and the varying nature of the environmental lighting reduce the accuracy of the data and influence the operation of the system adversely. This problem must be resolved before meaningful data are produced.

Two approaches to take care of the problem were examined. The first approach was based on separate sensing of the room lighting effects and subtracting them from the diffracted light. The second approach merely considered very tight control of the experiment environment lighting.

In the first approach two data sets were acquired under controlled room lighting -- one set from the point being inspected and another from a defect-free part of the surface. Subtraction of these data sets was expected to eliminate the effect of external lighting and to produce an environmental-lighting-debiased data set. Tests, however, indicated that

while this approach relaxed the need for very tight control of the room lighting, it introduced two new disadvantages -- the need for two data acquisitions per useful data set and introduciton of inconsistency into the behaviour of the data. While the need for two data acquisitions halves the speed of inspection, the subtraction of the assumed background lighting introduces errors into the data. This happens because the acquired background data not only carry the impact of the environmental lighting, but also are influenced by the metal surface characteristics of the defect-free area used in the data acquisition.

The second approach consisted of very tight control of the room lighting and allowing a small bias value to remain in the detector signals. Tests with this method indicated that even though small errors might exist in the detector signal, the data behave more consistently and are more meaningful. Therefore, it was concluded that subtraction of the background lighting is not preferred, but the room lighting must be controlled very tightly.

5.2.2 Feature Selection

A number of preliminary experiments were performed to investigate the sensitivity of the detected signal to the optical system adjustments and to gain a feel for which features carry high correlations with the flaw depth or width. Two different lenses were utilized in these experiments and the scattered light was focused on the detector surface to the circle of least confusion or to a slightly defocused diffraction pattern. These experiments conferred that focusing the scattered light to the circle of least confusion

produces more meaningful results and that the adjustments of the lens and the detector must be carefully watched during the experiments. The features found appropriate were included in the feature set of the following experiment for further investigation.

A large experiment was designed and executed to determine the appropriate features and their correlations with flaw depth and width. Fifteen scratches of various constant depths and widths were chosen; their calibrated dimensions are given in Table 5.1. For each scratch 20 data sets were acquired over a length of 50 microns of the flaw. This small length was chosen to reduce the effect of small changes in the dimensions of the flaw and the varying reflection coefficient of the surface.

After initial preprocessing of the data, 30 features were extracted from each data set. These features were:

1. sum of the wedge data (WS);
2. peak of the wedge data (WP);
3. sum of the ring data (RS);
4. total energy detected (TE);
5. total energy multiplied by peak of ring data (T*P);
6. total energy/peak of ring data (T/P);
7. peak of ring data/total eenrgy (P/T);
8. sum of ring data 5 to 32 (RS5);
9. sum of ring data 16 to 32 (RS16);
10. ratio of RS5 to RS16 (RSR);
11-15. the first five peaks of the ring data (RP1-RP5);

Table 5.1. Flaws used in correlation experiment.

FLAW NAME	DEPTH 1×10^{-4}" (microns)		WIDTH 1×10^{-4}" (microns)	
C8	1	(2.54)	20	(50.80)
C9	2	(5.08)	20	(50.80)
C1	4	(10.16)	15	(38.10)
B4	4	(10.16)	30	(76.20)
A7	5	(12.70)	30	(76.20)
C5	5	(12.70)	25	(63.50)
C2	7	(17.78)	20	(50.80)
C10	7	(17.78)	40	(101.60)
B5	9	(22.86)	40	(101.60)
C6	10	(25.40)	40	(101.60)
C3	12	(30.48)	30	(76.20)
4.5	12	(30.48)	35	(88.90)
C7	12	(30.48)	45	(114.30)
B6	13	(33.02)	45	(114.30)
C4	16	(40.64)	35	(88.90)

16-20. the ring number of the first five peaks of the ring data (RNP1-RNP5);

21-25. the first five minimums of the ring data (RM1-RM5); and

26-30. the ring number of the first five minimums of the ring dat (RNM1-RNM5).

At the completion of the feature-extraction step, every flaw possessed a set of 30 arrays each of which contained 20 samples of a specific feature for the flaw. Each feature array was then characterized by four of its statistical attributs -- the mean, the standard deviaiton, the lower limit, and the upper limit. Since the 20 data sets of each flaw could include a few data sets drastically different from the others (due to external interferences, operator errors, etc.), each feature array was truncated by dropping its three lowest and three highest values. Then the above statistical attributes were recalculated for the truncated arrays, the results of which are tabulated in Appendix D. In addition, correlation coefficients were computed for flaw depth or width and various features using the mean values of each feature for different flaws. The coefficients were found for the original and the truncated data from (Kirk [1978]):

$$r = \frac{n\sum_{i=1}^{n} X_i F_i - \sum_{i=1}^{n} X_i \sum_{i=1}^{n} F_i}{\left[n\sum_{i=1}^{n} X_i^2 - \left(\sum_{i=1}^{n} X_i\right)^2\right]^{1/2}\left[n\sum_{i=1}^{n} F_i^2 - \left(\sum_{i=1}^{n} F_i\right)^2\right]^{1/2}} \qquad (5.1)$$

where array F represents the mean values of a feature for different flaws and X contains the flaw depths for depth correlation and the flaw widths for width correlation. Appendix D contains corelation coefficients for flaw depth or width calculated from the truncated data for each of the 30 features.

All the collected data for the original and the truncated cases were studied extensively. It was concluded that using the truncated data was preferable since it produced equally good or better results than the original data. Groups of test scratches with the same width but different depths were considered and the mean, variability or dispersion, intercluster separation, width sensitivity, and depth and width correlations of their features were studied. Figure 5.4 illustrates the mean values versus flaw depth for four groups of scratches for the 30 features. For effective representation of the flaw depth, a feature must show a one-to-one relationship with the flaw depth and the rate of its changes with depth must be high. None of the 30 features possesses such attributes. The dependence of the features on the flaw width and shape and the lack of a unique relationship predicted by the light scattering theories discussed in Chapter 3 are clearly witnessed here. From theories, the light intensity maximums and minimums and their locations were expected to demonstrate a better correlation with the depth or width. However, the performances of these features are poor. This is caused partially by the fact that some minimums or maximums vanish in various data acquisitions and reduce the consistency of the light intensity distribution.

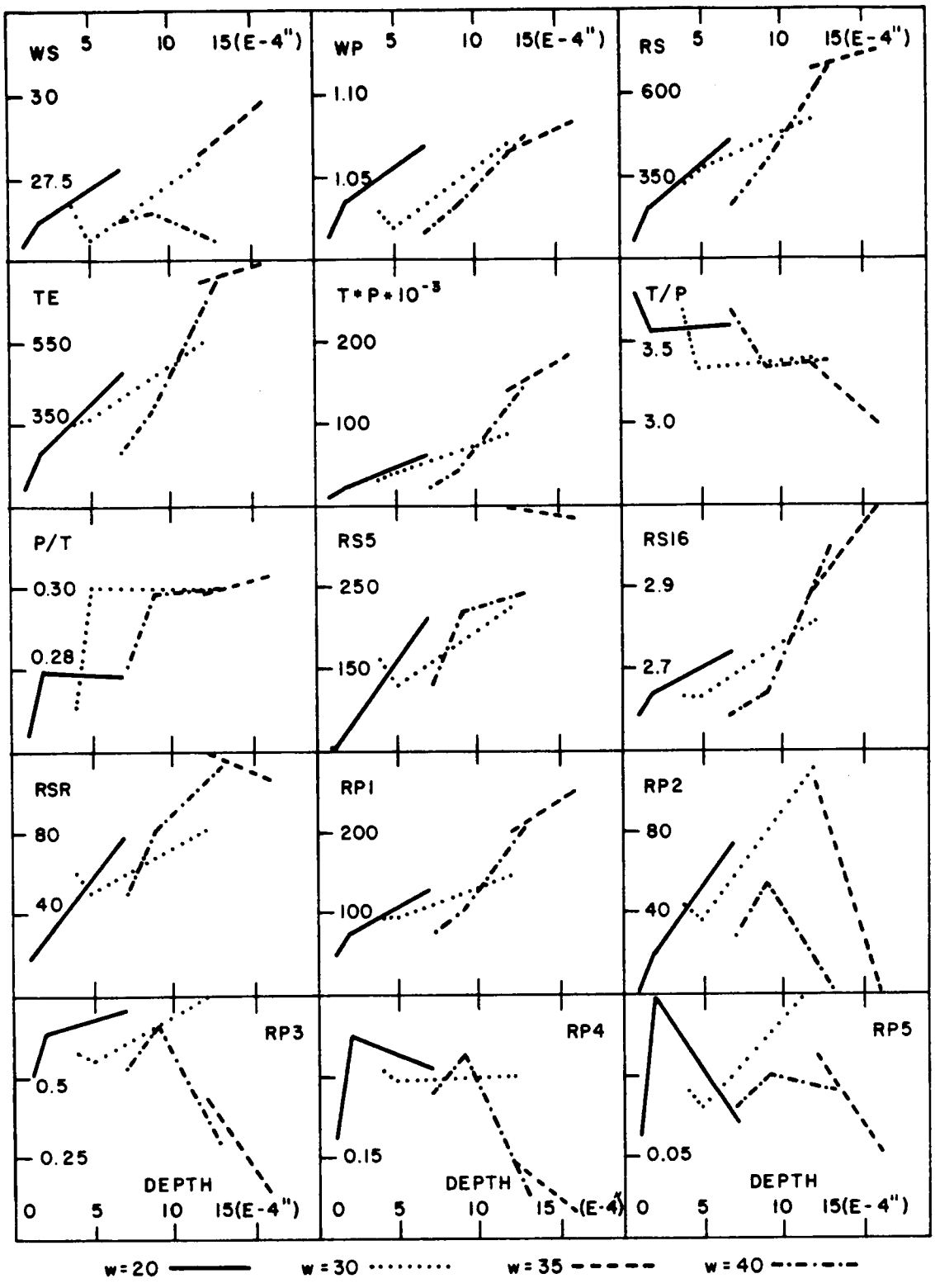

Figure 5.4. Mean values of flaw groups for various features.

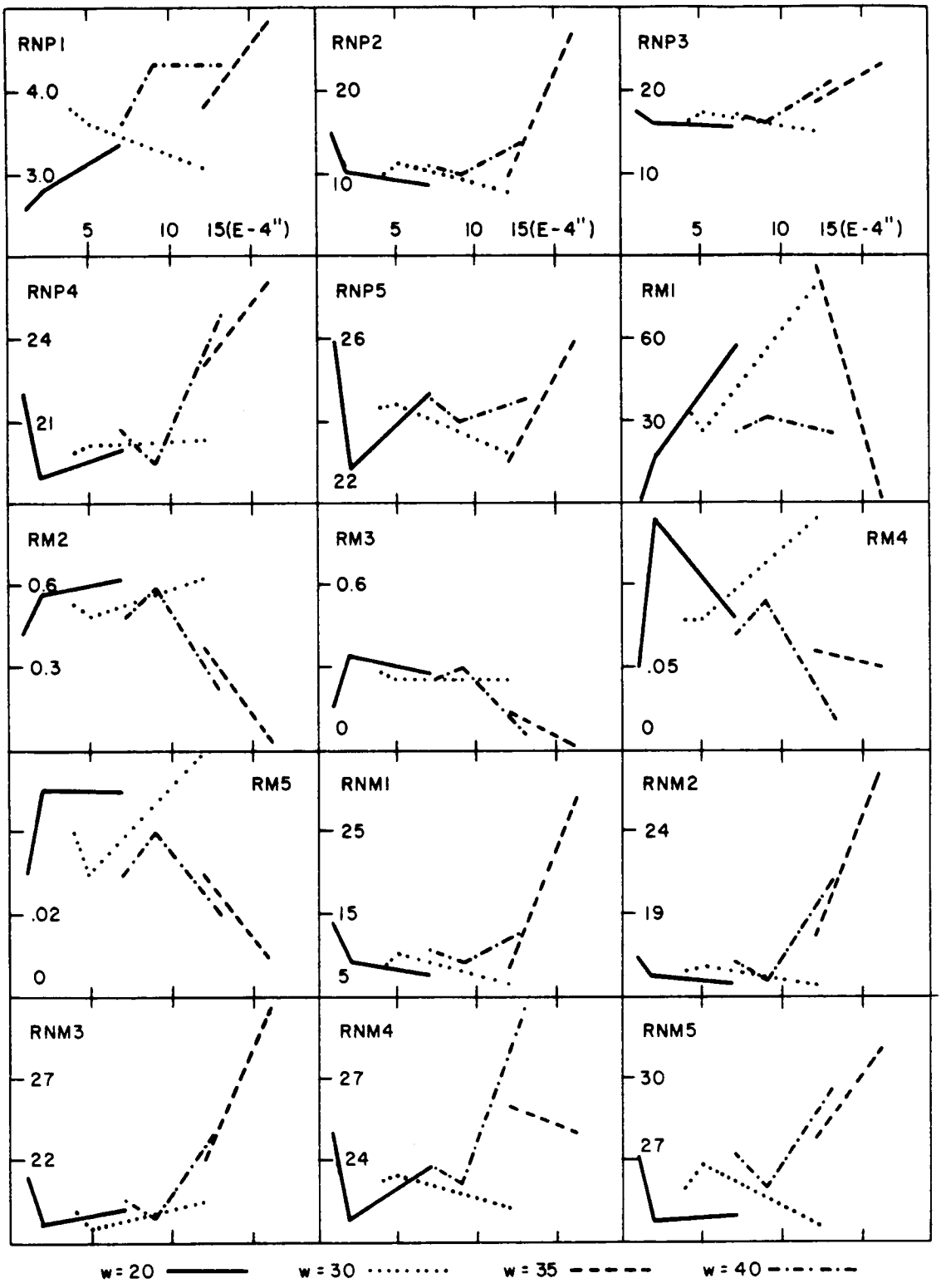

Figure 5.4. (continued)

Considering the mean values, we selected the following seven features for further investigation:

- total energy multiplied by peak of ring data (T*P);
- the first peak of the ring data (RP1);
- sum of the ring data (RS);
- total energy (TE);
- sum of ring data 16 to 32 (RS16);
- peak of the wedge data (WP); and
- ratio of sum of ring data 5 to 32 to sum of ring data 16 to 32 (RSR).

It is desirable that the selected features show a high clustering property. We evaluated this property of the seven features from the standard deviation tables (Tables D.4 and D.5 in Appendix D) where dispersion of the samples for each feature and each flaw is listed. The dispersion of the samples for the seven features increases in the following order:

$$WP \approx RS16,\ RSR,\ RP1,\ RS,\ TE,\ T*P\ .$$

In addition to the variability of samples in each sample cluster, the separation of different clusters from one another for each feature is also of great concern to us. We define a measure of intercluster separation as follows. Consider a cluster i and a feature j. Denote the upper limit of cluster (i-1) for the feature by $U_{(i-1)j}$ and the lower limit of the cluster $(i+1)$ by $L_{(i+1)j}$. Also, denote the mean and standartd deviation of the samples for class i and feature j by M_{ij} and S_{ij}, respectively. The definitions

$$\delta_{L_{ij}} = \frac{M_{ij} - U_{(i-1)j}}{S_{ij}} \tag{5.2}$$

and

$$\delta_{U_{ij}} = \frac{L_{(i+1)j} - M_{ij}}{S_{ij}} \tag{5.3}$$

give the relative separation of cluster i from clusters (i-1) and (i+1), respectively. We now define a *cluster separation coefficient* for feature j as:

$$\eta_j = \sum_{\text{FLAWS}} \min \{\delta_{L_{ij}}, \delta_{U_{ij}}\} . \tag{5.4}$$

The larger the η_j, the more desirable the feature j is. Coefficient η_j was computed for the seven features of concern to us from the tables of Appendix D. The results, given in Table 5.2, specify T*P, TE, RS, RP1, RSR, RS16, and WP as the most desirable to least desirable features. In fact, the negative η_j's of the last three features suggest interference of sample clusters for these features.

As another method of evaluating the selected features we considered the depth-feature and the width-feature correlations. Table 5.3 illustrates the results. For all the seven features the depth correlation is higher than the width correlation by at least 20%. The depth correlations, however, are

Table 5.2. Cluster separation coefficients for the selected features.

FEATURE j	WP	RS	TE	T*P	RS16	RSR	RP1
η_j	-4.67	6.04	6.22	7.62	-3.51	-2.81	3.41

Table 5.3. Depth and width correlations for the selected features.

	WP	RS	TE	T*P	RS16	RSR	RP1
DEPTH	0.832	0.885	0.885	0.869	0.839	0.886	0.886
WIDTH	0.417	0.603	0.603	0.630	0.534	0.651	0.617

not drastically different for different features and decrease in the following order: RSR ≈ RP1, RS ≈ TE, T*P, RS16, and WP.

Another aspect of features desirable for depth inspection is insensitivity of the feature to the flaw width. Groups of test scratches with the same depth but different widths were chosen and the mean values for each group for various features were studied. The results indicate that the features' sensitivity to flaw width increases in the order of T*P, TE ≈ RS, RP1, RSR, RS16 and WP.

Considering the above evaluations of the features we conclude that WP and RS16 should be eliminated from the selected features because of sample cluster interferences and high width sensitivity effects. Furthermore, the performances of RS and TE are quite similar and it is not necessary to include both of them in the selected features. Consequently, we finalize the features to RS, T*P, RSR, and RP1. Performance of these features will be further evaluated in the experiments of the next section.

5.3 Flaw Detection

In each application, the basis for flaw detection comes from the specifications adopted for acceptable and unacceptable flaws in that application. These specifications amount to thresholds specified for each flaw variable of interest. The decision-making for flaw detection, then, becomes the process of determining whether or not any of the given thresholds are exceeded. Such thresholds for the experiments in this work consist of only a depth threshold of 0.0010" (25.4 microns). Any flaw of

0.0010" or lesser depth is acceptable and classified as GO, while flaws deeper than 0.0010" are unacceptable and classified as NO-GO.

Two methods of decision-making based on cluster analysis were selected for the experimentation -- the *minimum distance classification rule* and the *Bayes classification rule* (Tou and Gonzalez [1974]). The minimum distance classifier uses the proximity of patterns in Euclidean space, assigning each pattern to the cluster of patterns closest to it. The Bayes classifier, on the other hand, is based on minimization of average loss in a zero-sum game and classifies samples in a statistically optimal sense. Both these methods require a *training phase* in which the classifier *learns* about the classes it is to recognize. This training is performed by showing typical samples of classes to the classifier. Programs TASISM and TASISB implement these two methods in our Experimental Inspection System.

Results of some of initial detection experiments are reported in Safabakhsh [1983, 1984]. The following experiments introduce the flaw detection capability of the present configuration of the Experimental Inspection System. The four scratches named B4, C10, B6, and C4 in Table 5.1 on page 97 were used for training the classifiers. Each scratch provided 15 samples for a training set of 60 patterns. The samples of the first two flaws constituted the patterns for the GO class, while the second two scratches provided samples for the NO-GO class. After the training was complete, these same four scratches as well as three other scratches were used to test the performance of the classifiers. Each scratch was tested over

a small portion of its length 25 times. The experiment was repeated for the two classifiers and each of the four features RS, RP1, T*P, and RSR.

The results of the experiments are presented in Tables 5.4 to 5.7. Although the two classifiers show similar performances for detection of the scratches in the training set, the overall performance of the minimum distance classifier is superior to that of the Bayes classifier. This is true despite the fact that the results obtained by the Bayes method should be optimal. The reason for this contradiction is that the Bayes decision function assumes Gaussian density functions for the samples, while the samples in the experiments do not show such a property. This has reduced the effectiveness of the classification approach.

As witnessed by Tables 5.4 and 5.6, the sum of ring data (RS) shows the best performance among the four selected features followed by total energy multiplied by peak of ring data ($T * P$) and the peak of ring data (RP1). The ratio of the sum of ring data 5-32 to sum of ring data 16-32 (RSR) demonstrates an inferior performance and may be dropped. Dependence of the features on the flaw width, in addition to flaw depth, reduces the accuracy of flaw detection by the system. This can be observed in the experiments by referring to Table 5.6. Considerable error enters the detection of C3 because, while its depth is only slightly higher than the threshold, its width is equal to the smallest width of the scratches used in the training phase. This small width of C3 has pulled the flaw from the NO-GO class to the GO class about 50% of the time. While a NO-GO test flaw significantly narrower than the training flaws may be wrongly classified as

Table 5.4. Correct detection of flaws used in training by the the minimum distance classifier.

FEATURE	FLAW CLASS, NAME, DEPTH, AND WIDTH (10^{-4}")				AVERAGE
	GO CLASS		NO-GO CLASS		
	B4 D=4 W=30	C10 D=7 W=40	B6 D=13 W=45	C4 D=16 W=35	
RS	100%	100%	100%	100%	100%
RP1	100%	100%	92%	96%	97%
T*P	100%	100%	96%	100%	99%
RSR	60%	100%	76%	16%	63%

Table 5.5. Correct detection of flaws used in training by the Bayes classifier.

FEATURE	FLAW CLASS, NAME, DEPTH, AND WIDTH (10^{-4}")				AVERAGE
	GO CLASS		NO-GO CLASS		
	B4 D=4 W=30	C10 D=7 W=40	B6 D=13 W=45	C4 D=16 W=35	
RS	100%	100%	100%	100%	100%
RP1	100%	100%	100%	80%	95%
T*P	100%	100%	100%	96%	99%
RSR	32%	100%	84%	56%	68%

Table 5.6. Correct detection of test flaws by the minimum distance classifier.

FEATURE	FLAW CLASS, NAME, DEPTH, AND WIDTH (10^{-4}")		
	GO CLASS	NO-GO CLASS	
	B5 D=9 W=40	C7 D=12 W=45	C3 D=12 W=30
RS	100%	100%	64%
RP1	100%	100%	40%
T*P	88%	100%	56%
RSR	58%	16%	0%

Table 5.7. Correct detection of test flaws by the Bayes classifier.

FEATURE	FLAW CLASS, NAME, DEPTH, AND WIDTH (10^{-4}")		
	GO CLASS	NO-GO CLASS	
	B5 D=9 W=40	C7 D=12 W=45	C3 D=12 W=30
RS	8%	56%	16%
RP1	20%	28%	0%
T*P	8%	20%	0%
RSR	64%	36%	0%

a GO flaw, a GO flaw considerably wider than the training flaws may also be classified wrongly as a NO-GO flaw. Such problems continue to exist until a depth-only-dependent feature can be found -- a necessity which may not be realizable at all!

We conclude this section with the following guidelines for flaw detection:

1. Surfaces of differnt materials or of different quality must be inspected by separate inspection criteria. Mixing such surfaces in the same training or testing set undoubtedly degrades the performance of the flaw detection system.
2. It is highly desirable that for every specific surface type or quality, the detection system develops and utilizes various inspection criteria correspondng to various small flaw width ranges.
3. A well-chosen training set can have an indispensable impact on the system performance. The training flaws must be selected so that their depth distribution about the threshold is well balanced. As an example, the 100% correct detection obtained from the training flaws

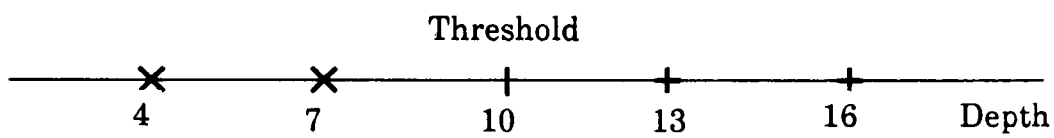

is reduced to 88% correct classification with the training flaws

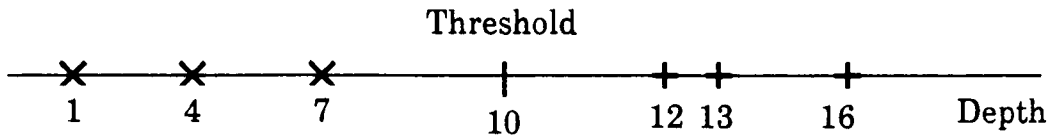

5.4 Flaw Characterization

Frequently, when the depth of a flaw is found to be greater than a given threshold, it is desirable to know the depth range of the flaw. Knowing merely that the flaw is deeper than the threhold is not always sufficient for making a decision about the part. Is the flaw depth greater than the threshold by 1, 10, or 100? Flaw characterization attempts to provide additional information about the flaw and to supply answers to such questions.

5.4.1 Classification of Flaws

To determine the depth range of a detected flaw, the two-class decision-making problem of the previous section must be extended to a multi-class case. We consider a four-class problem with the classes defined based on flaw depth as:

CLASS 1: Flaw Depth $\leq$ 0.00055"

CLASS 2: 0.00055" $<$ Flaw Depth $\leq$ 0.00100"

CLASS 3: 0.00100" $<$ Flaw Depth $\leq$ 0.00145"

CLASS 4: 0.00145" $<$ Flaw Depth

A number of experiments were performed using the training flaws B4, C10, B6, and C4 utilized in the previous section. The results of the following

experiment are typical of the Experimental Inspection System performance. A set of 100 samples was used to train a minimum distance classifier for the four classes. The performance of the classifier was evaluated through 100 tests of the training patterns and 100 tests using a testing set. The three single features RS, RP1, and T*P were considered for performing classification. Table 5.8 presents the results of the experiment. The highest correct classification rate achieved through these features was, on an average basis, 84% for the training set using RS, and 53% for the testing patterns using RS or T*P.

The above results could be improved if multiple features were used in the experiment. This was investigated by selecting two feature sets (RS RP1) and (RS RP1 T*P) and performing the classification with the same training and testing sets used with single features. The percentages of correct classification for these feature sets are also included in Table 5.8. Unfortunately, no improvement over the performance of the single features is observed. Other experiments reported in Safabakhsh [1983, 1984] also show similar correct classification rates. Under the present experimentaiton approach, this rate seems in general to stay between 50% and 75%.

The degradation in the system performance as compared to the 100% correct detection rate is produced by several factors. The major factors are the flaw ridges and widths, while other factors such as different surface qualities of parts A and B and small sizes of the selected depth ranges are also influential. Almost all the classification errors occur between classes 1

Table 5.8. Correct classification of training and testing patterns into four ranges of flaw depth.

TESTS	FEATURE(S)				
	RS	RP1	T*P	(RS RP1)	(RS RP1 T*P)
TRAINING SET					
Class 1	96%	72%	64%	96%	64%
Class 2	92%	44%	60%	96%	64%
Class 3	60%	48%	56%	56%	56%
Class 4	88%	68%	68%	88%	68%
Average	**84%**	**58%**	**62%**	**84%**	**63%**
TESTING SET					
Class 1	12%	52%	28%	8%	28%
Class 2	92%	44%	72%	92%	72%
Class 3	44%	32%	44%	48%	48%
Class 4	64%	76%	68%	68%	68%
Average	**53%**	**51%**	**53%**	**54%**	**54%**

and 2 or classes 3 and 4. Examination of the profiles of the four flaws by a Stylus Profiler indicated C10 as a *clean* flaw without ridges while B4 has a wide ridge. Also, B6 has a width larger than that of C4 and its ridges are larger and wider than those of C4. The impact of these shape and width differences cannot be ignored.

In order to further show the effect of flaw width on the depth range determination, we selected several special flaws and classified them by the trained classifier. Each selected flaw had a depth close to one of threshold values but a width much larger or much smaller than the width of the corresponding training flaw. The dimensions of these flaws as well as the results of the classification are given in Table 5.9. The impact of the flaw width on the classification is obviously tremendous!

Categorization of flaws can also be performed in several stages by a *tree-classifier* as discussed by Swain and Hauska [1977]. The *coincident spectral plot* for the four classes and the three features RS, RP1 and T*P is given in Figure 5.5. Classes 1 and 2 are shown to be easily separable from clases 3 and 4 (witnessed also by the 100% correct detection in the previous section). However, classes 1 and 2 or 3 and 4 are not as easily separable. The feature RS allows the best separation for classes 1 and 2 and the feature T*P seems to permit the best separation for classes 3 and 4. As a result, we adopt a decision tree as shown in Figure 5.6. The feature used for decision-making at each node of the tree is also shown on the diagram. This decision tree was implemented to classify the testing patterns used in the previous experiment. The results are 12%, 92%, 40%, and 68% correct

Table 5.9. Correct classification of a set of flaws chosen to show the degrading effect of flaw width.

THRESHOLDS & TRAINING WIDTHS (10^{-4}")	FLAW NAME & DIMENSIONS (10^{-4}")	FEATURE(S)		
		RS	T*P	(RS TP1)
THRESHOLD1 = 5.5				
	C2 D = 7 W = 20	0%	0%	0%
Training Width = 40				
	A10 D = 9 W = 50	0%	0%	0%
THRESHOLD2 = 10				
	C3 D = 12 W = 30	0%	16%	0%
Training Width = 45				
	A11 D = 14 W = 80	0%	0%	8%
THRESHOLD3 = 14.5				

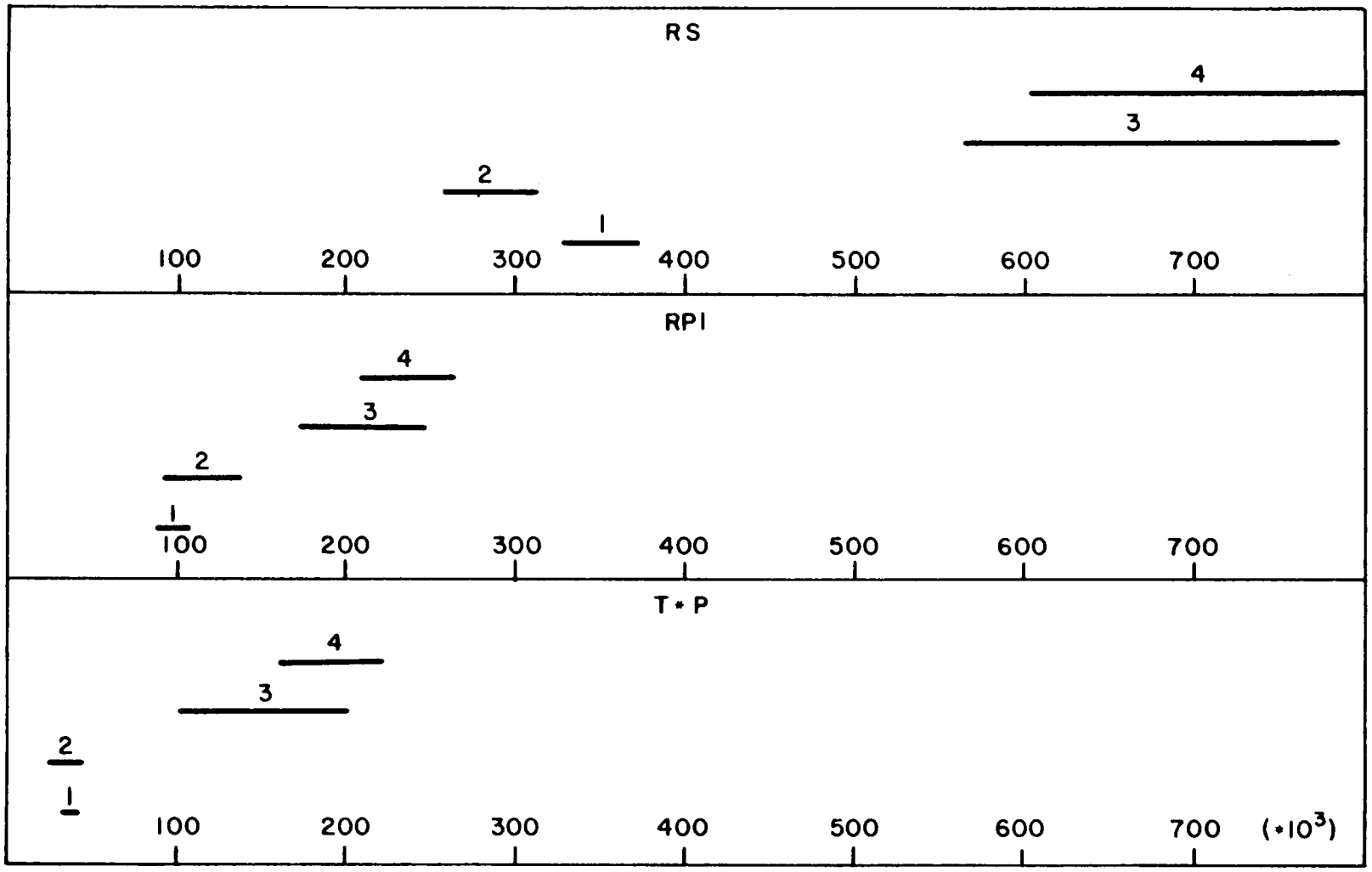

Figure 5.5. The Coincident Spectral Plot for the three features RS, RP1, and T*P.

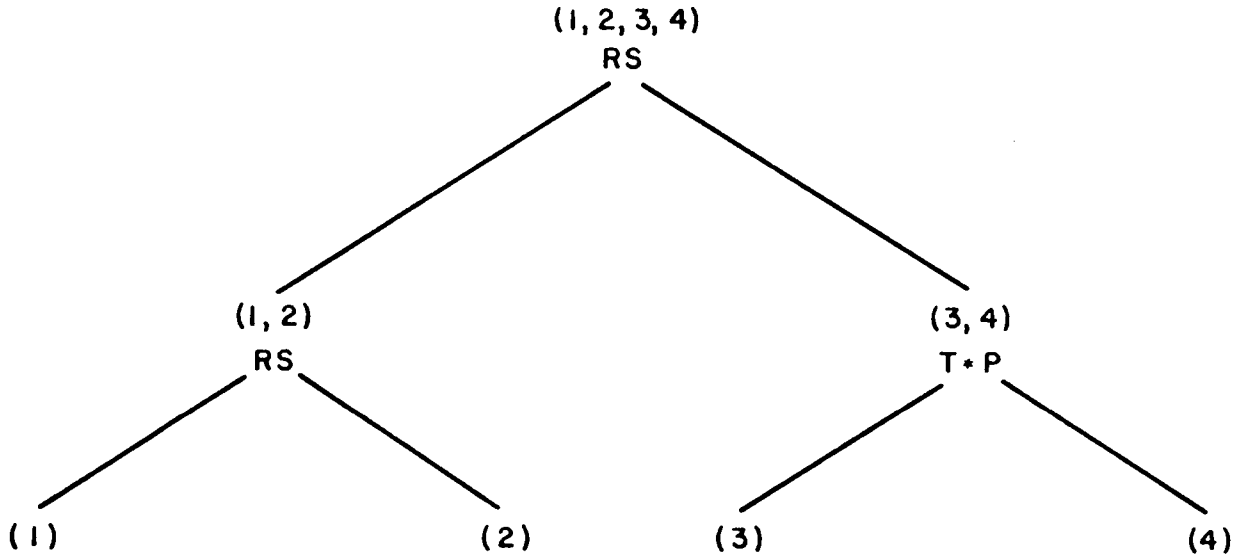

Figure 5.6. The decision tree for the four-class tree classifier.

classification for classes 1 to 4, respectively. These rates produce an average correct classification of 53%.

The tree-classifier does not boost the correct classification rate because of the inability of the features to adequately separate the four classes. If features which would distinguish between classes 1 and 2 or 3 and 4 were known, then the tree classifier would improve the results.

5.4.2 Flaw Shape Construction

Our major emphasis in this work has been on the inspection of flaws at their deepest point which we referred to as flaw depth. The scratches used in experiments were especially made so that, at least at the macro level, each one had constant depth and width. As a result, any point along the scratch was equally good for the acquisition of a data set for inspection. Actual scratches, on the other hand, have varying depths and widths along the scratch. If the deepest point of such a scratch is to be inspected by *a single* data acquisition, how can this point of the flaw be located? Even in a semi-automated system, the best chance of locating the deepest point is only as good as a human guess. Inspection based on a single data acquisition faces this inherent deficiency which no fully- or simi-automated approach can overcome. Further information extraction is necessary. Construction of flaw shape is one way of finding the deepest point in a flaw.

To construct the flaw shape, we consider the piecewise linear approximation introduced in Figure 3.2, on page 45. This profile can be specified completely at a point n along the flaw in terms of the d_i's and ω_i's at that point (d_{in}'s and ω_{in}'s) by a model B_{mn} as:

$$B_{mn} = (d_{on}\ d_{1n} \cdots d_{(m-1)n}\ \omega_{1n}\ \omega_{2n} \cdots \omega_{(m-1)n}) \tag{5.5}$$

Now if B_{mn}'s for a number of consecutive points along the entire length of the scratch are combined, a description of the shape of the scratch will result. Assume that B_{mn}'s at q points along the scratch are known and each point k is separated from point k+1 by ΔL_k, then one possible representation of the scratch is:

$$G_{mq} = \begin{bmatrix} 0 & d_{01} & d_{11} & \cdots & d_{(m-1)1} & \omega_{11} & \omega_{21} & \cdots & \omega_{(m-1)1} \\ \Delta L_1 & d_{02} & d_{12} & \cdots & d_{(m-1)2} & \omega_{12} & \omega_{22} & \cdots & \omega_{(m-1)2} \\ \cdot & & & & & & & & \cdot \\ \cdot & & & & & & & & \cdot \\ \cdot & & & & & & & & \cdot \\ \Delta L_{q-2} & d_{0(q-1)} & d_{1(q-1)} & \cdots & d_{(m-1)(q-1)} & \omega_{1(q-1)} & \omega_{2(q-1)} & \cdots & \omega_{(m-1)(q-1)} \\ \Delta L_{q-1} & d_{0q} & d_{1q} & \cdots & d_{(m-1)q} & \omega_{1q} & \omega_{2q} & \cdots & \omega_{(m-1)q} \end{bmatrix} \tag{5.6}$$

The two models B_{mn} and G_{mq} represent the scratch cross-section and shape effectively. However, direct measurement of the parameters of these models is not possible. To make the idea more practical, we introduce the following modifications in the models. First, we perform the model acquisition experiment with equal longitudinal increments ΔL along the scratch and equal transversal increments $\Delta\omega$ across the scratch. With the knowledge of ΔL and $\Delta\omega$, the model does not need to include ω_{in}'s nor ΔL_i's.

Secondly, we replace the elements d_{in} of the models by a specific feature (such as sum of ring data in our Experimental Inspection System) of the light scattered by the scratch. The modified B_{mn} and G_{mq} models will be called a *Belt Model*, β_{mn}, and a *Grid Model*, γ_{mq}, respectively. The following procedure can be used to determine γ_{mq} and β_{mn} experimentally.

1. For a detected scratch, choose q positions along the scratch with inter-distances ΔL. The strating position does not have to be the starting point of the scratch. The two ends of the scratch may be excluded from the process of shape construction to make the process faster.
2. For each position along the scratch, scan the width of the scrach by laser, acquiring p data sets of the scattered light intensity at p points separated from one another by $\Delta\omega$.
3. Reduce the data sets of step (2) by extracting a feature from each set. These features for a longitudinal position n form a Belt Model of the form:

$$\beta_{pn} = (F_{1n} \quad F_{2n} \quad F_{3n} \quad \cdots \quad F_{pn}) \tag{5.7}$$

   at that point.
4. Use the q Belt Models to form a Grid Model for the flaw. Several possibilities are:
   a. From the following γ_{pq} matrix of features and the known values of longitudinal and transversal increments ΔL and $\Delta\omega$, determine a three-dimensional representation for the scratch by constructing

longitudinal and transversal contours, as shown in Figure 5.7.

$$\gamma_{pq} = \begin{bmatrix} F_{11} & F_{21} & \cdots & F_{p1} \\ F_{12} & F_{22} & \cdots & F_{p2} \\ \cdot & & & \cdot \\ \cdot & & & \cdot \\ \cdot & & & \cdot \\ F_{1q} & F_{2q} & \cdots & F_{pq} \end{bmatrix} \tag{5.8}$$

b. Reduce the information of each Belt Model to two items -- the feature corresponding to the deepest point of the scratch at the pertinent cross-section and the corresponding width of the scratch. This will approximate the scratch profiles by a V of varying depth and width. The varying V can be used to construct the approximate scratch shape as sketched in Figure 5.8.

c. Obtain a *mean profile* for the portion of the scratch about the deepest point by averaging the Belt Models of the cross-sections.

The process of determining the Belt and Grid Models is depicted in Figure 5.9 and is implemented for the Experimental Inspection System in program NSMP.

Grid Models were acquired for a number of scratches. A Grid Model consisted of 10 Belt Models, each of which contained 50 elements. Five hundred data acquisitions, therefore, were necessary to produce a Grid Model. Flaw shapes constructed by contours for scratches C2 and C9 are demonstrated in Figures 5.10 and 5.11, while flaw mean profiles obtained

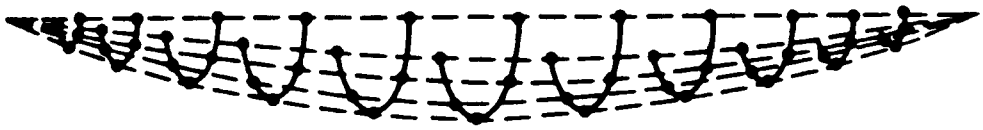

Figure 5.7. Representing scratch shape by contours.

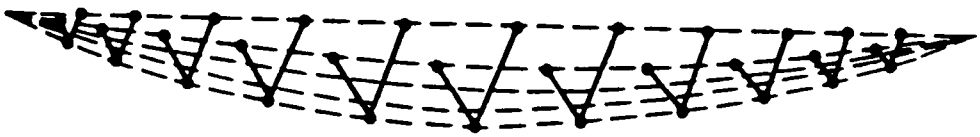

Figure 5.8. Representing scratch shape by a varying V.

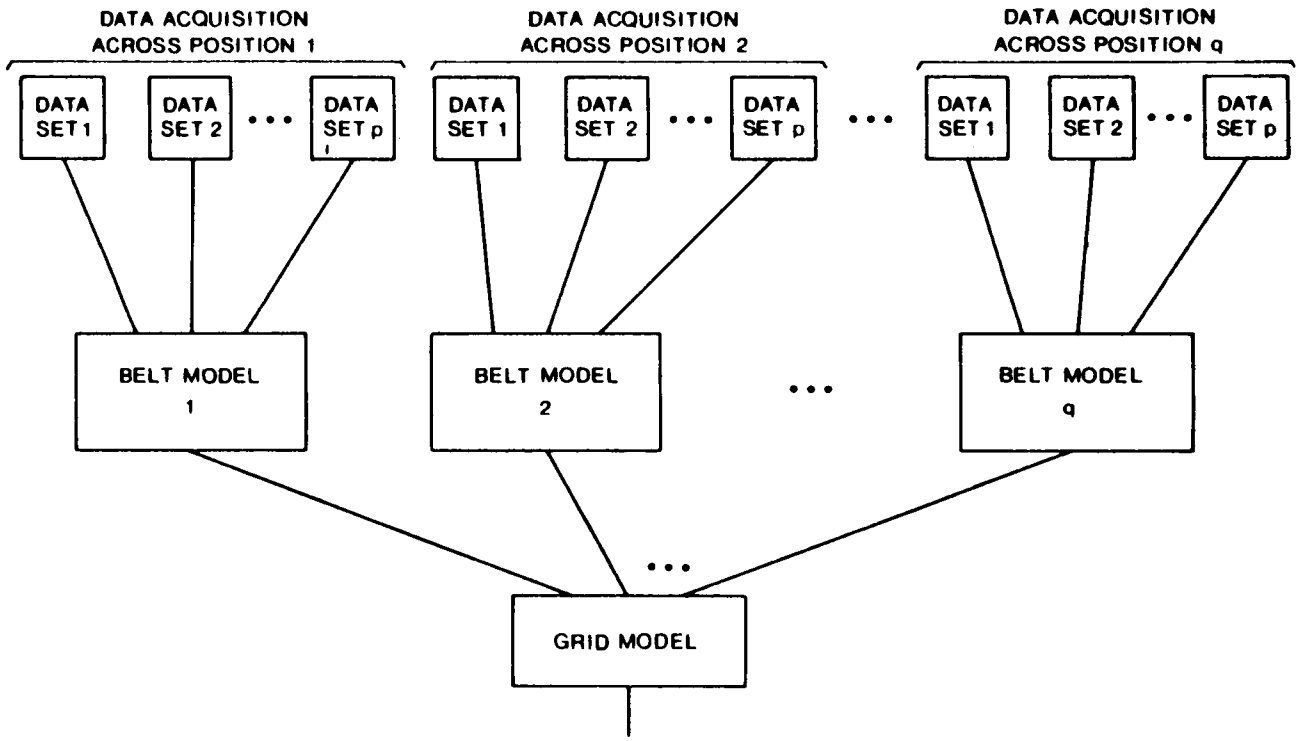

Figure 5.9. Determination of Belt and Grid Models.

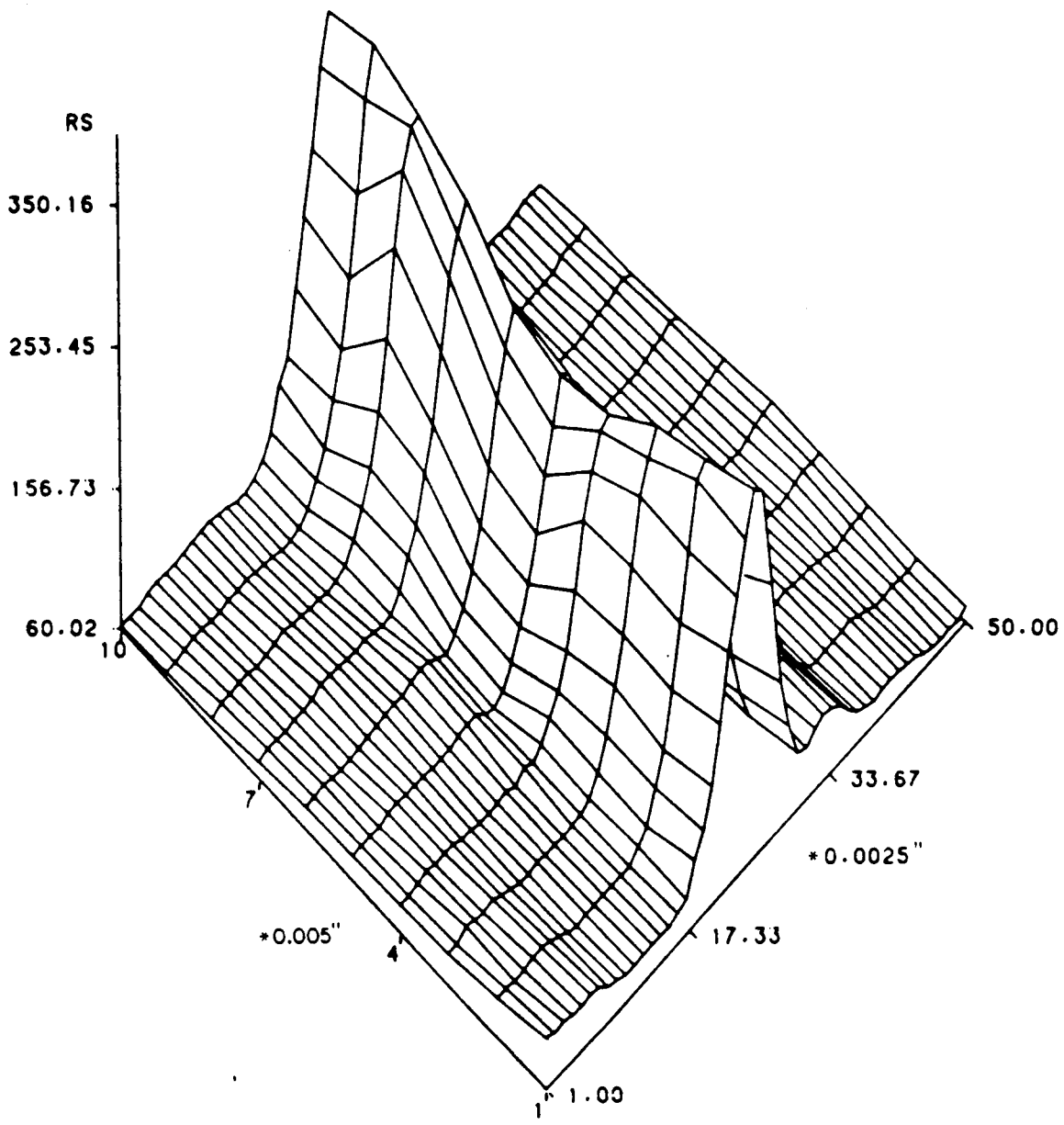

Figure 5.10. Construction of flaw shape by contours for scratch C2.

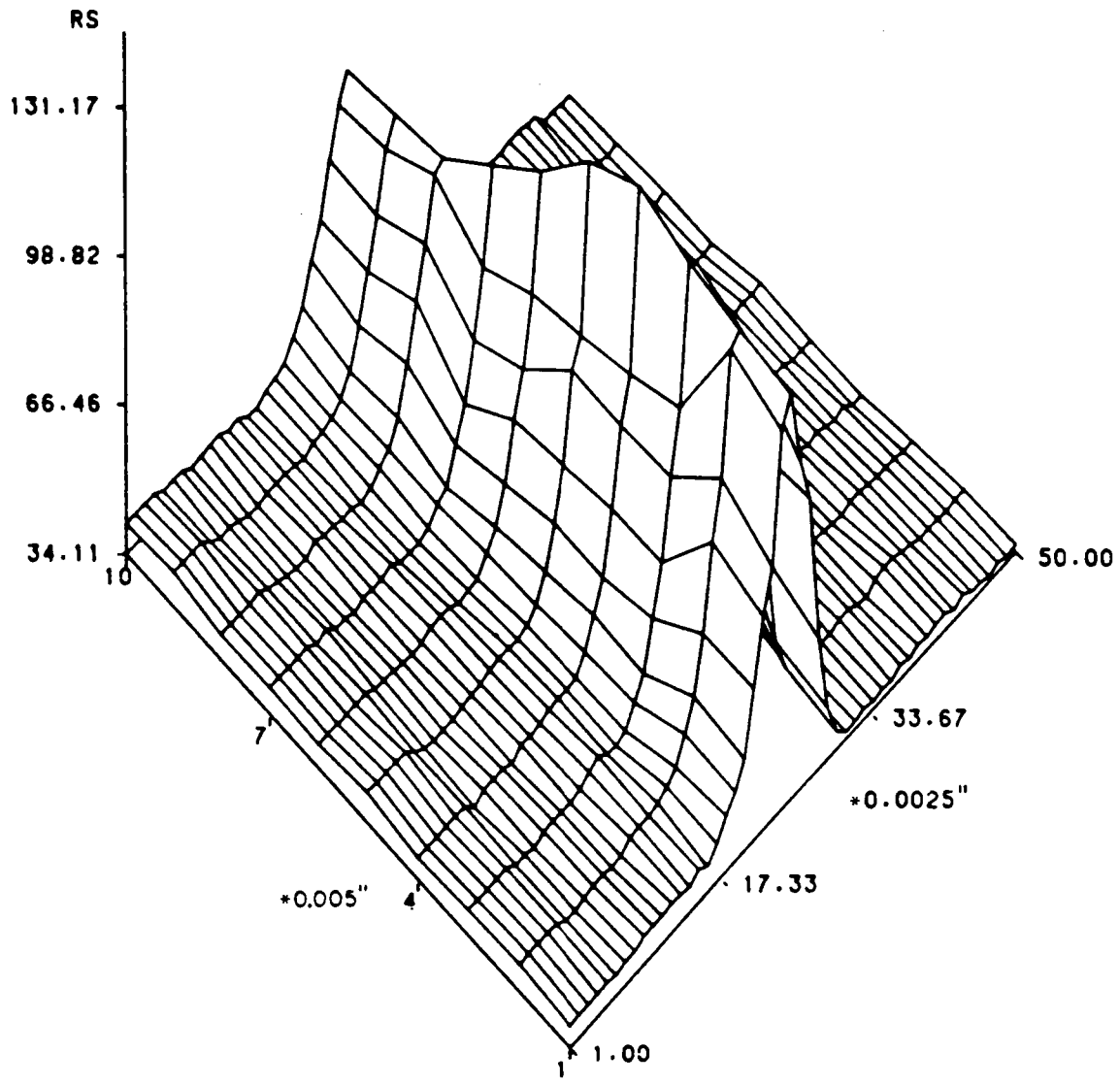

Figure 5.11. Construction of flaw shape by contours for scratch C9.

from Belt Models for scratches C1, C2, C4, and C9 are indicated in Figure 5.12.

Acquisition of the above models revealed some inherent difficulties of determining the flaw shape. The $1/e^2$-diameter of the laser beam used in the experiments is 252×10^{-4}", much larger than the widths of typical scratches. Moreover, the radial distribution of the laser beam intensity is Gaussian and not uniform. These factors combine with the flaw shape in production of the Grid Models for flaws. In fact, the influence of the laser beam seems to be dominant over that of the flaw. In the acquisiiton of the models shown in Figures 5.10 to 5.12, an attempt was made to scan the flaw by the central, rather uniform portion of the Gaussian beam, but the effect of the outer parts of the beam on the flaw could not be eliminated. The resulting profiles demonstrate significantly larger widths than the actual flaw widths. It seems as if the profile is stretched in the horizontal direction. When we contracted these mean profiles by a factor of 20, the profiles shown in Figure 5.13 resulted. The flaw widths given by these profiles are close to the actual calibrated values given by the Light-section Microscope. Nevertheless, it is not easy to determine precise width values from the profiles. This happens because of the effect of ridges in flaws. To determine the scratch shape from the profile, one needs to know from which point on the profile the profile should be inverted. This in turn is dependent on the presence or absence of ridges on the sides of the flaw, an unknown matter. Figure 5.14 shows one of the profiles inverted in four different ways, producing four different shapes for the flaw.

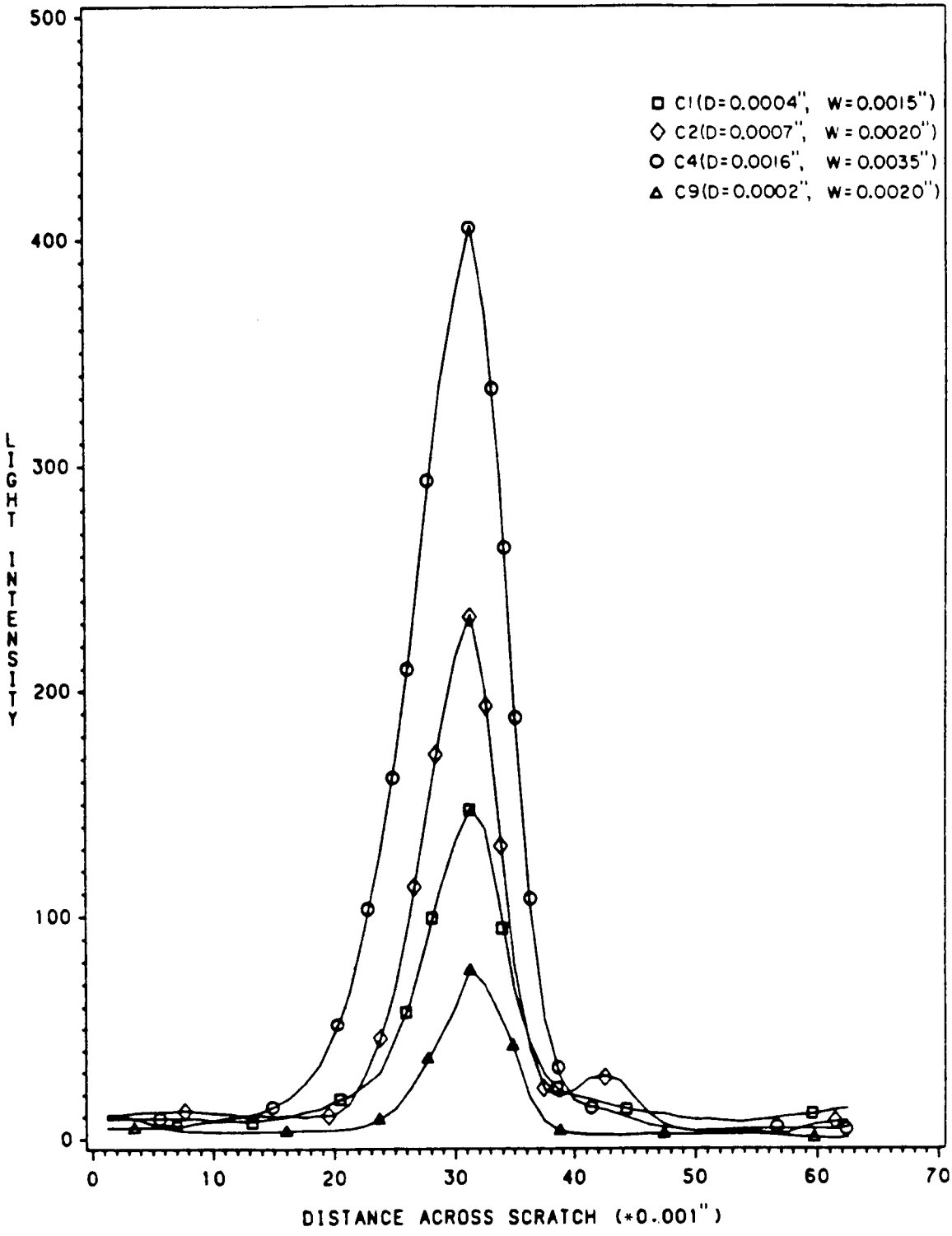

Figure 5.12. Mean profiles for scratches C1, C2, C4, and C9.

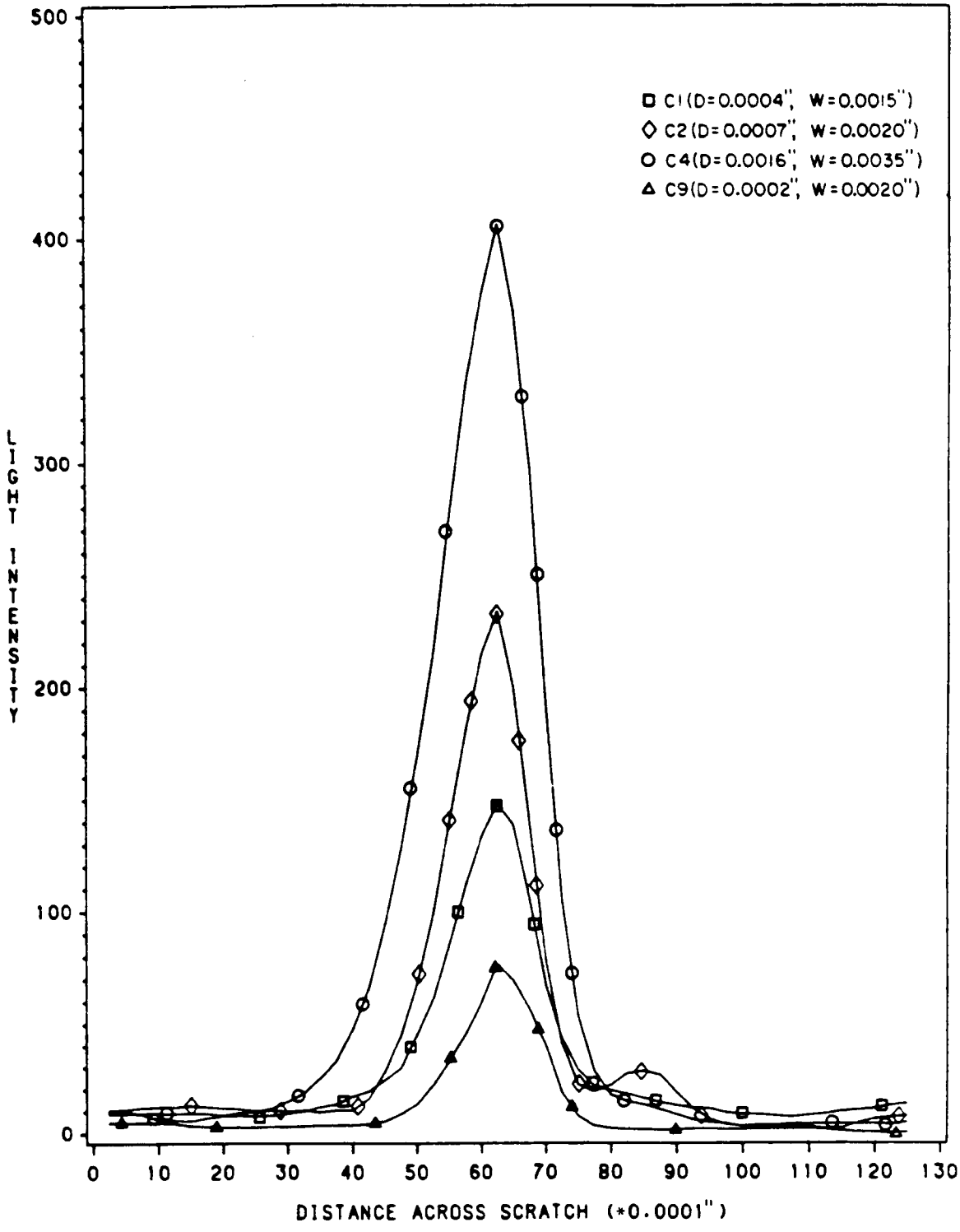

Figure 5.13. Contracted mean profiles for scratches C1, C2, C4 and C9.

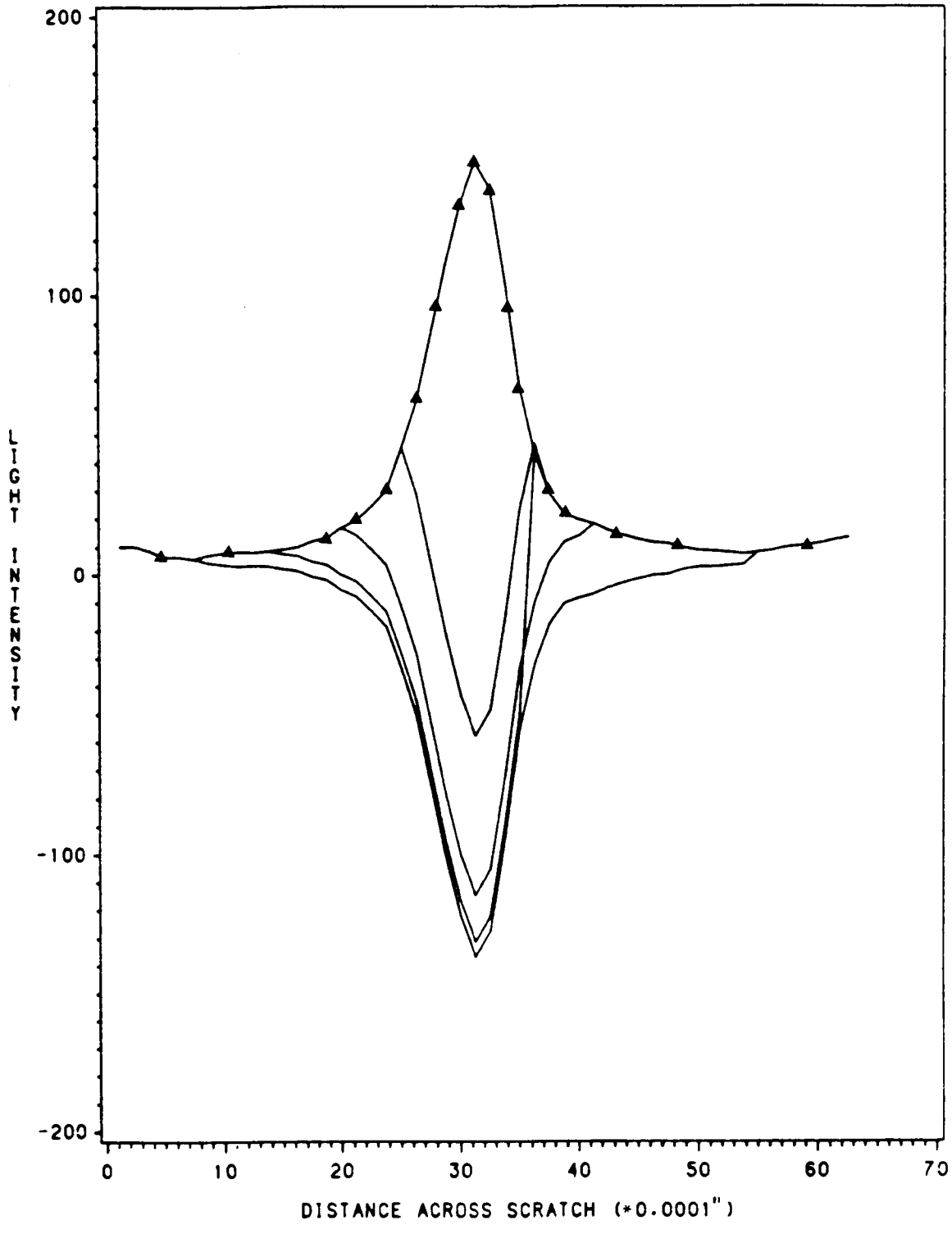

Figure 5.14. Inverting a Belt Model profile in several ways for obtaining flaw shape.

We conclude this section by the following remarks:

1. The shapes of the profiles produced by the Grid Models is strongly influenced by the laser beam intensity and size.
2. Determination of flaw width and ridges is not feasible from the Grid Models uniquely.
3. The depths of the flaws and the peaks of the profiles can be related by a deepest-point contour along the scratch.
4. Producing Varying-V Models for flaws seems to be more feasible than the complete construction of the flaw shape.

The last remark will be further discussed in the following section.

5.5 Flaw Measurement

Precise quantitative determination of flaw dimensions or shape is more stringent and more difficult than characterization of flaws. Considering the results of flaw characterization discussed in the previous section, expectations regarding flaw measurement should not be very high. This section examines several ways of relating data features to flaw dimensions.

5.5.1 Experimental Models

The theoretical light scattering models developed in Chapter 3 indicate the dependence of the light scattered from a flaw surface on the flaw dimensions. Although the models are obtained from approximate theories, the relationships are quite complex and cannot be utilized in

experimental work. Simpler models are needed which allow measurement of flaw dimensions.

Examination of the theoretical models shows the dependence of these models on the sine and cosine functions and different powers of flaw dimensions. The expressions will be considerably simplified if each side of the models is replaced by its own logarithm. This occurs because the logarithm of sine and cosine funcitons can be expressed as polynomials of their argument, producing models in terms of different powers of flaw dimensions.

Considering the above points, we selected a general linear model of the form:

$$F = a + bD + CW + d\,U + eV \tag{5.9}$$

for experimentation. In this model variables F, D, and W represent data feature, flaw depth, and flaw width, respectively, and coefficients a through e are unknown constant parameters. Variables U and V are given by:

$$U = D^2 \tag{5.10}$$

and

$$V = W^2 \tag{5.11}$$

Although this model is linear in D, W, U, and V, it is indeed second order in D and W.

The unknown coefficients of the model can be determined from simultaneous solution of the linear regression equations (Harnett [1970]):

$$\begin{cases} na + b\sum D + c\sum W + d\sum U + e\sum V = \sum F \\ a\sum D + b\sum D^2 + c\sum DW + d\sum DU + e\sum DV = \sum FD \\ a\sum W + b\sum DW + c\sum W^2 + d\sum UW + e\sum VW = \sum FW \\ a\sum U + b\sum DU + c\sum UW + d\sum U^2 + e\sum UV = \sum FU \\ a\sum V + b\sum DV + c\sum VW + d\sum UV + e\sum V^2 = \sum FV \end{cases} \tag{5.12}$$

where n is the number of samples used.

The linear model will be determined and evaluated in several forms in the following section.

5.5.2 Flaw Measurement by the Linear Model

The seven scratches C1, C2, C3, C4, C6, C8, and C9 were used for determining the coefficients a through e of the lienar model. The data feature used in the process was sum of the ring data. Several forms of the model and their evaluations are presented below.

1. Assume that the coefficients c, d, and e of the model are zero. Then the model will be first order in D and the best fit can be found from regression Equations 5.12 as:

$$F = 110.61 + 8.49\,D \ . \tag{5.13}$$

This model will be referred to as Model 1.

2. If coefficients c and e of the general model are allowed to be zero, a second-order model in D results. Coefficients a, b, and d are then found to give this model (Model 2) as:

$$F = 117.08 + 5.84\,D + 0.162\,D^2 \quad . \tag{5.14}$$

Determination of depth from this model for a given value of the feature requires the solution of a second-order equation which may produce two, one, or no acceptable answers.

3. A piecewise fit to the features is likely to produce improved results. Figure 5.15 shows the sum of ring data versus flaw depth. We distinguish four regions for the depth, as shown on the diagram. The best fits for these regions are (Model 3):

$$\begin{array}{lll} \text{Region 1:} & D = 0.0143F - 0.457 & F \le 102 \\ \text{Region 2:} & D = 0.047F - 3.78 & 102 < F \le 166 \\ \text{Region 3:} & D = 4.7 \pm \sqrt{0.961\,F - 160} & 166 < F \le 223 \\ \text{Region 4:} & D = 0.352\,F - 66.64 & 223 < F \end{array} \tag{5.15}$$

4. A first-order model in D and W can be obtained if the coefficients d and e of the general model are zero. The other coefficients can be found from the regression equations to give a model (Model 4) of the form:

$$F = 111.68 + 9.37\,D - 0.297\,W \quad . \tag{5.16}$$

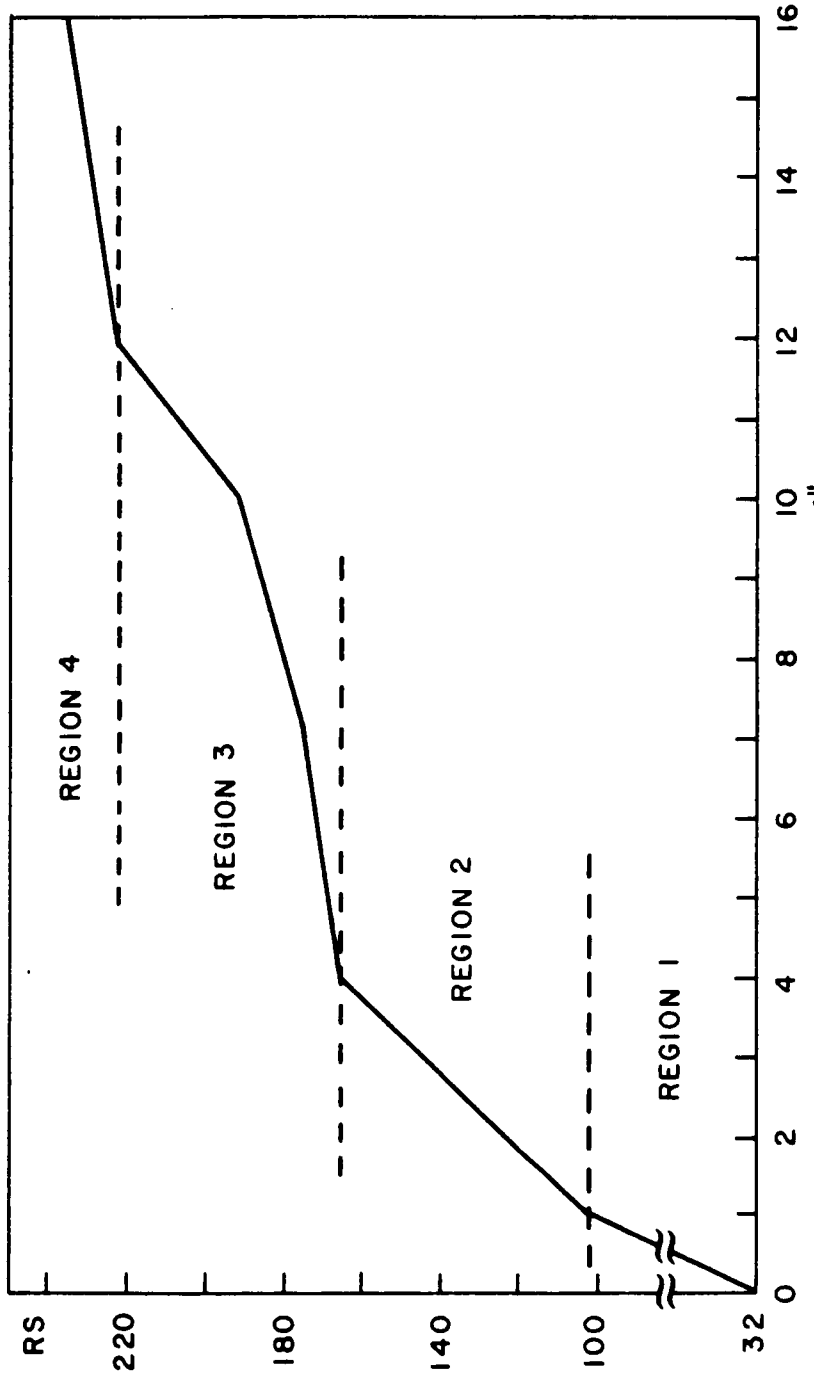

Figure 5.15. Different feature regions for Model 3.

Evaluation of this fit requires more information than merely the feature.

5. As the final fit, we consider the general model in its entirity and find the unknown coefficients. The result (Model 5) is:

$$F = 160.02 + 16.06\,D - 0.34\,D^2 - 4.76\,W + 0.06\,W^2 \ . \tag{5.17}$$

Here again the second-order equation may produce unacceptable or two acceptable values for the flaw depth or width.

The performance of the five models obtained above was examined by performing measurement of a number of calibrated flaws. Tables 5.10 and 5.11 show the results of evaluation and the error percentages of the measurements, respectively. The following rules were observed in selecting the depth values for the tables:

1. If the model has a single negative, two negative, or two complex roots for a given test, disregard the test.
2. If the model has two positive roots, choose the larger root when Model 3 is used and choose the smaller root when Model 5 is used.
3. If the model has one positive and one negative root, choose the positive one.

The first seven flaws in the mentioned tables are those used in determining the coefficients of the models. The best measurement for these flaws, on an average basis, includes 1.8% error and is obtained from Model 3. The second group of flaws, however, are not used in the development of the models. These flaws are best measured by Model 4 with an average

Table 5.10. Evaluation of models used for flaw depth measurement.

FLAW	CALIBRATED Depth ($1*10^{-4}$")	MEASURED DEPTH ($1*10^{-4}$")				
		MODEL 1	MODEL 2	MODEL 3	MODEL 4	MODEL 5
C8	1	NEGATIVE	NEGATIVE	1.00	NEGATIVE	0.93
C9	2	1.44	0.96	1.99	1.82	2.51
C1	4	6.50	6.98	4.01	6.25	5.03
C2	7	7.59	8.09	7.56	7.39	7.23
C6	10	9.59	10.04	9.66	9.85	12.40
C3	12	13.28	13.29	11.98	12.87	COMPLEX
C4	16	14.62	14.39	15.97	14.24	COMPLEX
B4	4	3.03	3.05	2.63	3.59	5.14
A7	5	4.04	4.26	3.03	4.50	5.95
C10	7	9.80	10.24	9.83	10.04	12.71
B5	9	5.54	5.96	3.63	6.17	7.81
B6	13	17.92	16.95	25.83	17.54	COMPLEX

Table 5.11. Error percentages of flaw depth measurements.

FLAW	CALIBRATED Depth ($1*10^{-4}$")	DEPTH MEASUREMENT ERROR				
		MODEL 1	MODEL 2	MODEL 3	MODEL 4	MODEL 5
C8	1	–	–	0.0%	–	-7.0%
C9	2	-28.0%	-52.0%	-0.5%	-9.0%	25.5%
C1	4	62.5%	74.5%	0.3%	56.2%	25.7%
C2	7	8.4%	15.6%	8.0%	5.6%	3.3%
C6	10	-4.1%	0.4%	-3.4%	-1.5%	24.0%
C3	12	10.7%	10.7%	-0.2%	7.2%	–
C4	16	-8.6%	-10.1%	-0.2%	-11.0%	–
Average		**20.4%**	**27.2%**	**1.8%**	**15.1%**	**17.1%**
B4	4	-24.3%	-23.7%	-34.2%	-10.2%	28.5%
A7	5	-19.2%	-14.8%	-39.4%	-10.0%	19.0%
C10	7	40.0%	46.3%	40.4%	43.4%	81.6%
B5	9	-38.4%	-33.8%	-59.7%	-31.4%	-13.2%
B6	13	37.8%	30.4%	98.7%	34.9%	–
Average		**31.9%**	**29.8%**	**54.5%**	**26.0%**	**35.6%**
Overall Average		**25.6%**	**28.4%**	**23.8%**	**20.0%**	**25.3%**

error rate of 26%. If all of the 12 flaws are considered together, the rate of error in measurement comes to 20%.

Table 5.10 also shows some problems occuring about the two extremes of the scale -- several of the depth values given by the models are complex numbers and some are negative. Such cases mostly will not happen if second-order models in depth are not used. Also, a piecewise fit is more appropriate for accomodating the problems in question.

A second point is that for the presented measurements of depth by models which incorporate flaw width, we used the known widths of the flaws. For an uncalibrated flaw, the width must be determined in some way before flaw depth can be found. In such a case, the depth measurement error may increase due to the errors of measurement of the width. The next section will present a method for the measurement of flaw width.

We conclude that a piecewise linear model in terms of flaw depth and a single linear model in terms of flaw width and depth deserve attention for flaw measurement. It must also be reiterated that the calibrated values, which form the source of our judgement about the measurements, themselves may not be very accurate. The given depth and width calibrations were measured at one point along the scratch and do not necessarily hold for the entire length of the scratch. In fact, we are certain that the width and shape of the flaw go through microscopic changes at various points of the flaw. This means that the calibrations may be close to the actual flaw dimensions, but they are not very accurate. And unfortunately, this is the best calibration we can have!

5.5.3 Width Measurement and the Varying-V Models

Inclusion of the flaw width in the experimental models fundamentally should increase the accuracy of flaw depth measurement. However, in the actual experiments, the opposite might be true. Incorporation of width in the models is highly likely to reduce the measurement accuracy when the given width itself is erroneous. As a result, depth measurement using such models becomes a double task -- the precise measurement of width and the subsequent determination of depth.

One way to resolve the problem is to solve simultaneously two models for the specific point under test. These two models can have different functional forms and use one data feature, or they may have the same functional form but utilize two different data features. In the previous section, we obtained the first-order model:

$$RS = 111.68 + 9.37\,D - 0.297\,W \qquad (5.18)$$

usign the sum of ring data (RS) for obtaining the regression coefficients. If we use the first peak of the ring data (RP1) of the same data sets, we arrive through the solution of regression equaitons at the model:

$$RP1 = 48.31 + 2.834\,D - W \; . \qquad (5.19)$$

Now, for any point along the scratch, the flaw depth and width can be calculated from the simultaneous equations:

$$\begin{cases} 9.37\,D - 0.297\,W = RS - 111.68 \\ 2.834\,D - W = RP1 - 48.31 \end{cases} \tag{5.20}$$

if the values of RP1 and RS for that point are known. This approach was evaluated through the testing of the 12 flaws used in the previous section. The results are shown in Table 5.12. Depth is measured by this method with an average overall error of 20.8%. This performance is almost the same as that of Model 4 of previous section in which calibrated width values were used! Measurement of flaw depth through this method is, therefore, worth consideration.

Measurement of flaw width is fulfilled by this method with the rather large average error of 42.3% for the 12 scratches. However, given that the flaw ridges act as scatterers and almost all the test flaws have ridges on one or two sides, the measurements include the ridges and may not be as poor as they look.

We tried another way of determining the flaw width for serving as a source of comparison. This approach used Model 3 of the previous section to determine the flaw depth and used Model 4 to obtain the flaw width. The results were much worse than the above results and will not be presented here.

The simultaneous solution of two models as discussed above can be used to construct a Varying-V Model for a flaw. An example is illustrated in Figure 5.16. Part (a) of this figure shows a constant-depth constant-width scratch calibrated by a Light-section Microscope at one point while Part (b) illustrates the measured Varying-V Model for it. Figure 5.16

Table 5.12. Measurement of flaw depth and width by two models.

FLAW	GIVEN D ($1*10^{-4}$")	GIVEN W ($1*10^{-4}$")	MEASURED D ($1*10^{-4}$")	MEASURED W ($1*10^{-4}$")	% ERROR IN D	% ERROR IN W
C8	1	20	–	26	–	30.0%
C9	2	20	2.11	29.02	5.5%	45.1%
C1	4	15	6.69	29.17	67.2%	94.5%
C2	7	20	7.83	33.89	11.9%	69.4%
C6	10	40	9.18	32.94	-8.2%	-17.6%
C3	12	30	12.27	11.26	2.2%	-62.5%
C4	16	35	14.09	30.37	-11.9%	-13.2%
Average					**17.8%**	**47.5%**
B4	4	30	3.52	27.86	-12.0%	-7.1%
A7	5	30	4.35	25.27	-13.0%	-15.8%
C10	7	40	9.07	9.61	29.6%	-76.0%
B5	9	40	5.73	26.11	-36.3%	-34.7%
B6	13	45	16.95	26.18	30.4%	41.8%
Average					**24.3%**	**35.1%**
Overall Average					**20.8%**	**42.3%**

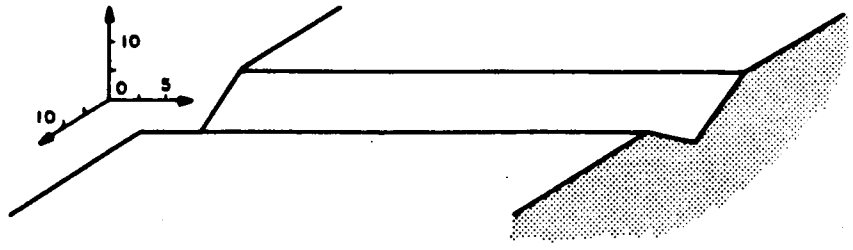

(a)

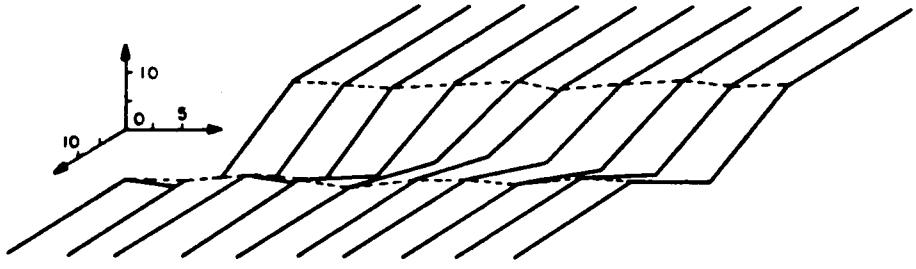

(b)

Figure 5.16. Comparison of the Light-section Microscope calibration and a Varying-V model for scratch C2.

indicates a large error in the measured flaw width. However, considering that the random ridges on the sides of the flaw act as scatterers and thus make the effective width of the flaw larger, the width measurements may not be as erroneous as they seem to be.

CHAPTER 6

CONCLUSIONS AND RECOMMENDATIONS

Automatic Visual Inspection is working its way towards widespread implementation on the plant floor, where the scope of its applications is boundless. Vision system components which previously constituted barriers to rapid development of the field outside laboratories have now reached a level of maturity and cost-effectiveness which permits the development of efficient vision systems for industry. In the coming years there will be explosive growth in the employment of automated systems for visual inspection.

Automating inspection of manufactured surfaces is not as easy as automating many other inspection tasks. In this case, the nature of the problem involves serious difficulties; the variables interact, metal surface characteristics differ, and environmental effects interfere. Researchers have been studying this application for well over a decade now, yet no breakthrough appears near. In fact, it is likely that complete descriptions of metal surface roughness will not be possible for quite some time.

This work has examined the inspection of machined metal surfaces with emphasis on flaw depth qualification. The investigation has utilized a Wedge/Ring Detector for sensing the laser light scattering from the surface of flaws. Study of the detector signals and the light scattering theories produced the following conclusions.

Mathematical analysis of the problem can be performed only through *approximate* light scattering theories. Three such theories, which were referred to as Point-Source, Tangent Plane, and Perturbation Theory approximations, were examined for a flaw with a piecewise linear profile. The first two methods were based on evaluating the integral theorem of Helmholtz and Kirchhoff by approximating the electric field and its normal derivative on the flaw surface. The third method, however, calculated the probability that light is diffracted into a small solid angle. The three theories indicated that the light scattered from a flaw surface is dependent on the light wavelength, light source position, observation point, surface area under radiation, electrical properties of the surface, flaw depth, flaw width, flaw shape, and flaw ridges. Furthermore, the theories suggested that the flaw parameters compoundly influence the scattered light and that the observed light intensity and the flaw depth do not show a one-to-one relationship. This means that two flaws of different depths can produce the same light intensity at the observation point. As the inverse problem, for a given observed light intensity, the light scattering models may suggest more than one value for flaw depth -- an undesirable feature for flaw depth inspection!

The study of the theories clearly indicated the contribution of flaw shape and ridges to the scattered light. Three parameters, called the scratch shape constant, scratch-valley shape factor, and scratch-ridge shape factor, were defined for the piecewise linear flaw profile to represent the effects of flaw shape.

To perform experimental work, a system was selected mainly based on the criterion that it must be simple, and implementable and operatable on the production floor. As a result, the optical components of the system were made minimal, with very little need for adjustment. Also, the angles of incidence and observation for the scattered light were made very small to convey more information about the surface roughness and to represent flaw parameters more accurately.

Initial experiments indicated that the dark currents of the detector elements deviated from their nominal value by -67.7% to 103.3%. The detector also was found to be very sensitive to environmental lighting. This sensitivity can be reduced by adding an appropriate red filter in front of the sensor. Larger rings of the detector were saturated very easily. The five largest rings, for example, went into saturation before rings 1 or 2 even responded to changes in the light intensity. This sensitivity of the detector made control of environmental lighting an absolute necessity for meaningful operation of the system.

As a way of eliminating the effect of environmental lighting, for each data acquisition from the flaw, a second data set was acquired from a defect-free area of the surface, and this second data set was subtracted from the flaw data set. This was expected to debias the flaw data from the background lighting. However, experiments showed that this method introduced inconsistencies into the behaviour of the flaw data. In addition, the method also required twice as many data acquisitions. For these

reasons, environmental lighting was not eliminated; it was controlled very tightly.

Another characteristic of the detector was the production by its different elements of unequal signals for the same incident light intensity. This happened because the elements of the detector had unequal surface areas. To compensate for this, each element signal after conversion to decimal was normalized by the area of the element. However, the Uniform Lighting Test showed that this correction was effective only for the wedges and the middle rings; for the rest of the rings further correction was necessary.

An interactive procedure was then developed to correct all the detector data together. The procedure computed a calibration coefficient for each detector element to transform each ring datum to the mean of the data of middle rings and each wedge datum to the mean of the data of all the wedges. The procedure was run several times and produced a set of calibration coefficients which corrected the data very satisfactorily for various light intensities. These coefficient calibrated all the data before use in any experiment.

With the necessary preprocessing of the data finalized, the inspection experiments were performed. Correlation between 30 different features and flaw depth was studied to determine which feature represented the flaw depth best. The study was based on statistical attributes of the feature samples, sensitivity of the features to flaw width, and separation of the

sample clusters. A parameter, called cluster separation coefficient, was defined for each feature to give a measure of intercluster separation.

As predicted by the light scattering theories, none of the 30 features showed a perfect one-to-one relationship with flaw depth. Dependence of the features on the flaw width and shape was witnessed very clearly. Altogether, the study determined four features as the most appropriate for flaw depth inspection. These features were sum of ring data (RS), total energy multiplied by peak of ring data (T * P), first peak of the ring data (RP1), and the ratio of the sum of ring data 5 through 32 to the sum of ring data 16 through 32 (RSR). These features were further evaluated through the inspection of some calibrated flaws.

Flaw detection was considered with a depth threshold values of 0.0010 inch. A flaw was assigned to the NO-GO or GO class based on the flaw depth exceeding or not exceeding the threshold. Two techniques from pattern recognition were used for decision making -- the minimum distance classification rule and the Bayes classification rule. The two classifiers were first trained to recognize the GO and NO-GO classes and were then put into test.

Experiments showed that the minimum distance classifier performed better than the Bayes classifier, although the performance of the Bayes rule is supposed to be statistically optimal. To explain this, the samples were examined. This examination revealed that the distribution of samples did not have a familiar form while the Bayes classifier used in the experiments assumed a Gaussian density function for the samples. The minimum

distance classifier gave the best result of 100% correct detection for the sum of ring data. However, this rate fell for those flaws whose depth was close to the threshold and whose width was much different from those of the flaws used in training of their class. Such errors cannot be eliminated unless an only depth-dependent feature or a model which appropriately relates a feature to flaw width and depth is found. The following guidelines were suggested for minimizing the errors:

1. Training and inspection for surfaces of various materials or quality must be performed separately.
2. Classifier training and flaw inspection, if possible, should be performed in separate groups based on flaw widths.
3. Training flaws must be chosen with care to produce a balanced set about the threshold.

Two ways of flaw characterization were examined in this work. In the first method, in addition to specifying the part as acceptable or unacceptable, the system specified the range of flaw depth. A case of four depth ranges was selected, and the minimum distance classifier was trained to recognize the four classes. The sum of ring data produced the best performance of 84% correct classification for the training patterns and 53% for the testing patterns. These results could not be improved significantly through the use of multiple features in the minimum distance classifier nor through the use of a tree classifier. The latter, however, showed that classes 1 and 2 were easily separable from classes 3 and 4; but none of the features could effectively distinguish between classes 1 and 2 or

3 and 4. Had a feature which could separate class 1 from class 2 or class 3 from class 4 been identified, the tree classifier would have performed much better.

The adverse effects of flaw width and riges on depth inspection are felt more strongly here than in flaw detection since the depth ranges are smaller and the potential for error higher. A special set of flaws was selected to show the seriousness of this problem. Each flaw was selected so that its depth was close to one of the thresholds while its width was much different from the width of training flaws of its class. These flaws were classified by the classifier 100% wrongly!

The second method of flaw characterization considered here consisted of modeling and shape construction for the flaw. Experimental Belt Models which gave the flaw profile at one point were defined, and Contour Grid Models, Varying-V Models, and Mean Profiles were introduced for combining different Belt Models obtained along the flaw. Procedures were devised for obtaining the models for a flaw, and a few examples were presented.

An inherent limitation was observed in determination of flaw shape from the Grid Models. The laser beam diameter is much larger than typical scratch widths, and the radial distribution of its intensity is Gaussian. These effects combined with the flaw characteristics in making of the Grid Models. In fact, the impact of the laser beam seems to dominate that of the flaw itself. It looks as though the beam stretches the flaw along its width and makes the profile width many times larger than the actual width of the

flaw. Even if this effect is corrected, flaw width cannot be determined from the profiles uniquely because of the flaw ridges. The Belt Model profiles, therefore, are not very conclusive in determining flaw width or shape; nevertheless, they can be used to locate the deepest point of the flaw.

The last protion of this work examined measurement of flaw dimensions from the observed scattered light. On the basis that the models obtained from light scattering theories would reduce to polynomials in flaw dimensions when further simplifications were made, a general linear model was considered for measurement experiments. The model was second-order in flaw depth and flaw width, and its coefficients were determined by linear regression techniques. Several forms of the model was then used to determine flaw depth or depth and width for a given feature.

Flaws used in determining the regression coefficients were meausred at best with an average error of 1.8% by a piecewise fit. Other flaws also were measured and showed an average measurement error of 26%. It must be remembered that the source of judgement on all the experimental results had been the calibration values given by the Light-section Microscope. These values most probably were not very accurate for the entire length of the flaw. This meant that the experimental results might have been somewhat better or worse than those given here.

Through experimenting with different forms of the general linear model, it was concluded that avoiding second-order terms is preferable since their inclusion in the model could result in ambigious results for flaw depth. A piecewise linear fit for depth and a linear fit in depth and width

were found to be the most favorable experimental models. The latter, however, will necessitate determination of flaw width before the depth can be calculated and will introduce the errors of the computed width in flaw depth measurement.

Two methods of determining flaw depth and width were examined. In the first method, two first-order models, relating flaw depth and width to two different features, were solved simultaneously to given flaw depth and width. The second approach, on the other hand, determined one of the two variables independently from a model and used that value in a second model in terms of depth and width to determine the other variable. Experimental evaluation the first method showed average error rates of 17.8% and 47.5% in measuring the depth and width of flaws used for finding regression coefficient and average error rates of 24.3% and 35.1% in measuring other flaw depths and widths. This makes the overall average error rates 20.8% for depth and 42.3% for width. The results obtained through the second approach were much worse than the above results.

Finally, the simultaneous solution of models was used to obtain Varying-V Models for flaws. Such models seem to be the best shape representations possible with the present system.

This work took a unique look at the problem of flaw inspection on machined metal surfaces. The theory of the problem was developed to a certain degree; models for flaw light-scattering were introduced; detection, characterization, and measurement of flaws were investigated; and results which in most cases were below acceptable levels, but not too discouraging

were obtained. However, much more investigation is needed before the problem comes to a complete solution. The theory of light scattering from metal surfaces must be studied further, and simple models must be developed to describe the behavior of metal surfaces in scattering the light incident upon them. One possibility in such a study is consideration of statistical atributes of the surfaces and utilization of statistical models.

On the experimental side, three routes can be taken. The first route is to use the same system chosen in the present work and try to improve the results (for example, by changing the optical components). The second route suggests a new approach which utilizes a TV camera and incandescent lamps. Here models will use image(s) of the flaw and digital image processing techniques to determine flaw dimensions. The third route is to employ a laser as the light source and a camera as the sensor. in this method, the camera will use the light patterns diffracted from the flaw to determine the flaw characteristics.

Among these three choices, the first and the last are likely to produce a solution more quickly. However, the first approach has some drawbacks which make it undesirable. The Wedge/Ring detector requires optical components, and is very sensitive to environmental lighting. Consequently, the detector is not appropriate for the precise measurements in question here. Through experimentations with the sensor, the author has come to the conclusion that this sensor should not be recommended for further work. A camera can effectively replace the Wedge/Ring detector and the same approach utilized in this work can be pursued.

As the third route does not include focusing of the diffracted light onto the camera, the approach will study the belt-like diffracted light patterns to determine flaw parameters. It is easily observable in the laboratory that the distribution and intensities of the constituents of such patterns are related to the flaw width and depth. The nature of the relationship must be investigated. The pursuit of this route is recommended for further investigations.

Inspection of machined surfaces at all levels requires further research and investigation. Flaw detection, although achievable at an acceptable level, can be improved and made more reliable with more appropriate features. More suitable features are needed to classify flaws into various classes based on their depths. Other forms of flaw characterization and measurement will also benefit from data features which reflect only flaw depth or only flaw width strongly. Methods must be devised for determining flaw width and flaw ridges, and experimental models must be developed to allow measurement of flaws more accurately.

BIBLIOGRAPHY

BIBLIOGRAPHY

Aalderink, B. J. and De Jong, M. W. C. [1976]. "Automatic Surface Inspection of Cold-Rolled Sheet at the Temper Mill," Proc. of the Int'l Meeting of Iron and Steel making, pp. 6.2.1, 1-9.

Andrews, H. C. [1978]. *Digital Image Processing*, IEEE Computer Society, New York.

Atkinson, B. M. and Heywood, P. W. [1982]. "Automated Inspection - The Challenge of Vision," Proc. of the 6th Int'l Conf. on Automated Inspection and Product Control, pp. 173-178.

Barnard, S. T. [1980]. "Automated Inspection Using Gray-scale Statistics," Proc. of the 5th Int'l Joint Conf. on Pattern Recognition, pp. 269-272.

Barton, J. R. and Kusenberger, F. N. [1977]. "CIBLE Data Base Acquisition on New and Used Bearings," Proc. of Eleventh Symp. on Nondestructive Evaluation, So. Texas Section, pp. 130-149.

Barton, J. R. and Kusenberger, F. N. [1982]. "Computer Aided Nondestructive Inspection of Ball and Roller Bearing Components," Proc. of the 6th Int'l Conf. on Automated Inspection and Product Control, pp. 297-306.

Batchelor, B. G. [1978]. *Pattern Recognition Ideas in Practice*, Plenum Press.

Batchelor, B. G. and Williams, G. A. [1979]. "Defect Detection on the Internal Surfaces of Hydraulic Cylinders for Motor Vehicles," Proc. of the Conf. on Imaging Applications for Automated Industrial Inspection and Assembly, pp. 65-78.

Batchelor, B. G., Marlow, B. K., Smith, B. D. V. and Verson, M. J. [1980]. "A Research Laboratory For Automatic Visual Inspection," Proc. of the 5th Int'l Conf. On Automated Inspection and Product Control, pp. 13-33.

Batchelor, B. G., Hill, D. A., and Hodgson, D. C., [1985]. *Automated Visual Inspection*, IFS Publications Ltd. UK.

Beckmann, P. and Spizzichino, A., [1963]. *The Scattering of Electromagnetic Waves From Rough Surfaces*, Pergamon Press.

Bowden, C.M. [1978]. "Application of Microcomputers to Shop Floor Inspection Problems," Proc. of the 3rd Int'l Conf. on Automated Inspection and Product Control, pp. 203-216.

Brady, M. [1981]. "Seeing Machines: Current Industrial Applications," Mechanical Engineering, Nov. 81, pp. 52-59.

Brananan, L. A. [1979]. "Recent Applications of Electronic Vision to Noncontact Automatic Inspection," Proc. of the Conf. on Imaging Applications for Automated Industrial Inspection and Assembly," pp. 102-107.

Brook, R. A. [1971]. "Automated Inspection of Flat Surfaces," Steel Times Annual Review, pp. 91-98.

Brook, R. A. [1971]. "An Experimental Automatic Surface Inspection System," Metron vol. 3, no. 8, pp. 219-223.

Castleman, K. R. [1979]. *Digital Image Processing*, Prentice-Hall.

Chin, R. T. [1982]. "Machine Vision for Discrete Part Handling in Industry: A Survey" Proc. of the 1982 Workshop on Industrial Applications of Machine Vision, pp. 26-32.

Church, E. L. and Zavada, J. M. [1975]. "Residual Surface Roughness of Diamond-Turned Otics," Applied Optics, vol. 14, no. 8, pp. 1788-1795.

Davies, R. L. [1974]. "The Computer Can't Replace the Inspector," Proc. of the Automated Inspection and Product Control Conference, pp. 223-228.

Don, H. S., Fu, K. S., Liu, R. and Lin, W. W. [1984]. "Metal Surface Inspection Using Image Processing Techniques," IEEE Transactions on SMC, vol. SMC-14, no. 1, pp. 139-146.

Droscha, H. [1978]. "Laser Beam Inspection of Strip Metal Surface Finish," Sheet Metal Industries, pp. 1230-1231.

Duff, M. J. B. and Levialdi, S. [1981]. *Languages and Architectures for Image Processing*, Academic Press.

Dutschke, W. and Keferstein, C. [1982]. "Application of Optical Sensors in West Germany," Proc. of the 1982 Workshop on Industrial Applications of Machine Vision, pp. 33-40.

Elson, J. M. and Ritchie, R. H. [1971]. "Photon Interactions at Rough Metal Surface," Physical Review B, vol. 4, no. 12, pp. 4129-4138.

Fadl, M. F. A. and Parsons, F. G. [1978]. "Electro-Optical Flaw Detection," Proc. of the 3rd Int'l Conf. on Automated Inspection and Product Control, pp. 111-118.

Glass, G. V. and Hopkins, K. D. [1984]. *Statistical Methods in Education*

and Psychology, Prentice-Hall, Inc.

Gonzalez, R. C. and Wintz, P. [1977]. *Digital Image Processing*, Addison-Wesley Publishing Company.

Gonzalez, R. C. and Safabakhsh R. [1982]. "Computer Vision Techniques for Industrial Applications and Robot Control," Computer, vol. 15, no. 12, pp. 17-32.

Goodman, J. W. [1968]. *Introduction to Fourier Optics*, McGraw-Hill Book Company.

Graham, D. and Choong, Y. C. [1982]. "An Intelligent machine Vision Module for Detecting Surface Defects," Proc. of the 6th Int'l Conf. on Automated Inspection and Product Control, pp. 271-279.

Haralick, R. M., Shanmugam, K. and Dinstein, I. [1973]. "Textural Features of Image Classification," IEEE Transactions on SMC, vol. SMC-3, No. 6, pp. 610-621.

Harnett, D. L. [1970]. *Introduction to Statistical Methods*, Addison-Wesley Publishing Company.

Hartwig, G. C. [1981]. "Electro Optics Inspection - Choosing the Right Light for the Job," Mechanical Engineering, May 1981, pp. 64-67.

Harvey, D. M., Hobson, C. A. and Lalor, M. J. [1982]. "Optical Inspection of Small Compnents," Proc. of the 6th Int'l Conf. on Automated Inspection and Product Control, pp. 153-160.

Hecht, E. and Zajac, A. [1979]. *Optics*, Addison-Wesley Publishing Company.

Hill, A. G. [1982]. "A General Applied Economic Study of Automated Inspection and Product Control," Proc. of the 6th Int'l Conf. on Automated Inspection and Product Control, pp. 103-110.

Hirata, Y., Hibara, T. and Tanaka, H. [1982]. "Application of Optical Sensing Techniques to Visual Inspection," Proc. of the 6th Int'l Conf. on Automated Inspection and Product Control, pp. 49-58.

HSDPS-1 Maintenance Manual, PD78-197-107-A1, Recognition Systems, Inc.

HSDPS-1 Operators Manual, PD78-195-105-A0, Recognition Systems, Inc.

Inari, T. [1972]. "Automatic Detection and Control of Surface Roughness by Coherent Diffraction Patterns," Proc. of the 16th Annual Technical Meeting of SPIE, pp. 47-53.

Kasdan, H. L. [1976]. "Linewidth Measurement by Diffraction Pattern Analysis," SPIE vol. 80, Developments in Semiconductor Microlithography, pp. 54-63.

Kasdan, H. L. and Mead, D. C. [1978]. "Automatic Visual Inspection By Optical Computing," Proc. of the 3rd Int'l Conf. on Automated Inspection and Product Control, pp. 73-80.

Kasdan, H. L. [1972]. "Nonparametric Feature Analysis Methods for Sampled Diffraction Patterns," Proc. of the 16th Annual Technical Meeting of SPIE, pp. 187-206.

Kirk, R. E. [1978]. *Introductory Statistics*, Brooks/Cole Publishing Company.

Klingsporn, P. E. [1980]. "Semi-automated Inspection of Superfinished Spherical Surfaces," Report BDX-613-2375, Bendix, Kansas City Division.

Klingsporn, P. E. [1980]. "Determination of the Diameter of an Isolated Surface Defect Based on Fraunhofer Diffraction," Applied Optics, vol. 19, no. 9, pp. 1435-1438.

Klingsporn, P. E. [1980]. "Normalization of The Scattered Light From An Isolated Defect Illuminated by a Guassian Beam," Bendix, Kansas City Division.

Krunger, R. P. and Thompson, W. B. [1981]. "A Technical and Economic Assessment of Computer Vision for Industrial Inspection and Robot Assembly," Proc. of the IEEE, vol. 69, no. 12, pp. 1524-1538.

Lendaris, G. G. and Stanley, G. L. [1970]. "Diffraction Pattern Sampling for Automatic Pattern Recognition," Proc. of the IEEE, vol. 58, no. 2, pp. 198-216.

Logan, I. G. and Macleod, J. E. S. [1974]. "An Application of Pattern Recognition Algorithms to the Automatic Inspection of Steel Strip Surfaces," Proc. of the 2nd Int'l Joint Conf. on Pattern Recognition, pp. 286-290.

Lukes, G. E. [1974]. "Cloud Screening from Aerial Photography Applying Coherent Optical Pattern Recognition Techniques," Proc. of SPIE, vol. 45, Coherent Optics in Mapping, pp. 265-272.

Luxon, J. T. and Parker D. E. [1985]. *Industrial Lasers and Their Applications*, Prentice-Hall, Inc.

Martin, G. [1974]. "Automated Inspection and Product Control," Proc. of the Automated Inspection and Product Control Conference, pp. XIII-XIX.

Mundy, J. L. [1977]. "Automatic Visual Inspection," Proc. of the 1977 Conf. on Decision and Control, pp. 705-710.

Mundy, J. L. [1982]. "Visual Inspection of Metal Surfaces," Proc. of the 6th Int'l Conf. on Pattern Recognition, pp. 227-231.

Mundy, J. L. and Porter III, G. B. [1980]. "Visual Inspection of Metal Surfaces," Proc. of the 5th Int'l Joint Conf. on Pattern Recognition, pp. 232-237.

Norton-Wayne, L. and Hill, W. J. [1974]. "The Automatic Classification of Defects on Moving Surfaces," Proc. of the 2nd Int'l Joint Conf. on Pattern Recognition, pp. 476-478.

Norton-Wayne, L., Hill, W. J. and Brook, R. A. [1977]. "The Automatic Visual Inspection of Moving Steel Surfaces," Brit. Jnl. of NDT, vol. 19, no. 7, pp. 242-248.

Norton-Wayne, L., Watts, C. and Hill, W. J. [1980]. "The Automatic Visual Inspection of Steel Strip," Proc. of the 5th Int'l Conf. on Automated Inspection and Product Control, pp. 143-151.

Ollus, M., Koskinen, K. and Mahlstrom, B. [1982]. "On Systems with Real-time Image Processing in Automated Inspection," Proc. of the 1982 Workshop on Industrial Machine Vision, pp. 101-107.

Parallel I/O Interface manual, Operation and Instruciton manual, MS 79-405, Recognition Systems, Inc.

Perkins, W. A. [1983]. "INSPECTOR: A Computer Vision System that Learns to Inspect Parts," IEEE Trans. on PAMI, vol. PAMI-5, no. 6, pp. 584-592.

Perkins, W. A. [1984]. "Model-based Inspection System For Component Boards," Pattern Recognition, vol. 17, no. 1, pp. 135-140.

Pernik, B. G. [1979]. "Surface Roughness Measurements with an Optical Fourier Spectrum Analyzer," Applied Optics, vol. 18, no. 6, pp. 796-801.

Porter III, G. B. and Mundy, J. L. [1982]. "A Noncontact Profile Sensing System For Visual Inspection," IEEE Workshop on Applications of Machine Vision, pp. 119-129.

Pratt, W. R. [1978]. *Digital Image Processing*, Wiley.

Pryor, T. R., Erf, R. K. and Gara, A. D. [1982]. "Applications of Lasers to Production Metrology, Control and Machine Vision," Proc. of the IEEE, vol. 70, no. 6, pp. 618-626.

Pryor, T. [1982]. "Optical Inspection and Machine Vision," Proc. of the 1982 Workshop on Industrial Applications of Machine Vision, pp. 3-20.

Reich, F. and Coleman, W. J. [1976]. "High-speed Surface Flaw Inspection," Optical Engineering, vol. 15, no. 1, pp. 48-51.

Rosenfeld, A. and Kak, A. C. [1982]. *Digital Picture Processing*, Academic Press.

Safabakhsh, R. [1983]. *Application of Pattern Recognition Technqiues to Automated Surface Inspection*, Technical Report TR-EE-83-45, University of Tennessee, Knoxville.

Safabakhsh, R. [1984]. *Application of Pattern Recognition Techniques to Automated Surface Inspection*, Technical Report TR-EE-84-42, University of Tennessee, Knoxville.

Safabakhsh, R. [1986]. *Application of Pattern Recognition Techniques to Automated Surface Inspection*, Technical Report TR-EE-86-64, University of Tennessee, Knoxville.

Saridis, G. N. and Brandin, D. M. [1976]. "An Automatic Surface Inspection System for Flat Rolled Steel," Proc. of the 1976 Conf. on Decision and Control, pp. 392-397.

Scott, A. J. [1982]. "Why Should I Use Automated Inspection," Proc. of the 6th Int'l Conf. on Automated Inspection and Product Control, pp. 1-5.

Sevcik, A. [1982]. "Methods and Devices For Scanning of the Surface of Bearing's Rotation Parts," Proc. of the 6th Int'l Conf. on Automated Inspection and Product Control, pp. 281-286.

Seymour, L. [1974]. "Planning for Automated Testing," Proc. of the Automated Inspection and Product Control Conf. pp. 23-38.

Stover, J. C. [1975]. "Roughness Characterization of Smooth Machined Surfaces by Light Scattering," Applied Optics, vol. 14, no. 8, pp. 1796-1802.

Suresh, B. R., Fundakowski, R. A., Levitt, T. S., Overland, J. E., Becking, T. L., and Whittenburg, T. M. [1982]. "The Automated Surface Inspection of Hot Steel Slabs," Proc. of the 1982 Workshop on Industrial Applications of Machine Vision, pp. 112-118.

Svelto, O. [1976]. *Principles of Lasers*, Plenum Press.

Swain, P. H. and Hauska, H. [1977]. "The Decision Tree Classifier: Design and Potential," IEEE Trans. on Geosci. Electron., GE-15, pp. 142-147.

Tate, M. W. [1955]. *Statistics in Eduction*, The Macmillan Company, New York.

Thompson, B. J. [1974]. "Introduction to Coherent Optics," Proc. of SPIE, vol. 45, Coherent Optics in Mapping, pp. 3-45.

Tou, J. T. and Gonzalez, R. C. [1974]. *Pattern Recognition Principles*, Addison-Wesley Publishing Comapny.

Walsh, L. C. [1978]. "The U.S.A. Scene," Proc. of the 3rd Int'l Conf. on Automated Inspection and Product Control, pp. 1-8.

Warnecke, H. J. and Blasing, J. P. [1980]. "Visual Inspection - Technical Aids and Computer Automation as Tasks in Industrial metrology," Proc. of the 5th Int'l Conf. on Automated Inspection and Product Control, pp. 1-12.

West, R. N. [1982]. "Laser Scanners for Automatic Inspection of Strip Products," Proc. of the 6th Int'l Conf. on Automated Inspection and Product Control, pp. 287-295.

Weszka, J. S. [1974]. "A Comparative Study of Texture Measurements for Terrian Classification," Proc. of SPIE vol. 45, Coherent Optics in Mapping, pp. 62-64.

Weszka, J. S., Dyer, C. R. and Rosenfeld, A. [1976]. "A Comparative Study of Texture Measures for Terrain Classifications," IEEE Transactions on SMC, vol. SMC6, no. 4, pp. 269-285.

Weszka, J. S. and Rosenfeld, A. [1976]. "An Application of Texture Analysis to Materials Inspection," Pattern Recognition, vol. 8, pp. 195-199.

Williams, T. L. and Corey, H. S. [1983]. "An Automated Wedge/Ring Detector Gage for Characterizing Surface Defects on Machine Parts," In-house Report, Union Carbide Corporation.

Young, A. W. [1974]. "Reliability Consideration in Automated Inspection," Proc. of the Automated Inspection and Product Control Conf., pp. 1-10.

ZEISS Light-section Microscope Manual, CARL ZEISS Oberkochen/Württ.

APPENDICES

APPENDIX A

SCATTERED FIELD FOR A POINT LIGHT SOURCE

The integral theorem of Helmholtz and Kirchhoff

$$\mathbf{E}(P_o) = \frac{1}{4\pi}\int\int_S \left\{ \frac{\partial \mathbf{E}(P_s)}{\partial \mathbf{n}} \left[\frac{\exp(ikR_o)}{R_o} \right] - \mathbf{E}(P_s) \frac{\partial}{\partial \mathbf{n}} \left[\frac{\exp(ikR_o)}{R_o} \right] \right\} ds \tag{A.1}$$

is evaluated in this appendix for a point light source radiating spherical waves onto a flaw with a piecewise linear profile as indicated in Figure 3.3 on page 49. The evaluation assumes flaws with dimensions much larger than the light wavelength λ, and considers local normals.

Assume that a light source located at point P_ℓ above the surface radiates spherical waves onto the surface. The angles of incidence and observation are both equal to α and the local normal $\mathbf{n}$ makes an angle β with the global normal $\mathbf{n}_g$. For the spherical waves at point P_s on the surface we have:

$$\mathbf{E}(P_s) = \frac{\exp(ikR_\ell)}{R_\ell} \tag{A.2}$$

and

$$\frac{\partial \mathbf{E}(P_s)}{\partial \mathbf{n}} = \left(\frac{\mathbf{R}_\ell \cdot \mathbf{n}}{R_\ell} \right) \frac{\partial \mathbf{E}(P_s)}{\partial R_\ell} = -\left(ik - \frac{1}{R_\ell}\right) \frac{\exp(ikR_\ell)}{R_\ell} \cos(\beta - \alpha) \tag{A.3}$$

where

$$k = \frac{2\pi}{\lambda} \tag{A.4}$$

is the *wave number* and R_ℓ is the distance between the light source and a point s on the surface. The normal derivative of the Green's function used in Equation A.1 is:

$$\frac{\partial}{\partial \mathbf{n}}\left[\frac{\exp(ikR_0)}{R_0}\right] = (ik - \frac{1}{R_0})\frac{\exp(ikR_0)}{R_0}\cos(\beta + \alpha) \tag{A.5}$$

where R_0 denotes the distance between the point s and the observation point P_0. Since $k >> 1/R_\ell$ and $k >> 1/R_0$, using Equations A.2, A.3, and A.5, the integrand of Equation A.1 can be found as:

$$\begin{aligned} \mathbf{Y} &= \mathbf{E}(P_s)\frac{\partial}{\partial \mathbf{n}}\frac{\exp(ikR_0)}{R_0} - \frac{\exp(ikR_0)}{R_0}\frac{\partial \mathbf{E}(P_s)}{\partial \mathbf{n}} \\ &= i2k\frac{\exp[ik(R_\ell + R_0)]}{R_\ell R_0}\cos\alpha\cos\beta \ . \end{aligned} \tag{A.6}$$

The flaw dimensions are much smaller than the distance between a point on surface S and the excitation point or the observation point. Consequently, we simplify the exact expressions for R_ℓ, R_0, and $\cos\alpha$ as follows:

$$R_\ell = \sqrt{r_\ell^2 - D_1^2 + (D_1 - z_j)^2} \simeq r_\ell - D_1 z_j \tag{A.7}$$

$$R_o = \sqrt{r_o^2 - D_2^2 + (D_2 - z_j)^2} \simeq r_o - D_2 z_j \tag{A.8}$$

$$\cos\alpha = \frac{D_1 - z_j}{R_\ell} \simeq \frac{D_1}{r_\ell} \ . \tag{A.9}$$

Also, the surface element on the flaw is given by:

$$ds = \frac{1}{\cos\beta}\, dx\, dy \ . \tag{A.10}$$

Using Equation A.6 to A.10 we get:

$$Y\, ds = \frac{C_{5j}}{C_{1j} + C_{2j} x} \exp(kC_{4j} x)\, dx\, dy \tag{A.11}$$

where

$$C_{1j} = r_\ell r_o - (r_o D_1 + r_\ell D_2) b_j \tag{A.12}$$

$$C_{2j} = -(r_o D_1 + r_\ell D_2) a_j \tag{A.13}$$

$$C_{4j} = -(D_1 + D_2) a_j \tag{A.14}$$

$$C_{5j} = i \frac{2kD_1}{r_\ell} \exp[ik(r_\ell + r_o) - ik(D_1 + D_2) b_j] \tag{A.15}$$

$$a_j = \frac{d_{j-1} - d_j}{\omega_j - \omega_{j-1}} \tag{A.16}$$

$$b_j = \frac{d_j \omega_{j-1} - d_{j-1} \omega_j}{\omega_j - \omega_{j-1}} \tag{A.17}$$

To make mathematical manipulations simpler, we temporarily assume that $h_j = -d_j$ for $j = \ell + 1,...,m$. Then for a scratch extending from -L to +L in the y-direction we have:

$$\mathbf{E}(P_o) = \frac{1}{4\pi} \int\int_S \mathbf{Y}\, ds = \frac{L}{2\pi} \int_{-\omega_m}^{\omega_m} \mathbf{Y}\, dx = \frac{L}{2\pi} \sum_{j=1}^{m} \mathbf{I}_{\pm j} \tag{A.18}$$

$$\begin{aligned} \mathbf{I}_{\pm j} &= \int_{+j} \mathbf{Y}\, dx + \int_{-j} \mathbf{Y}\, dx \\ &= 2\, \mathbf{C}_{5j} \int_{\omega_{j-1}}^{\omega_j} \frac{\exp(ikC_{4j}x)}{C_{1j} + C_{2j}x}\, dx \end{aligned} \tag{A.19}$$

From tables of integrals, one can show that

$$\int \frac{\exp(i\,k\,x)}{a + b\,x} dx = \frac{1}{b} \exp\left(-i\frac{ka}{b}\right) Ei\left(i\,\frac{ka}{b} + i\,k\,x\right) \tag{A.20}$$

in which Ei(z) is the Exponential Integral Function given by

$$Ei(z) = \int_{-\infty}^{z} \frac{e^t}{t}\, dt \tag{A.21}$$

Equation A.20 can be used to evaluate the integral in Equation A.19. The result is:

$$I_{\pm j} = \frac{2C_{5j}}{C_{2j}} \exp\left(-ik\frac{C_{1j}C_{4j}}{C_{2j}}\right)\left\{Ei\left(\frac{ikC_{1j}C_{4j}}{C_{2j}} + ikC_{4j}\omega_j\right) - Ei\left(\frac{ikC_{1j}C_{4j}}{C_{2j}} + ikC_{4j}\omega_{j-1}\right)\right\} \tag{A.22}$$

Substitution of Equations A.22 and A.12 to A.17 in Equation A.18 gives the field as:

$$\mathbf{E}(P_o) = \frac{L}{2\pi}\mathbf{F}_1 \sum_{j=0}^{m}\left(\frac{\omega_j - \omega_{j-1}}{d_{j-1} - d_j} - \frac{\omega_{j+1} - \omega_j}{d_j - d_{j+1}}\right)Ei\left(iF_2 + iF_3 d_j\right) \tag{A.23}$$

where

$$\mathbf{F}_1 = \frac{-i4kD_1}{(r_o D_1 + r_\ell D_2)r_\ell}\exp\left(ik\frac{r_o^2 D_1 + r_\ell^2 D_2}{r_o D_1 + r_\ell D_2}\right) \tag{A.24}$$

$$F_2 = k\frac{(D_1 + D_2)r_\ell r_o}{D_1 r_o + D_2 r_\ell} \tag{A.25}$$

$$F_3 = k(D_1 + D_2) \tag{A.26}$$

and $\omega_{m+1} = \omega_m$, $d_{m+1} \neq 0$, and $\omega_{-1} = d_{-1} = 0$.

Now, if we change the depth parameters d_j, $j = \ell + 1, \ldots, m$ of Equation A.23 to height parameters h_j, $j = \ell + 1, \ldots, m$, we get the final result:

$$E(P_o) = \frac{L}{2\pi} F_1 \left\{ \sum_{j=0}^{\ell} \left(\frac{\omega_j - \omega_{j-1}}{d_{j-1} - d_j} - \frac{\omega_{j+1} - \omega_j}{d_j - d_{j+1}} \right) Ei(iF_2 + iF_3 d_j) + \right.$$

$$\left. \sum_{j=\ell+1}^{m} \left(\frac{\omega_j - \omega_{j-1}}{h_j - h_{j-1}} - \frac{\omega_{j+1} - \omega_j}{h_{j+1} - h_j} \right) Ei(iF_2 - iF_3 h_j) \right\} \qquad \text{(A.27)}$$

where F_1, F_2, and F_3 are defined in Equations A.24 to A.26.

APPENDIX B

SCATTERING COEFFICIENT FOR PLANE WAVES

The scattering coefficient

$$\rho = \frac{C(\theta_i, \theta_r, \phi)}{4\ X\ Y} \int\int_S \exp(i\ \mathbf{u} \cdot \mathbf{r})\, dx\, dy \tag{B.1}$$

where

$$C(\theta_i, \theta_r, \phi) = \frac{1 + \cos\theta_i \cos\theta_r - \sin\theta_i \sin\theta_r \cos\phi}{\cos\theta_i (\cos\theta_i + \cos\theta_r)} \tag{B.2}$$

$$\mathbf{u} = \mathbf{K}_i - \mathbf{K}_r = u_x \mathbf{a}_x + u_y \mathbf{a}_y + u_z \mathbf{a}_z \tag{B.3}$$

$$u_x = \frac{2\pi}{\lambda}\left(\sin\theta_i - \sin\theta_r\right) \tag{B.4}$$

$$u_y = \frac{-2\pi}{\lambda}\left(\sin\theta_r \sin\phi\right) \tag{B.5}$$

$$u_z = -\frac{2\pi}{\lambda}\left(\cos\theta_i + \cos\theta_r\right) \tag{B.6}$$

and

$$\mathbf{r} = x\,\mathbf{a}_x + y\,\mathbf{a}_y + z\,\mathbf{a}_z \tag{B.7}$$

is evaluated in this appendix for a scratch rough in the x-direction only and extended in the y-direction from $y=-L$ to $y=+L$. Two scratch profiles are considered--the piecewise linear profile of Figure 3.2 on page 45 and the sinusoidal profile (c) of Figure 3.1 on page 43.

B.1 The Piecewise-Linear Flaw Profile

To make mathematical manipulations for the piecewise-linear profile simpler, we temporarily assume that $h_j=-d_j$ for $j=\ell+1, \ldots, m$. Since the surface is rough in only one dimension, the lateral scattering is negligible and $\phi=0$. Then the scattering coefficient is:

$$\begin{aligned}\rho &= \frac{C}{4XY}\int_{-L}^{L}\int_{-X}^{X} \exp[i\,x\,u_x + i\,z(x)\,u_z]dx\,dy \\ &= \frac{(2L)C}{4XY}\left\{\int_{-X}^{-\omega_m} \exp(i\,x\,u_x)dx + \int_{-\omega_m}^{\omega_m} \exp[i\,x\,u_x + i\,z(x)\,u_z]dx \right. \\ &\left. + \int_{\omega_m}^{X} \exp(i\,x\,u_x)dx\right\} .\end{aligned} \tag{B.8}$$

Evaluation of the first and last integrals and changing of the middle one to line-segment integrals result in:

$$\rho = \frac{(2L)\,C}{2XY\,u_x}\left(\sin u_x X - \sin u_x \omega_m\right) + \frac{(2L)C}{4XY}\sum_{j=1}^{m} I_{\pm j} \tag{B.9}$$

where

$$I_{\pm j} = \int_{+j} \exp[i x u_x + i z(x) u_z] dx + \int_{-j} \exp[i x u_x + i z(x) u_z] dx \quad . \tag{B.10}$$

Now, if we substitute Equation 3.1 given on page 44 for z (x) in Equation B.10 we get:

$$I_{\pm j} = \int_{-\omega_j}^{-\omega_{j-1}} \exp[i x u_x + i (-a_j x + b_j) u_z] dx + \int_{\omega_{j-1}}^{\omega_j} \exp[i x u_x + i (a_j x + b_j) u_z] dx \quad . \tag{B.11}$$

After evaluation of the above integrals and elementary manipulations, $I_{\pm j}$ reduces to:

$$I_{\pm j} = \frac{2}{u_x^2 + a_j^2 u_z^2} (G_j + i H_j) \tag{B.12}$$

in which

$$G_j = S_j \cos d_j u_z + T_j \sin d_j u_z \tag{B.13}$$

$$H_j = T_j \cos d_j u_z - S_j \sin d_j u_z \tag{B.14}$$

$$S_j = u_x \sin u_x \omega_j - u_x \sin u_x \omega_{j-1} \cos q_j - a_j u_z \cos u_x \omega_{j-1} \sin q_j \tag{B.15}$$

$$T_j = u_x \sin u_x \omega_{j-1} \sin q_j + a_j u_z \cos u_x \omega_j - a_j u_z \cos u_x \omega_{j-1} \cos q_j \tag{B.16}$$

$$q_j = (\omega_j - \omega_{j-1}) a_j u_z \tag{B.17}$$

and

$$a_j = \frac{d_{j-1} - d_j}{\omega_j - \omega_{j-1}} \tag{B.18}$$

Substitution of Equation B.12 in Equation B.9 gives:

$$\rho = \frac{(2L)C}{2XY\ u_x} (\sin u_x X - \sin u_x \omega_m) + \frac{(2L)C}{2XY} \sum_{j=1}^{m} \frac{G_j + i\ H_j}{u_x^2 + a_j^2 u_z^2} \tag{B.19}$$

Finally, we separate the effect of the valley and ridges to arrive at:

$$\rho = \frac{(2L)\,C}{2XY\ u_x} (\sin u_x X - \sin u_x \omega_m) + \frac{(2L)\,C}{2XY} \left[\sum_{j=1}^{\ell} \frac{G_j + i\ H_j}{u_x^2 + a_j^2 u_z^2} + \sum_{j=\ell+1}^{m} \frac{G_{rj} + i H_{rj}}{u_x^2 + a_{rj}^2 u_z^2} \right] \tag{B.20}$$

where

$$G_{rj} = S_{rj} \cos h_j u_z - T_{rj} \sin h_j u_z \tag{B.21}$$

$$H_{rj} = T_{rj} \cos h_j u_z + S_{rj} \sin h_j u_z \tag{B.22}$$

$$S_{rj} = u_x \sin u_x \omega_j - u_x \sin u_x \omega_{j-1} \cos q_{rj} - a_{rj} u_z \cos u_x \omega_{j-1} \sin q_{rj} \tag{B.23}$$

$$T_{rj} = u_x \sin u_x \omega_{j-1} \sin q_{rj} + a_{rj} u_z \cos u_x \omega_j - a_{rj} u_z \cos u_x \omega_{j-1} \cos q_{rj} \tag{B.24}$$

$$q_{rj} = (\omega_j - \omega_{j-1}) a_{rj} u_z \tag{B.25}$$

$$a_{rj} = \frac{h_j - h_{j-1}}{\omega_j - \omega_{j-1}} \tag{B.26}$$

and G_j, H_j, S_j, T_j, q_j and a_j are defined in Equations B.13 to B.18.

B.2 The Sinusoidal Profile

The sinusoidal profile (c) of Figure 3.1 on page 43 described by

$$z(x) = \begin{cases} d_o \dfrac{\cos \omega_\ell - \cos x}{1 - \cos \omega_\ell} & -\pi \le x \le \pi \\ 0 & \text{elsewhere} \end{cases} \tag{B.27}$$

is used in this section to develop the scattering coefficient from Equation B.1 as follows.

$$\begin{aligned} \rho &= \frac{C}{4XY} \int_{-L}^{L} \int_{-X}^{X} \exp[i x u_x + i z(x) u_z] dx\, dy \\ &= \frac{(2L)C}{4XY} \left\{ \int_{-X}^{-\pi} \exp(i x u_x) dx + \int_{-\pi}^{\pi} \exp[i x u_x + i z(x) u_z] dx \right. \\ &\qquad \left. + \int_{\pi}^{X} \exp(i x u_x) dx \right\} . \end{aligned} \tag{B.28}$$

Evaluating the first and third integrals and substitution of z(x) in the second integral gives:

$$\rho = \frac{(2L)C}{2\,X\,Y\,u_x}\left[\sin u_x X - \sin u_x \pi\right] + \frac{(2L)C}{4\,X\,Y}\cdot$$

$$\exp\left(i u_z d_o \frac{\cos\omega_\ell}{1-\cos\omega_\ell}\right)\int_{-\pi}^{\pi}\exp\left(i u_x x - i\frac{u_z d_o}{1-\cos\omega_\ell}\cos x\right)dx \quad . \tag{B.29}$$

If we assume that $\theta_i = \theta_r$, then the above integral reduces to a Bessel function of first kind zero order. Then:

$$\rho = \frac{2L}{2Y}\left\{\left(1-\frac{\pi}{X}\right) + \frac{\pi}{X}\exp\left(i u_z d_o \frac{\cos\omega_\ell}{1-\cos\omega_\ell}\right)J_o\left(\frac{-u_z d_o}{1-\cos\omega_\ell}\right)\right\} \tag{B.30}$$

in which

$$u_z = \frac{-4\pi}{\lambda}\cos\theta_i \tag{B.32}$$

APPENDIX C

SURFACE PROFILE TRANSFORMATION

In this appendix we determine the transformation integral

$$I = \int_{\mathbf{r}} z(\mathbf{r}) \exp(-i\,\mathbf{u}\cdot\mathbf{r})\, d\mathbf{r} \tag{C.1}$$

in which $z(\mathbf{r})$ gives the height of surface roughness at $\mathbf{r}$,

$$\mathbf{u} = u_x \mathbf{a}_x + u_y \mathbf{a}_y = \frac{2\pi}{\lambda} \sin\theta_r \left(\cos\phi\, \mathbf{a}_x + \sin\phi\, \mathbf{a}_y \right) \tag{C.2}$$

and

$$\mathbf{r} = x\, \mathbf{a}_x + y\, \mathbf{a}_y \ . \tag{C.3}$$

The surface described by $z(\mathbf{r})$ has a piecewise-linear profile as shown in Figure 3.2 on page 45 with the flaw extending in the y-direction from $y = -L$ to $y = +L$.

For convenience, we temporarily assume that $h_j = -d_j$ for $j = \ell + 1, \ldots, m$. Then from Equations C.1 to C.3 we have:

$$I = \int_{\mathbf{r}} z(\mathbf{r}) \exp(-i\,\mathbf{u}\cdot\mathbf{r})\, d\mathbf{r} =$$

$$= \int_{-Y}^{Y} \int_{-X}^{X} z(\mathbf{r}) \exp[-i(x u_x + y u_y)] dx\, dy = \tag{C.4}$$

$$2\left(\frac{\sin u_y L}{u_y}\right) \int_{-\omega_m}^{\omega_m} z(x) \exp(-i\, x\, u_x) dx \ .$$

The above integral can be evaluated by summing the integrals of symetrical pairs of the profile segments. That is:

$$I = 2\left(\frac{\sin u_y L}{u_y}\right) \sum_{j=1}^{m} I_{\pm j} \tag{C.5}$$

where

$$I_{\pm j} = \int_{-\omega_j}^{-\omega_{j-1}} z(x) \exp(-i\, x\, u_x) dx + \int_{\omega_{j-1}}^{\omega_j} z(x) \exp(-i\, x\, u_x) dx \ . \tag{C.6}$$

If we replace z(x) of Equation C.6 with appropriate functions from Equation 3.1 on page 44 and use the integration formula

$$\int (a\, x + b) \exp(-i\, u_x x) dx = \frac{1}{u_x^2} [a + i\, u_x (a\, x + b)] \exp(-i\, u_x x) \tag{C.7}$$

we get:

$$I_{\pm j} = \int_{-\omega_j}^{-\omega_{j-1}} (-a_j x + b_j)\exp(-i\,x\,u_x)dx + \int_{\omega_{j-1}}^{\omega_j} (a_j x + b_j)\exp(-i\,x\,u)dx$$

$$= \frac{2}{u_x^2}\left[a_j(\cos u_x\omega_j - \cos u_x\omega_{j-1}) + u_x d_{j-1}\sin u_x\omega_{j-1} - u_x d_j \sin u_x\omega_j\right].$$

(C.8)

Substituting Equation C.8 in Equation C.5 gives:

$$I = \frac{4\sin u_y L}{u_x^2 u_y}\left[\sum_{j=1}^{m} a_j \cos u_x\omega_j - \sum_{j=1}^{m} a_j \cos u_x\omega_{j-1} + u_x \sum_{j=1}^{m}(d_{j-1}\sin u_x\omega_{j-1} - d_j \sin u_x\omega_j)\right] . \quad (C.9)$$

The last summation in Equation C.9 is equal to:

$$\sum_{j=1}^{m}(d_{j-1}\sin u_x\omega_{j-1} - d_j \sin u_x\omega_j) = d_o \sin u_x\omega_o - d_m \sin u_x\omega_m \quad (C.10)$$

but since $\omega_o = 0$ and $d_m = 0$, the summation is zero. Now we define $\omega_{-1} = \infty$ and $d_{-1} = 0$, then since d_o is finite we have:

$$\frac{d_{-1} - d_o}{\omega_o - \omega_{-1}}\cos u_x\omega_o = a_o \cos u_x\omega_o = 0 . \quad (C.11)$$

Therefore

$$\sum_{j=1}^{m} a_j \cos u_x \omega_j = \sum_{j=0}^{m} a_j \cos u_x \omega_j \quad . \tag{C.12}$$

It is desirable that the second summation in Equation C.9 contain ω_j rather than ω_{j-1}. To make this change, we add 1 to the subscripts inside the summation and substract 1 from the summation limits. The result is:

$$\sum_{j=1}^{m} a_j \cos u_x \omega_{j-1} = \sum_{j=0}^{m-1} a_{j+1} \cos u_x \omega_j \quad . \tag{C.13}$$

However, since $d_m = d_{m+1} = \omega_{m+1} = 0$, a_{m+1} is zero and

$$\sum_{j=1}^{m} a_j \cos u_x \omega_{j-1} = \sum_{j=0}^{m} a_{j+1} \cos u_x \omega_j \quad . \tag{C.14}$$

Substitution of Equations C.12 and C.14 in Equation C.9 gives:

$$\begin{aligned} I &= \frac{4 \sin u_y L}{u_x^2 u_y} \left[\sum_{j=0}^{m} a_j \cos u_x \omega_j - \sum_{j=0}^{m} a_{j+1} \cos u_x \omega_j \right] \\ &= \frac{4 \sin u_y L}{u_x^2 u_y} \sum_{j=0}^{m} (a_j - a_{j+1}) \cos u_x \omega_j \quad . \end{aligned} \tag{C.15}$$

Finally, if we substitute a_j from Equation 3.2 on page 44 and change the depth parameters d_j, $j = \ell + 1, \ldots, m$ to height parameters h_j, $j = \ell + 1, \ldots, m$, we get:

$$\int_{\mathbf{r}} z(\mathbf{r}) \exp(-i\,\mathbf{u}\cdot\mathbf{r})\,d\mathbf{r} = \left(\frac{4 \sin u_y L}{u_x^2 u_y}\right)\left[\sum_{j=0}^{\ell}\left(\frac{d_{j+1}-d_j}{\omega_{j+1}-\omega_j} - \frac{d_j - d_{j-1}}{\omega_j - \omega_{j-1}}\right)\cos u_x \omega_j \right.$$

$$\left. + \sum_{\ell+1}^{m}\left(\frac{h_j - h_{j-1}}{\omega_j - \omega_{j-1}} - \frac{h_{j+1}-h_j}{\omega_{j+1}-\omega_j}\right)\cos u_x \omega_j\right| \qquad \text{(C.16)}$$

in which $d_j = h_j = 0$ and $\omega_j = \infty$ for $j > m$ or $j < 0$.

APPENDIX D

TRUNCATED DATA STATISTICS

This appendix contains the truncated data statistics obtained by program COREG2. Tables of mean, standard deviation, lower limits, upper limits, depth correlations, and width correlations for the thirty features under study are presented.

Table D.1. Mean values of features 1-10 for truncated data.

FLAW NAME	FEATURE									
	WS	WP	RS	TE	T*P	T/P	P/T	RS5	RS16	RSR
C8	25.5	1.01	167.0	192.5	10197	3.79	0.26	45.7	2.59	17.61
C9	26.3	1.03	256.8	283.1	22016	3.56	0.28	74.0	2.65	27.86
C1	26.5	1.03	372.0	398.6	45720	3.50	0.29	169.2	2.65	63.80
B4	26.6	1.03	324.7	351.4	33441	3.68	0.27	158.8	2.63	60.32
A7	25.6	1.02	345.0	370.7	40944	3.36	0.30	133.0	2.63	50.42
C5	26.2	1.04	364.5	390.7	46255	3.27	0.31	187.0	2.66	70.37
C2	27.8	1.07	456.5	484.2	64379	3.59	0.28	213.2	2.74	77.66
C10	26.4	1.02	260.5	286.7	22358	3.66	0.27	127.7	2.59	49.23
B5	26.5	1.03	375.3	401.9	48076	3.37	0.30	217.8	2.64	82.39
C6	28.6	1.07	682.2	710.7	150488	3.39	0.30	339.8	3.04	111.76
C3	27.9	1.07	524.5	552.3	92289	3.39	0.30	228.8	2.83	80.59
4.5	28.2	1.06	675.8	704.0	145392	3.37	0.30	350.7	2.88	121.62
C7	29.3	1.08	789.4	818.7	213239	3.18	0.31	316.4	3.04	103.59
B6	28.4	1.07	625.5	653.9	146470	2.99	0.33	345.3	2.87	119.99
C4	29.9	1.08	722.6	752.5	188139	2.99	0.33	337.6	3.13	107.85

Table D.2. Mean values of features 11-20 for truncated data.

FLAW NAME	FEATURE									
	RP1	RP2	RP3	RP4	RP5	RNP1	RNP2	RNP3	RNP4	RNP5
C8	52.13	0.79	0.50	0.18	0.06	2.6	15.1	17.4	22.0	26.0
C9	77.39	20.7	0.64	0.38	0.15	2.8	10.5	16.1	18.9	22.8
C1	108.80	80.6	0.75	0.38	0.11	3.3	6.8	15.3	18.7	23.4
B4	94.03	43.6	0.58	0.31	0.09	3.8	9.7	16.6	19.8	24.3
A7	96.45	37.1	0.56	0.29	0.08	3.6	11.0	16.8	20.1	24.4
C5	102.91	48.8	0.73	0.42	0.12	4.1	9.9	15.4	18.0	23.0
C2	130.44	74.8	0.71	0.31	0.09	3.6	8.5	15.8	20.0	24.7
C10	77.13	29.3	0.54	0.27	0.08	3.6	11.1	17.0	20.5	24.6
B5	104.07	55.2	0.66	0.34	0.10	4.3	10.2	16.0	19.4	23.9
C6	210.68	32.0	0.29	0.07	0.09	4.3	14.0	21.0	24.9	24.5
C3	147.04	112.6	0.75	0.30	0.16	3.1	7.5	15.5	20.3	23.2
4.5	199.35	106.5	0.43	0.15	0.11	3.8	9.7	18.5	22.9	23.0
C7	252.00	130.9	0.16	0.13	0.07	3.2	10.3	23.4	23.0	24.9
B6	213.72	0.68	0.39	0.11	0.05	5.0	16.1	18.7	23.4	26.0
C4	249.58	0.08	0.13	0.05	0.05	4.8	27.1	23.0	26.0	26.0

Table D.3. Mean values of features 21-30 for truncated data.

FLAW NAME	FEATURE									
	RM1	RM2	RM3	RM4	RM5	RNM1	RNM2	RNM3	RNM4	RNM5
C8	0.70	0.45	0.16	0.05	0.03	14.1	16.4	21.0	24.9	27.1
C9	17.54	0.58	0.34	0.14	0.05	9.5	15.1	17.9	21.8	24.8
C1	61.95	0.67	0.35	0.10	0.04	5.8	14.3	17.7	22.4	25.3
B4	35.11	0.52	0.28	0.08	0.04	8.7	15.6	18.8	23.3	25.9
A7	25.28	0.50	0.27	0.08	0.03	10.0	15.8	19.1	23.4	26.8
C5	30.9	0.65	0.38	0.11	0.04	8.9	14.4	17.0	22.0	25.3
C2	58.73	0.62	0.28	0.08	0.05	7.5	14.8	19.0	23.7	25.0
C10	25.83	0.48	0.25	0.07	0.03	10.7	16.0	19.5	23.6	27.2
B5	32.19	0.59	0.30	0.09	0.04	9.2	15.0	18.4	22.9	26.1
C6	25.36	0.22	0.07	0.02	0.02	13.0	21.0	23.9	29.7	29.6
C3	79.03	0.63	0.26	0.14	0.06	6.5	14.8	19.4	22.2	24.6
4.5	87.22	0.37	0.14	0.06	0.03	8.7	17.8	21.9	26.1	27.8
C7	108.26	0.07	0.11	0.01	0.02	10.5	26.8	22.2	31.0	29.0
B6	0.59	0.29	0.08	0.05	0.01	15.1	19.0	23.7	25.0	31.0
C4	0.03	0.05	0.01	0.05	0.01	28.6	27.8	31.0	25.0	31.0

Table D.4. Standard deviations of features 1-10 for truncated data.

FLAW NAME	FEATURE									
	WS	WP	RS	TE	T*P	T/P	P/T	RS5	RS16	RSR
C8	0.37	0.03	11.58	11.68	1633.9	0.28	0.02	6.03	0.03	2.124
C9	0.29	0.03	12.45	12.49	2847.9	0.23	0.02	15.08	0.01	5.568
C1	0.32	0.03	26.16	26.05	7752.0	0.17	0.01	17.41	0.01	6.361
B4	0.32	0.03	9.85	9.88	2126.7	0.14	0.01	20.09	0.02	7.286
A7	0.39	0.03	35.43	35.55	9717.5	0.31	0.03	19.95	0.02	7.208
C5	0.50	0.02	13.30	13.29	4240.8	0.18	0.02	16.07	0.03	5.342
C2	0.25	0.01	22.60	22.64	6306.0	0.13	0.01	28.40	0.07	8.696
C10	0.36	0.03	12.90	12.56	2330.9	0.18	0.01	4.98	0.04	1.226
B5	0.33	0.03	13.78	13.86	5685.3	0.24	0.02	12.55	0.01	4.506
C6	0.24	0.01	40.27	40.37	17409.5	0.18	0.01	25.74	0.03	7.186
C3	0.31	0.01	21.26	21.37	12766.0	0.25	0.02	51.07	0.06	16.857
4.5	0.32	0.01	27.31	27.24	16896.6	0.25	0.02	15.74	0.05	3.628
C7	0.27	0.01	38.45	38.77	17018.1	0.18	0.02	59.85	0.07	17.729
B6	0.33	0.01	89.19	89.65	37661.7	0.17	0.02	51.10	0.05	19.972
C4	0.27	0.01	28.24	28.39	21206.5	0.11	0.01	22.00	0.03	6.045

Table D.5. Standard deviations of features 11-20 for truncated data.

FLAW NAME	FEATURE									
	RP1	RP2	RP3	RP4	RP5	RNP1	RNP2	RNP3	RNP4	RNP5
C8	5.69	0.24	0.15	0.13	0.03	0.50	1.49	1.22	2.18	2.04
C9	8.24	27.65	0.15	0.15	0.12	0.43	4.45	1.23	2.27	2.29
C1	13.87	44.29	0.19	0.11	0.02	0.74	3.70	1.45	1.82	1.09
B4	4.35	44.55	0.13	0.15	0.03	0.95	4.95	1.08	2.49	1.54
A7	11.52	50.69	0.11	0.16	0.03	0.51	4.95	1.03	2.57	1.45
C5	13.36	57.46	0.13	0.01	0.00	1.00	4.50	0.94	0.00	0.00
C2	6.09	57.91	0.25	0.16	0.04	0.74	4.27	1.93	2.88	2.97
C10	4.90	34.39	0.11	0.16	0.03	0.50	5.33	1.04	2.59	1.50
B5	7.71	65.21	0.20	0.15	0.03	1.15	4.56	1.57	2.34	1.38
C6	13.46	79.13	0.24	0.03	0.04	0.84	5.48	3.89	1.49	2.56
C3	10.29	75.12	0.24	0.19	0.15	0.27	4.11	1.95	2.79	3.14
4.5	13.43	95.88	0.22	0.12	0.00	0.77	5.22	2.71	2.43	0.00
C7	16.98	118.03	0.17	0.00	0.03	0.58	6.41	3.23	0.00	1.49
B6	31.88	0.24	0.11	0.02	0.00	0.00	1.99	1.82	1.09	0.00
C4	18.13	0.12	0.00	0.00	0.00	0.36	4.17	0.00	0.00	0.00

Table D.6. Standard deviations of features 21-30 for truncated data.

FLAW NAME	FEATURE									
	RM1	RM2	RM3	RM4	RM5	RNM1	RNM2	RNM3	RNM4	RNM5
C8	0.19	0.13	0.12	0.03	0.01	1.49	1.22	2.18	1.90	1.96
C9	23.25	0.13	0.14	0.11	0.02	4.45	1.23	2.27	2.29	1.61
C1	34.46	0.16	0.10	0.02	0.01	3.70	1.45	1.82	1.09	1.07
B4	35.76	0.11	0.13	0.03	0.01	4.95	1.08	2.50	1.54	1.54
A7	34.29	0.10	0.14	0.03	0.01	4.95	1.03	2.57	1.45	1.96
C5	36.26	0.11	0.01	0.01	0.01	4.50	0.94	0.00	0.00	1.07
C2	45.54	0.21	0.14	0.04	0.00	4.27	1.93	2.88	2.97	0.00
C10	30.29	0.10	0.14	0.03	0.01	5.33	1.04	2.59	1.51	2.01
B5	37.78	0.17	0.13	0.03	0.02	4.56	1.57	2.34	1.38	2.03
C6	62.65	0.21	0.03	0.00	0.00	5.48	4.13	1.49	1.54	0.94
C3	51.89	0.21	0.17	0.14	0.04	4.11	2.01	2.79	3.14	2.44
4.5	78.07	0.21	0.11	0.05	0.01	5.22	2.96	2.43	4.50	1.87
C7	97.05	0.10	0.02	0.00	0.00	8.53	4.96	0.80	0.00	0.00
B6	0.21	0.15	0.04	0.00	0.00	1.99	2.88	2.55	0.00	0.00
C4	0.02	0.05	0.00	0.00	0.00	1.98	4.47	0.00	0.00	0.00

Table D.7. Lower limits of features 1-10 for truncated data.

FLAW NAME	FEATURE									
	WS	WP	RS	TE	T*P	T/P	P/T	RS5	RS16	RSR
C8	24.86	0.99	148.1	173.4	7057	3.41	0.23	38.08	2.55	14.93
C9	25.83	1.00	235.4	261.6	18522	3.24	0.25	52.87	2.62	20.18
C1	26.18	1.00	317.3	343.9	32591	3.24	0.27	148.67	2.64	56.31
B4	26.23	1.00	307.6	334.4	29678	3.51	0.25	131.41	2.60	50.54
A7	25.02	0.99	301.2	326.6	31734	2.77	0.26	103.49	2.58	40.11
C5	25.39	1.00	346.0	372.1	40963	3.04	0.27	164.00	2.62	62.59
C2	27.34	1.06	401.9	429.6	53056	3.40	0.26	167.40	2.67	62.70
C10	25.64	0.99	241.0	267.7	18806	3.27	0.25	117.72	2.53	46.53
B5	26.04	1.00	360.3	385.7	41236	2.97	0.27	193.99	2.63	73.76
C6	27.99	1.06	632.8	661.3	126882	3.12	0.27	302.95	2.99	101.32
C3	27.44	1.06	490.1	517.5	73978	2.94	0.27	118.59	2.67	44.41
4.5	27.74	1.06	642.7	670.8	126377	2.98	0.27	325.44	2.83	115.0
C7	28.75	1.06	732.8	761.5	184005	2.78	0.29	186.98	2.92	64.03
B6	27.87	1.06	477.9	505.1	87080	2.71	0.30	262.95	2.81	93.55
C4	29.40	1.07	673.9	703.9	160105	2.82	0.31	302.49	3.08	98.21

Table D.8. Lower limits of features 11-20 for truncated data.

FLAW NAME	FEATURE									
	RP1	RP2	RP3	RP4	RP5	RNP1	RNP2	RNP3	RNP4	RNP5
C8	40.69	0.64	0.42	0.09	0.02	2.0	11.0	14.0	18.0	23.0
C9	67.98	0.65	0.43	0.12	0.05	2.0	5.0	14.0	16.0	18.0
C1	83.78	0.93	0.42	0.12	0.05	3.0	5.0	14.0	18.0	23.0
B4	86.66	0.65	0.42	0.11	0.05	3.0	5.0	15.0	18.0	23.0
A7	83.30	0.65	0.42	0.11	0.05	3.0	5.0	16.0	18.0	23.0
C5	83.78	0.93	0.64	0.42	0.11	3.0	5.0	14.0	18.0	23.0
C2	119.69	0.93	0.43	0.05	0.02	3.0	5.0	13.0	18.0	23.0
C10	69.28	0.64	0.42	0.11	0.05	3.0	5.0	16.0	18.0	23.0
B5	90.96	0.80	0.42	0.11	0.05	3.0	5.0	14.0	18.0	23.0
C6	191.86	0.05	0.05	0.05	0.02	3.0	5.0	16.0	23.0	23.0
C3	135.96	0.93	0.43	0.11	0.05	3.0	5.0	14.0	16.0	18.0
4.5	181.92	0.46	0.12	0.05	0.12	3.0	5.0	14.0	18.0	23.0
C7	225.01	0.46	0.05	0.13	0.05	3.0	5.0	18.0	23.0	23.0
B6	158.50	0.43	0.12	0.05	0.05	5.0	14.0	18.0	23.0	26.0
C4	225.01	0.02	0.13	0.05	0.05	4.0	18.0	23.0	26.0	26.0

Table D.9. Lower limits of features 21-30 for truncated data.

FLAW NAME	FEATURE									
	RM1	RM2	RM3	RM4	RM5	RNM1	RNM2	RNM3	RNM4	RNM5
C8	0.59	0.39	0.08	0.02	0.02	10.0	13.0	17.0	22.0	25.0
C9	0.59	0.39	0.11	0.05	0.02	4.0	13.0	15.0	17.0	22.0
C1	0.82	0.39	0.11	0.05	0.02	4.0	13.0	17.0	22.0	25.0
B4	0.59	0.38	0.11	0.05	0.02	4.0	14.0	17.0	22.0	25.0
A7	0.59	0.39	0.11	0.04	0.02	4.0	15.0	17.0	22.0	25.0
C5	0.79	0.57	0.38	0.10	0.02	4.0	13.0	17.0	22.0	25.0
C2	0.82	0.38	0.05	0.02	0.05	4.0	12.0	17.0	22.0	25.0
C10	0.57	0.38	0.11	0.04	0.02	4.0	15.0	17.0	22.0	25.0
B5	0.68	0.38	0.11	0.05	0.02	4.0	13.0	17.0	22.0	22.0
C6	0.05	0.03	0.05	0.02	0.02	4.0	15.0	22.0	28.0	29.0
C3	0.82	0.39	0.11	0.05	0.02	4.0	13.0	15.0	17.0	22.0
4.5	0.39	0.11	0.05	0.01	0.02	4.0	13.0	17.0	22.0	25.0
C7	0.02	0.02	0.05	0.01	0.02	4.0	17.0	22.0	31.0	29.0
B6	0.39	0.05	0.01	0.05	0.01	13.0	17.0	22.0	25.0	31.0
C4	0.01	0.01	0.01	0.05	0.02	22.0	22.0	31.0	25.0	31.0

Table D.10. Upper limits of features 1-10 for truncated data.

FLAW NAME	FEATURE									
	WS	WP	RS	TE	T*P	T/P	P/T	RS5	RS16	RSR
C8	25.99	1.06	182.6	208.4	11780	4.26	0.29	56.12	2.64	21.28
C9	26.88	1.06	276.4	303.1	27133	3.96	0.31	100.20	2.67	37.53
C1	27.21	1.06	401.6	427.8	57994	3.75	0.31	197.70	2.68	73.78
B4	27.46	1.08	339.2	365.6	37774	4.02	0.28	190.96	2.65	72.06
A7	26.28	1.06	416.3	442.2	58301	3.80	0.36	165.89	2.66	62.36
C5	27.02	1.06	379.3	406.3	53384	3.67	0.33	212.90	2.76	77.61
C2	28.14	1.08	477.7	505.2	72425	3.82	0.29	249.41	2.83	88.56
C10	26.76	1.06	279.8	305.0	27427	3.93	0.31	137.26	2.65	51.80
B5	27.07	1.08	398.97	425.6	57183	3.68	0.34	235.05	2.66	88.49
C6	28.94	1.08	750.99	779.6	178733	3.76	0.32	394.63	3.12	126.48
C3	28.31	1.08	563.5	591.4	112132	3.75	0.34	284.21	2.98	96.54
4.5	28.74	1.08	735.8	764.2	176485	3.68	0.33	377.10	2.99	126.18
C7	29.66	1.09	845.7	875.3	238689	3.40	0.36	386.22	3.13	123.39
B6	29.05	1.08	742.2	770.7	190524	3.32	0.37	415.38	2.97	139.86
C4	30.18	1.09	775.3	805.7	225597	3.19	0.35	381.42	3.16	120.70

Table D.11. Upper limits of features 11-20 for truncated data.

FLAW NAME	FEATURE									
	RP1	RP2	RP3	RP4	RP5	RNP1	RNP2	RNP3	RNP4	RNP5
C8	57.57	1.48	0.93	0.43	0.11	3.0	16.0	18.0	24.0	30.0
C9	89.53	64.42	0.93	0.64	0.43	3.0	16.0	18.0	23.0	26.0
C1	133.09	118.18	0.95	0.43	0.12	5.0	14.0	18.0	23.0	26.0
B4	101.49	94.08	0.80	0.43	0.12	5.0	16.0	18.0	23.0	26.0
A7	125.51	117.72	0.65	0.43	0.12	4.0	16.0	18.0	23.0	26.0
C5	127.91	117.71	0.93	0.43	0.12	5.0	14.0	16.0	18.0	23.0
C2	142.74	131.62	1.11	0.43	0.12	5.0	14.0	18.0	26.0	30.0
C10	83.3	73.69	0.65	0.43	0.12	4.0	16.0	18.0	23.0	26.0
B5	113.74	132.54	0.93	0.46	0.12	6.0	15.0	18.0	23.0	26.0
C6	228.84	220.60	0.64	0.12	0.11	5.0	26.0	26.0	26.0	29.0
C3	166.60	187.23	0.95	0.64	0.43	4.0	14.0	18.0	23.0	26.0
4.5	224.80	216.89	0.93	0.43	0.12	5.0	18.0	23.0	26.0	23.0
C7	273.85	255.82	0.46	0.13	0.11	5.0	18.0	26.0	23.0	26.0
B6	257.7	0.95	0.46	0.12	0.05	5.0	18.0	23.0	26.0	26.0
C4	285.48	0.46	0.13	0.05	0.05	5.0	30.0	23.0	26.0	26.0

Table D.12. Upper limits of features 21-30 for truncated data.

FLAW NAME	FEATURE									
	RM1	RM2	RM3	RM4	RM5	RNM1	RNM2	RNM3	RNM4	RNM5
C8	1.24	0.82	0.38	0.11	0.05	15.0	17.0	23.0	29.0	29.0
C9	51.75	0.82	0.59	0.38	0.11	15.0	17.0	22.0	25.0	29.0
C1	90.87	0.82	0.39	0.11	0.05	13.0	17.0	22.0	25.0	29.0
B4	75.80	0.68	0.38	0.11	0.05	15.0	17.0	22.0	25.0	29.0
A7	76.20	0.59	0.39	0.11	0.05	15.0	17.0	22.0	25.0	29.0
C5	82.31	0.82	0.39	0.11	0.05	13.0	15.0	17.0	22.0	29.0
C2	102.88	0.92	0.39	0.11	0.05	13.0	17.0	25.0	29.0	25.0
C10	64.39	0.59	0.39	0.11	0.05	15.0	17.0	22.0	25.0	29.0
B5	81.10	0.82	0.39	0.11	0.11	14.0	17.0	22.0	25.0	29.0
C6	177.67	0.59	0.11	0.02	0.02	25.0	28.0	25.0	31.0	31.0
C3	126.33	0.82	0.59	0.39	0.11	13.0	17.0	22.0	25.0	29.0
4.5	167.89	0.82	0.39	0.11	0.05	17.0	22.0	25.0	31.0	29.0
C7	194.79	0.39	0.11	0.01	0.02	29.0	31.0	25.0	31.0	29.0
B6	0.82	0.39	0.11	0.05	0.01	17.0	25.0	31.0	25.0	31.0
C4	0.11	0.11	0.01	0.05	0.01	31.0	31.0	31.0	25.0	31.0

Table D.13. Correlation between truncated data features and flaw depth or width.

FEATURE	DEPTH CORRELATION	WIDTH CORRELATION	FEATURE	DEPTH CORRELATION	WIDTH CORRELATION
WS	0.889	0.540	RNP1	0.621	0.570
WP	0.832	0.417	RNP2	0.455	0.302
RS	0.885	0.603	RNP3	0.637	0.612
TE	0.885	0.603	RNP4	0.701	0.573
T*P	0.869	0.630	RNP5	0.270	0.340
T/P	-0.786	-0.561	RM1	0.229	0.059
P/T	0.783	0.563	RM2	-0.654	-0.655
RS5	0.903	0.655	RM3	-0.692	-0.612
RS16	0.839	0.534	RM4	-0.400	-0.594
RSR	0.886	0.651	RM5	-0.436	-0.631
RP1	0.886	0.617	RNM1	0.483	0.306
RP2	0.225	0.039	RNM2	0.674	0.562
RP3	-0.597	-0.639	RNM3	0.720	0.471
RP4	-0.672	-0.613	RNM4	0.458	0.591
RP5	-0.226	-0.391	RNM5	0.659	0.700

VITA

Reza Safabakhsh was born in Isfahan, Iran, on May 24, 1953. He attended elementary schools in that city and graduated from Hakim Sanaee High School in June 1971. The following September he entered Sharif University of Technology (previously Aryamehr University of Technology), Tehran, Iran, where he received a Bachelor of Science Degree in Electrical Engineering in July 1976.

After attending an intensive English course at Simin English Institute in Tehran, Mr. Safabakhsh enrolled in the graduate program in Electrical Engineering at the University of Detroit. In September 1977, he transferred to the University of Tennessee, Knoxville, where he pursued his studies and received a Master of Science Degree in Electrical Engineering in December 1979. He then continued his graduate studies in Electrical Engineering at the University of Tennessee, Knoxville, and received a Doctor of Philosophy Degree in Electrical Engineering in March 1986.

Mr. Safabakhsh held a teaching assistantship in the Electrical Engineering Department from 1978 through 1982. In January 1983, he accepted a full-time job with Walters State Community College, Morristown, Tennessee, where he served as assistant professor of Electromechanical and Robotics Technology and Computer Science Technology. During the two years of his stay at Walters State, Mr. Safabakhsh proposed and partially implemented a program for robotics education called Electromechanical and Robotics Technology. From 1983

to 1986, he also held a graduate research assistantship in the Electrical Engineering Department of the University of Tennessee, Knoxville.

Mr. Safabakhsh is a member of several honor societies including Phi Kappa Phi and Eta Kappa Nu.